POLITECNICO DI TORINO

Master's Degree in Aerospace Engineering

Master's Degree Thesis

DIRECT NUMERICAL SIMULATION OF FLEXIBLE PATCHES

Supervisors

Prof. Francesco AVALLONE

Prof. Marco Edoardo ROSTI

Prof. Costantino MANES

Candidate

Elisa TRESSOLDI

A.Y. 2023/2024

Abstract

Canopy flows are of significant interest across various natural and industrial applications, since several elongated slender objects clamped on a wall or a surface can be addressed to as canopies. Modern word issues, such as river pollution mitigation and urban heat cooling, can benefit from a deeper understanding of the flow behavior around such structures. Although extensive research has already been conducted on rigid canopies through experimental and numerical studies, flexible canopies are more commonly encountered in many fields, highlighting the need to investigate not only the fluid behavior around flexible structures, but also the dynamics of these flexible elements and their interactions with the surrounding flow. In their recent study of Direct Numerical Simulation (DNS) of flexible canopies, Foggi Rota et al. 2024 focused on the fluid-structure interactions within and above a distribution of filaments covering the whole wall, paving the way for studies on more complex configurations. In this thesis, we expand on these findings by examining the fluid and filament dynamics in a canopy where flexible filaments cover only one half of the wall-surface, thus creating an edge aligned with the flow direction. This scenario reminds of roads cutting through forests or rivers where submerged seagrass grows along the banks. We take into account two limit flexibilities, one with almost-rigid filaments, and another where the filaments deflect significantly when hit by the flow.

The mean flow characteristics in the patch case fall well in between those of the two limit scenarios - the open channel and the full canopy. Moreover, the mean flow shows the appearance of mean vortex structures, that brings high energy flow into the canopy through the lateral edge of the patch, and that creates an updraft of the flow, transporting low-energy flow outside of the canopy through the canopy top. The analysis of the shear balance equation indicates that, unlike in full canopies and open channels, the mean flow plays a key role in balancing the forcing pressure gradient over time in canopy patches, although the turbulent shear still represents the major contributor for all the three scenarios investigated. Velocity fluctuation reveals that ejections dominate over sweeps on horizontal planes above vegetated regions, regardless of the vegetation distribution, while sweeps are predominant along the vertical planes separating vegetated and non-vegetated regions. Finally, the filament dynamics show that the average tip positions are compliant with the mean vortex structures in the domain. Overall, although the dynamics of the filaments in the patch scenario are similar to those in the full canopy, their swinging behavior varies with the spanwise position: indeed, filaments closer to the non-vegetated regions exhibit greater deflection and tend to oscillate in a wider range of frequencies if compared to those deeper within the canopy.

Table of Contents

List of Figures

Chapter 1

Introduction

When talking about canopies, we refer to filaments, fibers or, more in general, elongated elements which are clamped on a wall. Understanding how fluid flows through and around these structures has gained increasing importance due to their relevance in both natural and industrial contexts, with examples of canopy

(a) Marine Ecosystem **(b)** Crop Field

(c) Forests **(d)** Urban buildings

Figure 1.1: Examples of canopy systems.

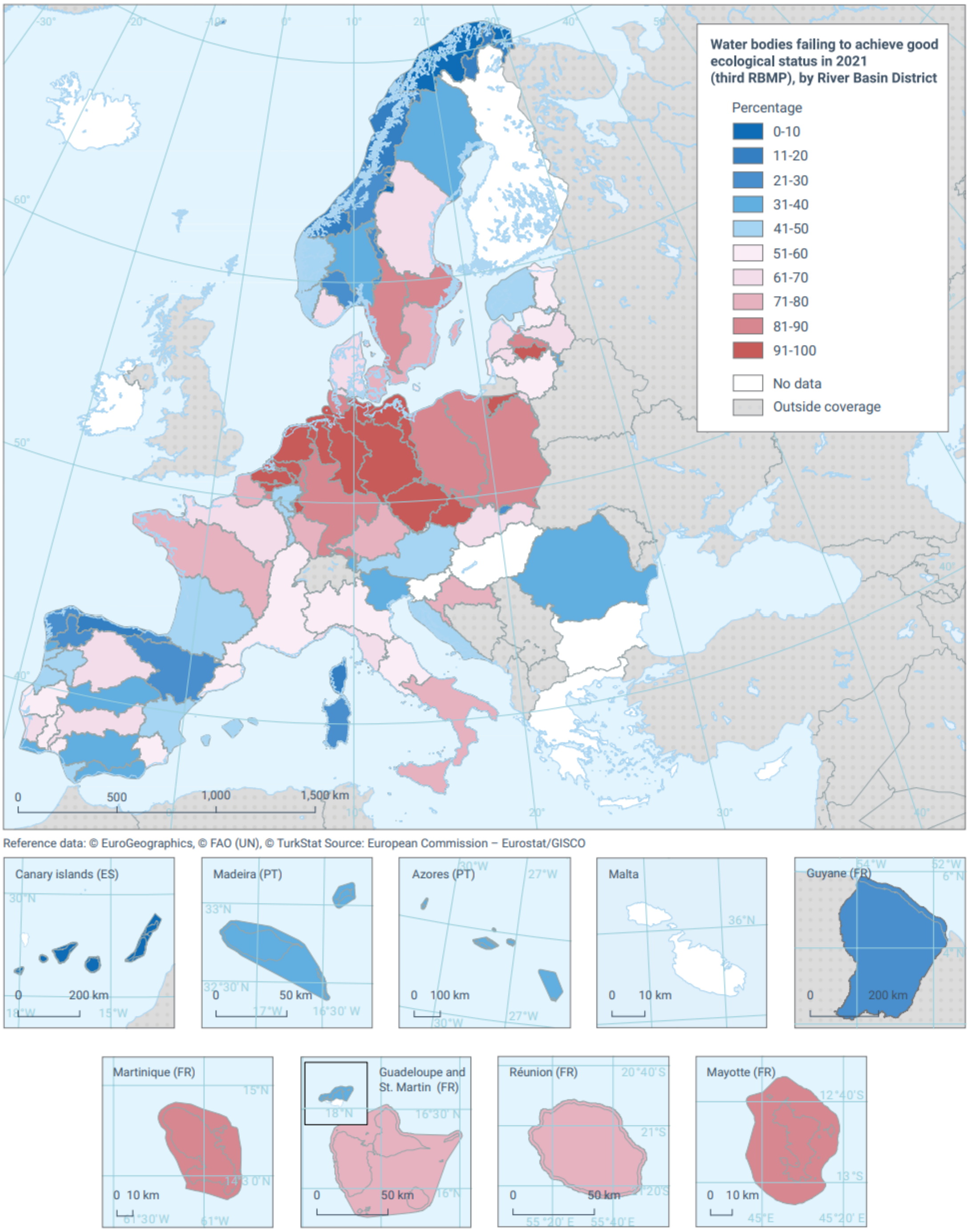

Reference data: © EuroGeographics, © FAO (UN), © TurkStat Source: European Commission – Eurostat/GISCO

Figure 1.2: Percentage of surface water bodies not meeting good ecological status across European countries and Norway (European Commission 2024).

structures including forests, crop fields, urban buildings or artificial installations. The study of natural canopies provide insights crucial for addressing hydrological and ecological challenges, while research on industrial canopies contributes to an efficient planning of urban areas and infrastructures.

In natural systems such as submerged plants or forests, canopies alter flow patterns, for example, capturing sediments and shaping bed morphology, influencing the exchange of species and microclimates. Based on the latest report by the European Environment Agency presenting the state of Europe's water (European Commission 2024), the majority of surface waters across European countries do not achieve good ecological status, as shown in figure 1.2. With reference to the Environmental Quality Standards (EQS, European Commission 2008), the four pollutant substances discharged into river basins most reported as failing EQSs across Member States were zinc, copper, arsenic and ammonium. This has significant consequences not only on human's health, but also on the preservation of ecosystems. This is the reason why the European Commission, through the EU Action Plan *Towards a Zero Pollution for Air, Water and Soil* (European Commission 2021), aims to reduce air, soil, and water pollution to levels considered safe for human health and ecosystem preservation by 2050.

A deep understanding of canopy flows is essential for addressing pollution issues, including how pollutants diffuse and accumulate in the atmosphere and in water bodies. Several studies focused on understanding the effect of plants growing in river corridors in modifying water flow, sediment and particle deposition and bed erosion (Wu et al. 2005, Gurnell 2014, C. Liu, Hu, et al. 2018). Techniques already exist to forecast sediment dynamics and trajectories, such as Sediment Trend Analysis (STA), which enables the identification of sediment patterns, accretion, and movement (McLaren et al. 2007). Therefore, advancing our understanding of flow behavior can contribute significantly to the implementation and enhancement of these forecasting techniques.

Urban and industrial applications are essential in modern city planning. According to the European Commission *Urban heat islands and heat mortality* 2024, nearly three-quarters of Europe's population resides in urban areas. In 2024, the Copernicus Climate Change Service (C3S) reported that the average surface air temperature over European land during the summer months (June–August) reached a record high, measuring 1.54°C above the 1991–2020 seasonal average (*C3S seasonal lookback: summer 2024 | Copernicus* 2024), as shown in figures 1.3 and 1.4. Such anomalies in European air temperature have become increasingly common in recent years compared to the past. People living in cities are more affected by intense heat waves: temperatures increase as paved surfaces absorb heat, buildings and

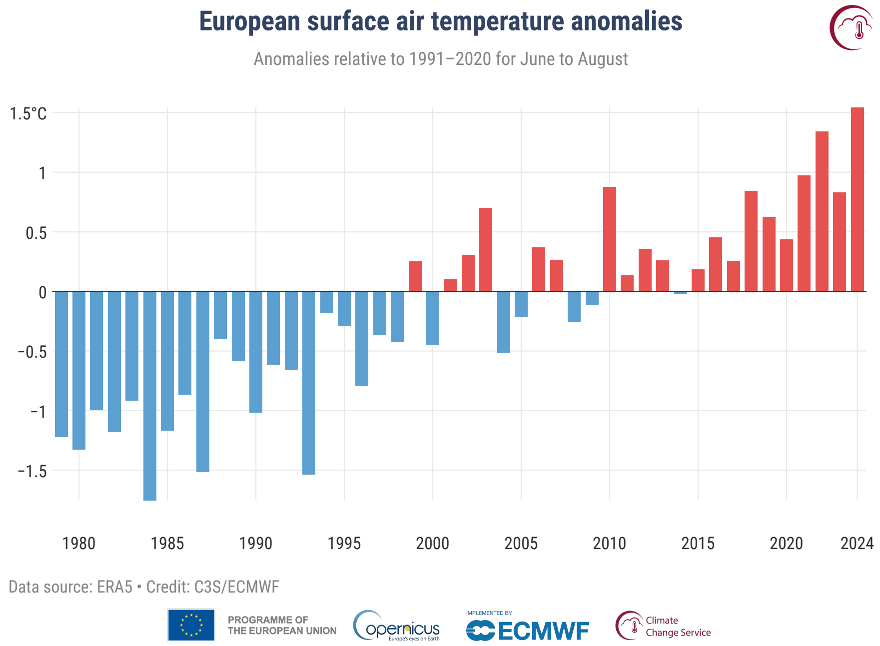

Figure 1.3: European mean surface air temperature anomalies for each boreal summer (June to August) from 1979 to 2024, relative to the 1991–2020 average. Data source: ERA5. Credit: Copernicus Climate Change Service/ECMWF

narrow streets retain it, and human activities contribute additional warmth to the environment. Gillerot et al. 2024 demonstrated the importance of urban tree canopies in local heat reduction, thus giving further evidence of the importance of understanding these kind of structures.

Not only natural structures can be modeled as canopies. Basing on the definition of canopies, every elongated element clamped on a surface can be considered as such. Thus, also urban buildings and skyscrapers can be modeled as canopies, representing the limiting scenario in which the flexibility of the slender objects tends to zero. Ashie et al. 1999, through a building canopy model coupled with CFD, studied radiant heat exchange between urban buildings as an attempt to model a more efficient air conditioning system which took into account both the indoor and outdoor heat sources. Coceal and Belcher 2004 developed an urban canopy model to study winds within and above urban areas, in an attempt to forecast air quality in cities.

Through the examples previously introduced, it becomes clear that canopies can exhibit a wide range of geometries and properties depending on the application.

Canopies may consist of rigid or flexible filaments, with uniform or varying heights, and can either cover the entire surface on which they are clamped or be arranged in patches. In this work, we refer to a *full canopy* when these structures cover the entire bottom wall of the domain, and a *canopy patch* when they are arranged in localized patches within the domain.

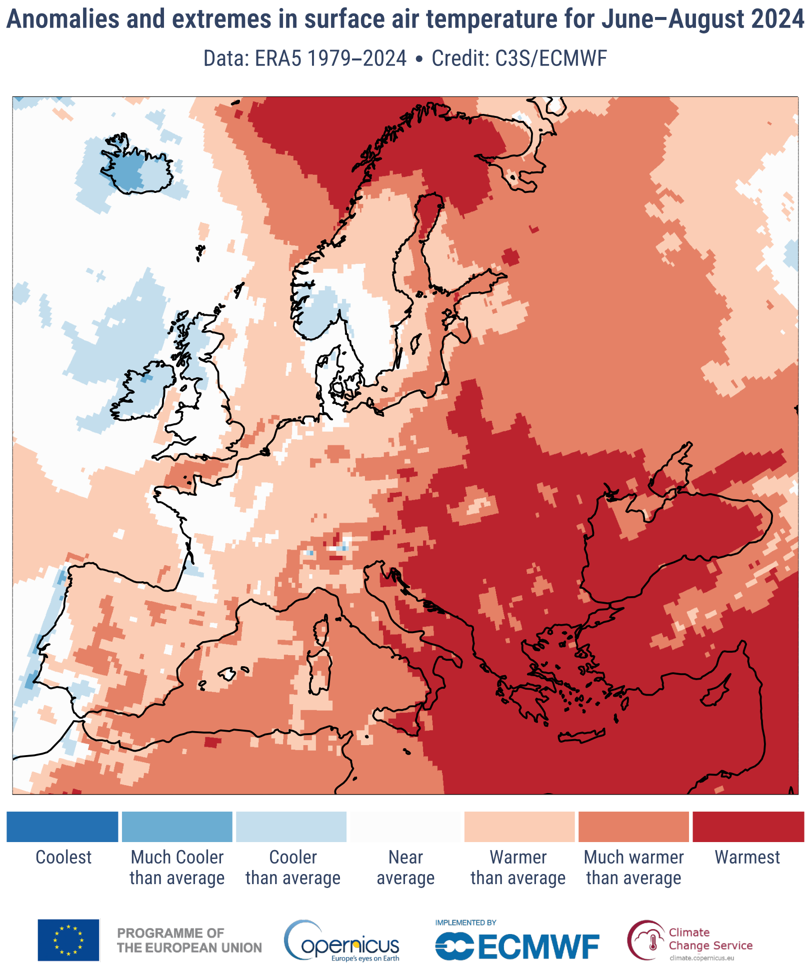

Figure 1.4: Surface air temperature anomalies and extremes for June–August 2024 are represented using color categories corresponding to percentiles of the temperature distributions for the 1991–2020 reference period. The "coolest" and "warmest" extremes are determined based on rankings spanning the period 1979–2024. Data obtained from ERA5. Source: Copernicus Climate Change Service/ECMWF

Rigid canopies have been extensively studied, with a rich body of literature addressing various aspects of their behavior. Rota et al. 2024 took this research further by introducing flexible filaments and examining both fluid and filament dynamics in a full canopy scenario across different levels of filament flexibility. But what happens in a system where the canopy has finite dimensions, creating a distinct edge? This thesis aims to investigate the behavior of both the fluid and filaments in such a scenario.

For simplicity, we focus on a natural canopy, referring to the elongated elements as filaments. Three distinct scenarios are considered:

1. Open Channel, where no filaments are present;
2. Full Canopy, where filaments cover the entire bottom wall of the domain;
3. Canopy patch, where filaments only partially cover the bottom wall of the domain.

In this way, we will refer to the filament-covered area of the domain as *vegetated region* and the not covered area as *non-vegetated*.

In the canopy patch scenario, we can imagine starting from a full canopy and removing a certain number of filaments, creating two regions, one vegetated and one non-vegetated, with a distinct edge aligned in the streamwise direction. For a visual understanding of this scenario, we can think about a straight road or highway cutting through a forest, as in figure 1.5.

Figure 1.5: Canopy patch

For scenarios involving vegetation, we consider two different levels of filament flexibility. Flexibility is characterized by the Cauchy number, a dimensionless parameter representing the ratio of the fluid's force on the filaments to the restoring force of the filaments and defined as:

$$Ca = \frac{\rho_f d h^3 U_b^2}{2\gamma}, \tag{1.1}$$

where ρ_f is the density of the fluid, h is the height of the filaments, U_b is the bulk velocity and γ is the bending rigidity of the filaments. The higher the Cauchy number, the more flexible the filaments. Thus, we consider two Cauchy numbers that describe two limit conditions, one with almost-rigid filaments and and another in which the filaments deflect significantly when hit by the flow. Therefore, unlike a scenario with entirely rigid filaments, it is crucial to focus on the fluid dynamics when interacting with flexible structures. When hit by the incoming flow, the filaments deflect, and this deflection, in turn, influences the flow dynamics. Consequently, the system forms a fluid-structure interaction problem.

Chapter 2

Literature Review

The study of canopy flows has always been of primary interest. Early investigations focused on rigid structures occupying the entire bottom wall of the domain, to later expand to more complex configurations, including modeling the slender elements as flexible filaments, to finally consider finite patches of vegetation to account for different natural scenarios and help river and water management. As an example, J. Li et al. 2022 offered interesting insights into the significance of considering different spatial layouts of vegetation distribution, emphasizing the role of the frontal projected area of vegetation patches in shaping the morphological evolution of fluvial systems. They concluded that a reduction in the frontal projected area of the vegetation patch could be an efficient solution to restore vegetation. On the other hand, other studies focused on the effect of finite length patches on the flow behind them (Folkard 2011, C. Liu, Hu, et al. 2018, Anjum and Tanaka 2020). In particular, C. Liu, Hu, et al. 2018 focused on the vortex structures forming in the wake of the patches both in the horizontal and in the vertical planes, which increment the sediment deposition and, thus, play a beneficial role in the persistence and growth of vegetation. Anjum and Tanaka 2020 highlighted how in the spaces between vegetation patches, there is a marked reduction in flow velocity, turbulent kinetic energy, and turbulence intensity attributed to the obstruction and protection offered by the patches, suggesting conditions that are beneficial for both aquatic habitats and sediment deposition.

As highlighted by Unigarro Villota et al. 2023, flows within a partially obstructed channel containing a submerged canopy can be simplified into two two-dimensional problems. Indeed, depending on the water depth and on the canopy height, aquatic vegetation can be either emergent, when the canopy height is greater than the water depth, or submerged, when the canopy is shorter than the water depth (W.-X. Huai et al. 2019). The flow above the canopy top can be studied by considering a vegetation distribution such that the vertical flow motions predominate over horizontal flow motions, thus considering submerged filaments that fully cover the bottom wall of the domain. On the other hand, the lateral edge can be modeled using patches of emergent vegetation, such that vertical motions are stronger compared to horizontal motions. However, these two scenarios do not account for the simultaneous presence of both the top edge and the lateral edge of the canopy, as each considers only one edge in isolation and simplifications on the setup can bias the outcome of the study, by either hiding or amplifying some of the relevant physical processes found in natural conditions (Tinoco et al. 2020). Consequently, recent studies have shifted their focus toward submerged canopy patches, initially representing the slender elements as rigid cylinders (Devi and Kumar 2016a, Yan, W.-H. O. Wai, et al. 2016, J. Zhang et al. 2020, D. Li et al. 2022, Yan, Duan, W.-H. Wai, et al. 2022, Yan, Jia, et al. 2023, Yan, Duan, Y.-H. Zhang, et al. 2023, Unigarro Villota et al. 2023), then focusing on more complex flexible geometries resembling more natural conditions (Pang et al. 2014, Devi and Kumar 2016b, Caroppi et al. 2021).

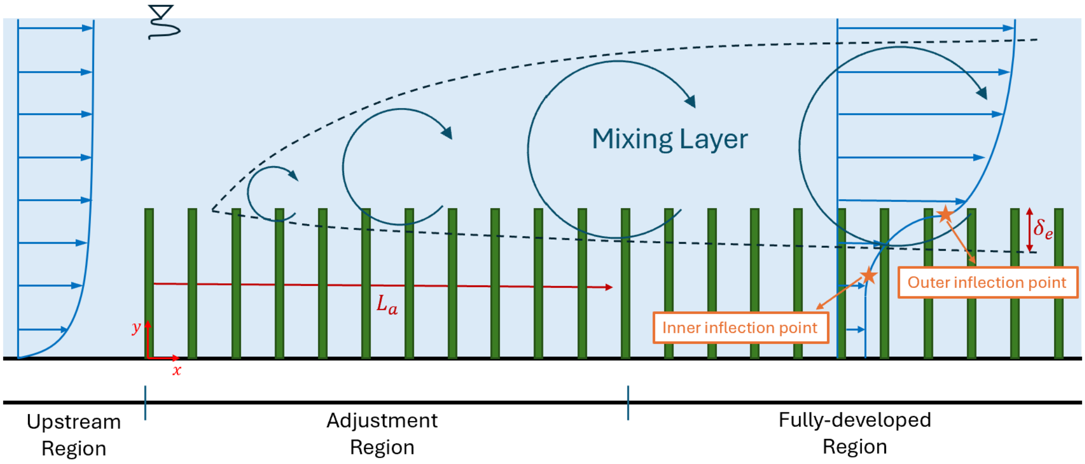

Figure 2.1: Mixing layer development above a fully distributed submerged canopy. After an adjustment length L_a over a sufficiently long canopy, the mixing layer reaches a constant thickness and ceases to grow, displaying fully developed velocity profiles. Vertical coherent vortexes grow in size coherently with the growth of the mixing layer, reaching a fixed size in the fully-developed region and penetrating in the canopy region of a vertical depth δ_e inversely proportional to the canopy drag and canopy frontal area (Figure adapted from Yan, Jia, et al. 2023.)

2.1 Fully-distributed Submerged Canopies

It is well known that any obstruction or alteration of a flow natural path can significantly change its characteristics. For instance, when a surface is entirely covered by flexible filaments or rigid cylinders, the resulting flow often exhibits modified velocity profiles, which can lead to the development of vortex structures within the flow, further influencing its behavior and interactions with the surface. This is due to the resistance opposed by the structures in the domain: the drag discontinuity at the canopy top creates a shear region similar to a free shear layer, with the flow in the canopy layer decelerating and in the upper open layer accelerating. This abrupt change in drag at the canopy top creates significant velocity shear and amplifies turbulence intensity in this area compared to unobstructed flows. Thus, flow structure within and just above an unconfined canopy more strongly resembles a mixing layer than a boundary layer (Raupach et al. 1996, Ghisalberti and H. M. Nepf 2002).

Monti, Omidyeganeh, et al. 2019, modeling the canopy as fully submerged rigid cylinders arranged on a wall, through Large Eddy Simulation of the turbulent channel, showed that flow behavior can be divided into two distinct spatial regions based on velocity distribution: the canopy layer and the outer region above it. In the outer region the velocity profile follows the logarithmic law

$$\langle u \rangle = \frac{u_\tau}{\kappa} \log \left[\frac{(y - y_{vo}) u_\tau}{\nu} \right] + B,$$

where $\kappa = 0.41$, $B = 5.2$ and y_{vo} is the so called *virtual origin*, i.e. the point from which the log-law applies. u_τ is the friction velocity at the virtual origin, thus $u_\tau = u_\tau(y_{vo})$.
Mean streamwise velocity profiles show two inflection points, one within the canopy and the other one near the canopy tip (Ikeda and Kanazawa 1996, H. M. Nepf 2012, Rota et al. 2024). As for Rayleigh's theorem (Rayleigh 1879), an inflection point in the velocity profile is a necessary condition for flow instability, thus making the flow prone to the Kelvin–Helmholtz instability. This instability produces large, coherent vortexes within the mixing layer, which play a dominant role in the vertical transport of momentum above the canopy (Raupach et al. 1996, Finnigan 2000, Ghisalberti and H. M. Nepf 2002, Ghisalberti and H. Nepf 2006, Diwan 2015). The downstream advection of the vortexes leads the flexible submerged aquatic vegetation to a gradual, synchronized, large-amplitude waving motion, a phenomenon first described by Ackerman and Okubo 1993 as *monami*, which will be further described in section 2.4. Since coherent vortexes also appear in rigid canopies, it was concluded that vegetation flexibility is not the cause of vortex formation. Instead, the Kelvin-Helmholtz instability, arising from the presence

of an upper inflection point in the velocity profiles, generates these vortexes. Consequently, the *monami* motion is a response of flexible filaments, which move in an organized, resonant pattern with the coherent eddies (Nezu and Sanjou 2008).

When encountering a sufficiently long canopy, the flow hitting a submerged fully-distributed canopy needs a certain distance to adjust and reach a fully-developed state. The flow adjustment length, is defined as the distance from the leading edge of the canopy to the position where the velocity decreases to a constant value, representing that the flow is fully developed (F. Li et al. 2024). Belcher et al. 2003, by balancing the non-linear drag exerted by the canopy with the non-linear streamwise advection, estimated the streamwise extension of the adjustment region as:

$$L_a = L_c \ln\left(\frac{U_h}{u_*}\frac{h}{L_c}\right),$$

with $L_c = 2/(C_D N b_v)$, C_D the canopy drag, N the canopy density, b_v the width of each vegetation element, U_h the velocity at the canopy tips, h the height of the vegetation elements and u_* the shear velocity at the canopy tips, defined as the square root of the peak Reynolds stress per unit mass at the canopy top in the fully developed flow region:

$$u_* = \sqrt{(-u'v')_{max}}.$$

However, Zeng and C.-W. Li 2014 noted that the above equation has not a general validity, as it could get negative values in case the canopy density is not sufficiently high. Thus, an empirical equation was suggested:

$$L_a \propto 1.5\frac{U_{av}}{u_*}D,$$

where U_{av} is the cross-sectional mean velocity.
The flow adjustment length can be calculated for submerged fully-distributed canopies as their shear layer grows only to a finite thickness, unlike free shear layers which grow continuously downstream. In fact, once the the production of shear-layer-scale turbulent kinetic energy is balanced by drag dissipation, the growth of the shear layers ceases and the fully developed state for the flow is reached. Thus, to describe the thickness of the mixing layer, the momentum thickness θ is used. It is defined as

$$\theta = \int_{-\infty}^{+\infty}\left[\frac{1}{4} - \left(\frac{U-\bar{U}}{\Delta U}\right)^2\right]dz,$$

where $\Delta U = U_2 - U_1$ is the velocity difference of the mixing layer and $\bar{U} = (U_1 + U_2)/2$ is the mean velocity, with U_1 and U_2 are the lower and upper margin velocities respectively.

The constant thickness of the shear layer controls the vertical mixing and exchange between the vegetated region and the flow above it, as Kelvin-Helmholtz vortex growth stops when the shear layer reaches a constant thickness (Ghisalberti and H. M. Nepf 2002, Ghisalberti and H. M. Nepf 2004, Nezu and Sanjou 2008). As the flow reaches an equilibrium state, turbulence intensities are increased near the top of the canopy for submerged vegetation, and the peak in the Reynolds shear stresses lays near the tips of the canopy. In particular, for rigid canopies it always coincides, within measurements and numerical errors, with the inflection point in the velocity profile (Bennett et al. 2002, White and H. M. Nepf 2008), while for flexible canopies it lays below the vegetation top due to the oscillatory motion of the flexible filaments and their greater deflection, which shifts the shear layer towards the channel bed (Okamoto and Nezu 2009).

In the fully-developed region, vortexes penetrate downward into the canopy layer. The vertical penetration depth (δ_e) is defined basing on the distribution of Reynolds shear stress, which reaches its maximum value at top of the canopy and diminishes progressively deeper into the canopy. Thus, the depth of vortex penetration corresponds to the location from the canopy top where turbulent stress fades to an insignificant level, that is the vertical position where the Reynolds stress decreases to 10% of its peak. The penetration depth was found to be inversely dependent on canopy resistance C_D and frontal area a (H. Nepf et al. 2007, Yan, Jia, et al. 2023, M. Liu et al. 2024):

$$\frac{\delta_e}{h} = \frac{0.23 \pm 0.06}{C_D a h},$$

and roughly coincides with the inner inflection point of the velocity profiles. The flow above submerged canopies has thus been divided in three sub-zones, as depicted in figure 2.2, (Nezu and Sanjou 2008 Okamoto and Nezu 2009):

1. **Emergent zone** ($0 \leq y \leq h_P$), extending from the bottom wall of the domain to the penetration height h_P, which corresponds to the vertical location from the channel bed where turbulent stress decreases to 10% of its maximum value. This region is characterized by a small vertical turbulent momentum transport and an almost-constant velocity due to the shielding effect exerted by the filaments on the incoming flow;

2. **Mixing-layer zone** ($h_P \leq y \leq y_{vo}$), extending between the penetration height and the virtual origin, dominated by large-scale coherent vortexes;

3. **Log-law zone** ($y_{vo} \leq y \leq H$), extending above the virtual origin and resembling boundary layers, with the velocity profiles obeying the log-law distribution.

The coherent vortexes forming in the mixing layer zone contribute to the momentum and mass exchange at the top of the canopy. Ejections are responsible for moving low-speed flow from inside the canopy to the outside, while sweeps are responsible for moving high-speed fluid from within the canopy (Nezu and Sanjou 2008). For unobstructed channels the largest sweeps and ejections occur in the near-bed region, with ejection events typically contributing more than sweep events (Nakagawa and Nezu 1977). Therefore, when submerged vegetation is present, as the log-layer resembles a boundary layer, ejection dominate near the canopy top. On the other hand, sweep events become the primary contributors within the canopy (Nezu and Sanjou 2008, Cui and Neary 2008).

Many parameters influence the characteristics of flow interacting with submerged canopies, including canopy density. Submerged canopies are often categorized as sparse or dense, based on the balance between turbulent stress and canopy drag in affecting momentum. In sparse canopies, the flow profile resembles that of a turbulent boundary layer, where turbulent stress remains high near the bed,

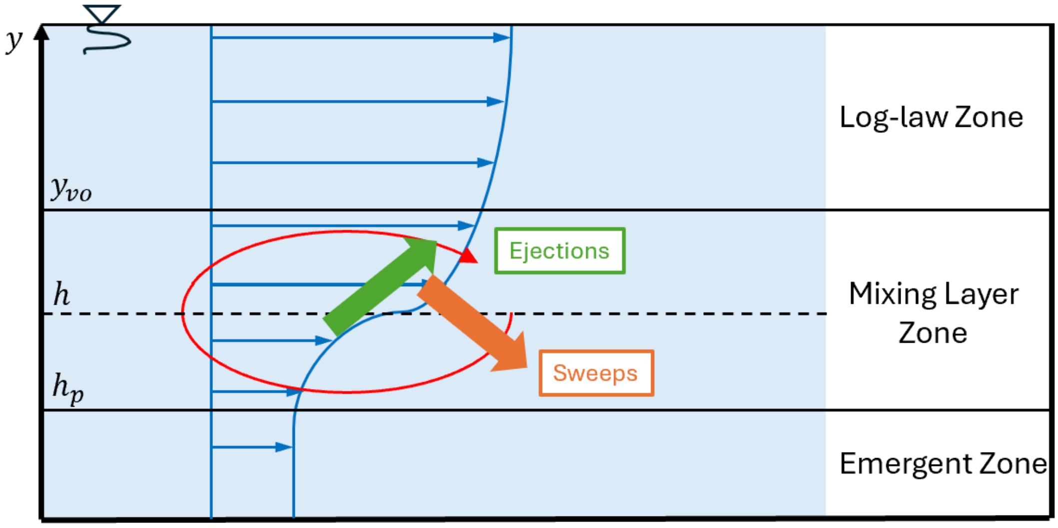

Figure 2.2: Division of the flow above a generic fully-distributed submerged canopy in three sub-zones. y_{vo} is the virtual origin, h is the canopy height and h_p is the penetration height. The emergent zone is characterized by small momentum exchange, the mixing-layer zone is dominated by large scale coherent vortexes, while in the log-law zone the velocity profiles follow the log-law (figure adapted from Nezu and Sanjou 2008).

resembling conditions similar to a non-vegetated channel. In contrast, shear-scale vortexes generated by the Kelvin-Helmholtz instability penetrate into dense canopies over a distance δ_e, reducing near-bed turbulent stresses compared to canopy-free flows. This has implications for sediment deposition, as suspended sediment concentration decreases with increasing canopy density (C. Liu, Gao, et al. 2019). The influence of canopy density also affects the development of mixing layer instability. A denser canopy reduces vertical exchange between the canopy and the overlying flow while intensifying the mixing layer, as observed by Fang et al. 2022.

Flexibility also significantly impacts canopy-flow interactions. When flexible canopies deflect under the incoming flow, their effective height decreases, shifting the canopy shear layer closer to the bed, which enhances near-bed turbulence levels considerably (Abdolahpour et al. 2018). Additionally, as the relative velocity between the filaments and the flow decreases, and with a reduced frontal area, the drag exerted by flexible canopies is lower than in the rigid canopy scenario (Alben et al. 2002).

Another significant parameter when dealing with submerged canopies is the submergence relative depth, defined as the ratio between the height of the channel and the height of the filaments. This means that, at fixed canopy height h, the higher is the height of the channel H, the higher is the submergence relative depth. For small submergence depth, the log-law zone of the shear layer disappears and the shear layer is divided only between the emergent and the mixing-layer zones. Additionally, the average length scale of coherent vortexes in the mixing layer depends on the submergence ratio, increasing in a linear relationship as water depth gets higher (Nezu and Sanjou 2008).

2.2 Partially-distributed Emergent Canopies

In contrast to the full canopy scenario, where all filaments are entirely submerged, an emergent canopy consists of filaments that extend above the water surface due to their height exceeding the water depth. This makes it more insightful to focus on vegetation patches emergent in shallow water rather than a fully vegetated channel bed. Consequently, even if emergent canopy patches are characterized by a lateral edge, in contrast to the horizontal edge found in a fully submerged canopy, the problem is still bi-dimensional.

As the unperturbed flow hits a vegetated region, the flow adjusts over a length scale proportional to the canopy width. Rominger and H. M. Nepf 2011, indeed, suggested that the flow adjustment length depends on the canopy drag coefficient C_D, the vegetation density a and the width of the canopy region D, and provided an estimation of the flow adjustment length L_a:

$$L_a = \begin{cases} (3.0 \pm 0.3)\sqrt{\frac{2}{C_D a}(1 + (C_D a D)^2)} & C_D a D < 1, \\ (5.5 \pm 0.4)\sqrt{\left(\frac{2}{C_D a}\right)^2 + D^2} & C_D a D \geq 1. \end{cases}$$

Given the difference in velocity between the flow in the vegetated region and the flow in the main channel, a shear layer forms along the flow-parallel edges. Its width, measured by the momentum thickness θ as for the fully-distributed submerged canopy, starts growing until it reaches a fully developed state downstream of the adjustment region (White and H. M. Nepf 2008, Rominger and H. M. Nepf 2011). The existence of both vegetated and non-vegetated regions within the channel results in flow characteristics showing a dependence on the transverse direction, with mean velocity profiles stabilizing to a quasi-equilibrium shape in the transverse direction, reaching a condition which resembles the open channel scenario (W.-X. Huai et al. 2019). The shear layer, analogous to the one forming in the fully-distributed submerged canopy, is characterized by an inflection point in the mean velocity profile along the transverse direction, similar to the well documented inflection point observed near the canopy tips in the vertical direction for fully distributed canopies (White and H. M. Nepf 2007, Rominger and H. M. Nepf 2011, Dupuis et al. 2017, W.-X. Huai et al. 2019). As already pointed out, as for the Rayleigh Theorem (Rayleigh 1879), an inflection point in the velocity profile is a necessary

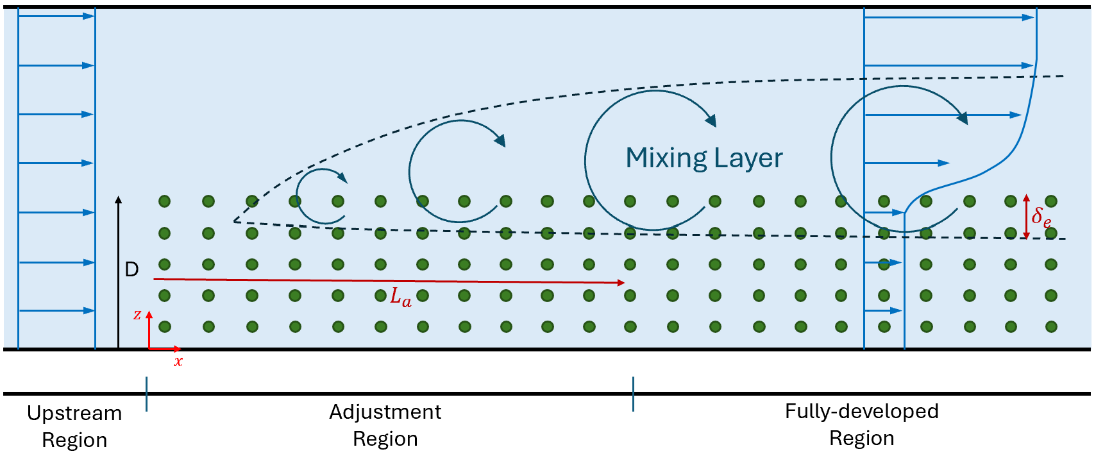

Figure 2.3: Mixing layer development at the lateral edge of a generic partially-distributed emergent canopy. Downstream of an adjustment length L_a, the flow reaches a fully-developed state. Coherent vortex structures penetrate into the vegetated area of a horizontal depth δ_e, thus governing the momentum exchange with the main channel (figure adapted from Yan, Jia, et al. 2023).

condition for flow instability, thus leading to horizontal coherent vortex structures forming in the shear layer and growing to a finite size within this layer when the fully-developed state is reached (White and H. M. Nepf 2008, Rominger and H. M. Nepf 2011, W.-X. Huai et al. 2019). The horizontal coherent vortexes penetrate into the vegetated region, thus, similarly to fully-distributed submerged canopies, an horizontal penetration depth δ_e can be defined. An empirical estimation was provided by White and H. M. Nepf 2008:

$$\delta_e = max[0.5(C_D a)^{-1}, 1.8d],$$

where d is the diameter of the cylinders. For sufficiently large values of $C_D a$ such that $(C_D a)^{-1}$ is smaller than the diameter of the cylinders, the penetration depths was shown to be independent of $C_D a$, reaching a constant value which depends only by the diameter of the cylinder. This occurs because the velocity transition cannot begin before reaching the first row of cylinders and lower values of $C_D a$ would prevent this condition from being met. Consequently, a minimum limit is set for the penetration depth.

Given the characteristics of the shear layer, it resembles more a mixing layer and

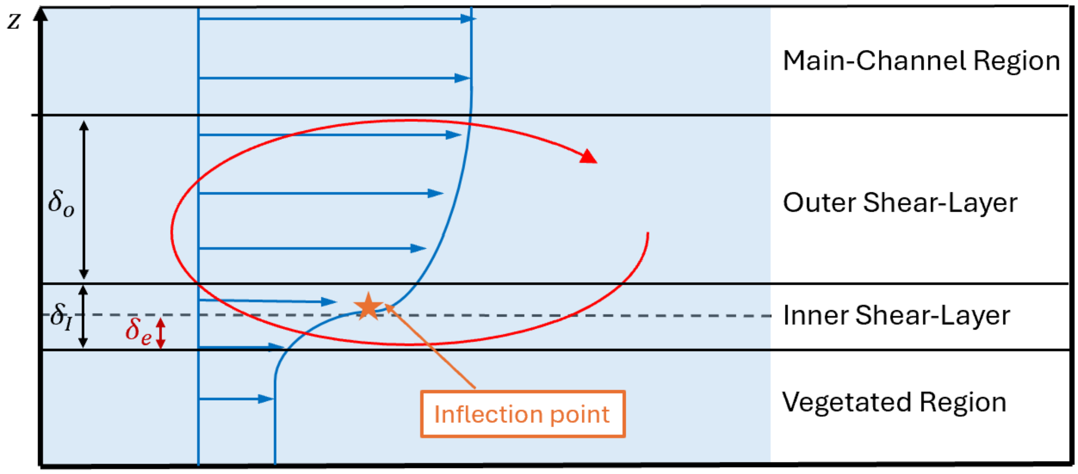

Figure 2.4: Flow regions in a generic partially-distributed emergent canopy, with the main-channel and the vegetated regions show laterally-uniform velocity profiles and a two-layer shear-layer structure. The inner shear-layer δ_I has the characteristics of a mixing layer and, by penetrating into the vegetated region of δ_e, controls the momentum at the interface. The outer shear-layer δ_O resembles a boundary layer and lays in the main-channel, dictating the scale of the horizontal vortexes.

is asymmetric about the interface between the vegetated and the non-vegetated regions, showing a two-layer structures. Therefore, the flow can be divided into four regions (White and H. M. Nepf 2007, White and H. M. Nepf 2008):

1. **Vegetated region**, characterized by laterally-uniform flow;
2. **Inner shear layer**, penetrating into the vegetated region of a penetration length δ_e, resembling a mixing layer because of the inflection point in the velocity profile, similarly to the one of the fully-distributed submerged canopies. It shows the maximum shear near the interface, thus establishing the length scale of the penetration of momentum into the vegetated region;
3. **Outer shear layer**, resembling a boundary layer, forms in the main non-vegetated channel and, by dictating the scale of the vortexes at equilibrium state, determines the main channel boundary layer width.
4. **Main channel** outside the region of shear, characterized by laterally-uniform flow.

In the fully developed state of the flow, the abrupt transition from the fast-moving channel flow to the slower, obstructed flow within the vegetation generates high shear at the lateral edge. This shear influences both the turbulence intensity and the distribution of transverse Reynolds shear stresses, which peak along the interface between the emergent riparian vegetation and the main channel. Consequently, the mutual interaction between these two distinct regions is substantial, with horizontal coherent vortexes, generated by the inflectional instability, playing a primary role. In particular, near the interface, sweeps and ejections contribute significantly to the Reynolds stress, with sweeps having a greater influence than ejections within the vegetated area. Consequently, vortex structures induce strong cross-flows at the interface, where sweeps draw flow inward from the main channel and ejections drive outflow from the vegetation array, leading to intense momentum and mass fluxes across the lateral boundary. On the other hand, near-bed shear stresses are reduced within the vegetated zone compared to the non-vegetated region (Nezu and Onitsuka 2001, Bennett et al. 2002, White and H. M. Nepf 2007, White and H. M. Nepf 2008, W.-X. Huai et al. 2019).

2.3 Fully Submerged Canopy Patches

Although the fully-obstructed channel with submerged vegetation and the partially-obstructed channel with emergent vegetation are well-studied scenarios, whose turbulence dynamics and vortex generations are deeply described in literature, they can only partially describe finite patches of vegetation. In fact, presenting two homogeneous directions, they represent bi-dimensional flows and so flow characteristics. However, when horizontal and lateral interfaces, at the top and lateral edges of the canopy respectively, coexist, multidimensional coherent vortexes and turbulence-induced secondary flows may drive complex mass and momentum exchanges between the canopy region and the surrounding open water (Yan, Duan, W.-H. Wai, et al. 2022, Unigarro Villota et al. 2023,Yan, Jia, et al. 2023).

As for the other analyzed scenarios, the elongated elements can be modeled as either rigid or flexible, with the latter ones being part of a fluid-structure interaction problem. Canopy patches, regardless of their structural flexibility, represent zones of high flow resistance, causing flow to deflect and interfere with bad erosion and sediment transport (Colomer and Serra 2021, W.-x. Huai et al. 2021). In fact, the blockage opposed by the vegetation causes more water to flow in the non-vegetated region and the difference in velocity above and within the vegetation cause a shear layer both above the canopy and at the lateral interface, which leads to the generation of vertical and horizontal vortex structures respectively (Devi and Kumar 2016b, Yan, Duan, W.-H. Wai, et al. 2022). Due to the generation of coherent vortexes, high-momentum flow from outer open water regions is transported into the vegetation canopy in the transverse direction and vertical direction, while low-momentum flow inside the vegetation canopy is transferred into the outer open water region (Yan, Jia, et al. 2023).

2.3.1 Rigid vegetation

Most studies on canopy patches to date have modeled the vegetation stems as morphologically simple elements, such as rigid cylinders. Although it represents a pure fluid-dynamics problem, as there is no a coupled effect between the fluid and the filament dynamics, it shows some characteristic features of the problem.

When describing the flow characteristics in a turbulent channel fully-covered by submerged vegetation or partially-obstructed by emergent vegetation, an adjustment length was present at the leading edge of the canopy, after which the flow reaches a fully-developed state and the size of the shear layer reaches a constant size. Yan, Jia, et al. 2023, using plastic cylinders to model rigid vegetation, found that the adjustment distance was shorter within a submerged partially-distributed canopy compared to a submerged fully-distributed canopy. On the other hand, for both submerged and emergent partially distributed canopies, the adjustment distances were found to be comparable, thus, the flow adjustment distance can be estimated with the formula proposed by Rominger and H. M. Nepf 2011. They also highlighted the so-called *velocity reversal phenomenon*. During the flow adjustment, the velocity just below the canopy top in the Junction Region, initially, was overall smaller than that deeper inside the Vegetated Region, while this trend gradually reversed further downstream.

When the flow becomes fully-developed, the velocity are altered across three regions — the vegetated zone, the non-vegetated zone, and the interface between them. In the non-vegetated area, the velocity profiles are similar to those of open channels without vegetation, thus resembling a boundary layer. In contrast, the profiles within the vegetated zone align with those observed in fully vegetated flows. At the interface between the two regions, velocity profiles exhibit a quasi-linear shape due to the combined influences of both zones (Nezu and Onitsuka 2001). Particularly, since the flow in the canopy region still maintains a mixing-layer behavior dominated by vertical coherent vortexes, this suggests that when the width of the patches is sufficiently large, the neighboring open water appears to not influence the canopy-side flow, even if horizontal coherent vortexes were formed at the lateral edge below the canopy top. Similarly, when getting further away from the junction in the unvegetated side of the channel, the particular vertical flow structure gradually shifts to the wall-bounded pattern, characteristic of open channel flows. However, the flow behavior near the boundary between the vegetated and the non vegetated regions is more complicated, as the effects of the horizontal and vertical vortexes exert a combined effect, with the junction momentum exchange playing a key role in determining the vertical flow structure in both the canopy side and the neighboring open water side of the shear layer (Yan, Duan, W.-H. Wai, et al. 2022, Yan, Jia, et al. 2023).

In the near-lateral junction region of the canopy patch, at the neighboring open-water side, the flow is influenced by both the horizontal and vertical shear layers. In fact, the presence of the canopy causes a deflected pattern on the vertical flow structure due to the transverse extension of the vertical coherent vortexes which arise above the vegetated region, differing significantly from the horizontal shear layer in fully-distributed canopies that decays above the canopy top. Given also the lateral outward extension in the neighboring open water region of the vertical shear layer, the vertical flow structure on the neighboring open side still follows a mixing-layer pattern for regions near the junction. (Yan, Duan, W.-H. Wai, et al. 2022). Thus, basing on the vertical velocity profiles, the water depth in the near-junction region can be divided into three sub-regions, each governed by a particular physical mechanism (Yan, Jia, et al. 2023):

- **Wall-subregion**, where the horizontal vortexes arising on the side of the canopy, as described for emergent vegetation, don't have much influence to the flow, as they are inhibited by the bed, thus resembling a wall-bounded flow.
- **Deflection sub-region**, where transverse Reynolds stress become pronounced as the coherent vortexes at the lateral edge become more pronounced.
- **Mixing-subregion**, where vertical vortexes become more important while horizontal coherent vortexes become less important. The flow in the mixing subregion nearly complies with the turbulent mixing flow theory, the velocity profile of which might be described by the tangent hyperbolic curve.

In particular, Yan, W.-H. O. Wai, et al. 2016 highlighted how the neighboring open water region near the lateral interface the combination of the bed effect and transverse coherent vortexes leads to a highly anisotropic flow field. In the near-bed region, bed friction plays the dominant role in controlling the flow structure, since it significantly suppresses formation of horizontal coherent vortexes, leading to poor momentum exchange between vegetation and non-vegetation regions. The low momentum from the vegetation region is transferred to the neighboring open water region with high momentum, resulting in reduction of the longitudinal velocity. On the other hand, large-scale coherent vortexes arising from both the top and lateral edges of the canopy both coexist near the canopy top corner, where three-dimensional mass and momentum exchange are present (Yan, Duan, W.-H. Wai, et al. 2022)

As suggested by Yan, Duan, W.-H. Wai, et al. 2022, in submerged canopy patches, secondary circulation caused by turbulence anisotropy, plays a fundamental role, impacting mass and momentum exchange. In fact, due to the coevolution of multidimensional - vertical and horizontal - coherent vortexes, turbulence anisotropy arises, influencing both the mean flow and the turbulence field. Turbulence anisotropy also occurs due to the spatially nonuniform distribution of unidimensional vortexes, such as the bed tending to inhibit horizontal coherent vortexes.
Naot et al. 1996 proposed an algebraic stress model obtained from the stress transport equations to study turbulence anisotropy. A simpler approach was adopted by Yan, Duan, W.-H. Wai, et al. 2022, who studied turbulence anisotropy by evaluating the difference in vertical and transverse components of Reynolds shear stresses. They showed the existence of a negative anisotropic zone $\overline{u'v'} - \overline{u'w'} < 0$ along the canopy top edge and positive anisotropic zone $\overline{u'v'} - \overline{u'w'} > 0$ along the canopy lateral edge, which indicate the domination of the vertical and transverse coherent vortexes, respectively. However, the turbulence anisotropy

effect diminishes near the canopy top corner, which means that the turbulent effect induced by both vertical and transverse dimensions is equivalent even though the resultant turbulence attains the maximum. D. Li et al. 2022, highlighting the strong momentum exchange occurring in the mixing layer, where the fluctuating streamwise and lateral velocity components contribute to the Reynolds stresses $-u'w'$, showed that peaks of the Reynolds stress occur in the main channel at the leading edge of the canopy patch, as a result of the diverging flow caused by the blockage of the vegetation. The Reynolds stress increases with the distance downstream, and its peak shifts towards the canopy.

Given the importance of secondary currents, Yan, Duan, Y.-H. Zhang, et al. 2023 further analyzed the momentum fluxes across the different interfaces of the partially-distributed submerged canopies, concluding that advection momentum fluxes, generated by secondary circulations, are equally important as Large Scale Vortexes-driven diffusion momentum fluxes near the mixing interfaces. The turbulence anisotropy-caused secondary flows are responsible for the exchange of fluid between the vegetated and the non-vegetated regions. For example, they noted a near-bed clockwise circulation which enables a mean negative transverse velocity from the neighboring open water to the vegetation canopy above the bed, resulting in high-momentum flow being transferred at the junction. Unigarro Villota et al. 2023 highlighted the presence also of tertiary circulations for high density patches, whose size and strength is smaller and whose rotational direction is opposite with respect to the secondary circulation.

Other phenomena were found to alter the flow structure in partially-obstructed channels with submerge vegetation. AS an example, Devi and Kumar 2016a using steel tube structure, studied the change in flow characteristics of alluvial channel occupied by submerged vegetated patches of different spacing under downward seepage condition. In particular, they concluded that the pattern of vegetation inside the patches has an impact on the drag distribution, with low vegetation spacing offering more resistance to the flow with respect to high spacings which, instead, allow the flow to enter the canopy region. On the other hand, downward seepage has an effect on the near-bed velocity, which is increases with respect to the case without seepage, suggesting that other kind of circulation arise in the domain. Nevertheless, they concluded that the distribution of Reynolds stresses seem to not be affected neither by the spacing between stems, nor by the seepage condition, with the maximum value always laying near the vegetation top, thus further highlighting the importance of turbulence generated in this region. However, the quadrant analysis showed that, when there is a downward seepage, ejections and sweeps have an equal contribution in the region just above of the canopy, unlike in the no seepage case which is dominated by ejections.

J. Zhang et al. 2020, instead, considered the impact of vegetation density and extension, as well as the distance from the vegetation leading edge on the evolution of velocity, turbulent kinetic energy, and net deposition within a submerged vegetation. They concluded that vegetation density has an impact on the deceleration of the flow, with velocity decreasing in the adjustment region inversely proportional to dimensionless vegetation density. In the fully developed, instead, vegetation density, along with water depth ratio and channel bulk velocity, has an impact on the net deposition of sediment and species. Moreover, they concluded that when the width of the vegetation is significantly larger than its height, the deceleration induces a vertical updraft, which plays a key role in transporting sediments away from the bed.

2.3.2 Flexible and Nature-Inspired Vegetation

When the filaments are flexible, other effects may arise due the combined interaction between the flow and the structures. For example, Zeng and C.-W. Li 2014 highlighted how the leading edge of a finite-length canopy patch deflects more and vibrates violently if compared to filaments in the fully-developed region. This effect may reduce the vegetation resistance and slightly increase the length of the intrusion region as compared to the results obtained with rigid vegetation.

Given the complexity in realizing the setup of flexible canopy patches, not many studies are to be found in literature to date. Zeng and C.-W. Li 2014 simulated semi-rigid vegetation patches using plastic strips with rectangular cross-sections. It was observed that, beyond the leading edge of the canopy in the intrusion region, the streamwise velocity gradually decreased within the vegetation canopy while increasing above it. This deceleration of streamwise velocity within the canopy was accompanied by vertical flow to maintain water mass balance. Consequently, part of the water entering the canopy was slowed down, while the majority was deflected upward. Furthermore, an analysis of the vertical turbulent shear stress, $u'v'$, revealed that its peak values occurred at the deflected height of the horizontal edge when the flow reaches a fully-developed state. These findings support the validity of modeling the top edge of vegetation patches using the two-dimensional approach of the fully-distributed submerged canopy model.

Pang et al. 2014 conducted a flume experiment on a patch of submerged *eel grass* - a highly flexible herbaceous plant common in Chinese lakes - using Acoustic Doppler Velocimetry (ADV) technique to measure time-averaged velocity, turbulence intensity, and shear stresses. Results indicated that vertical streamwise velocity profiles within the plant patch display an S-shaped pattern from canopy to root, a shape that is more irregular than that for more rigid plants, reflecting the extremely flexible nature of *eel grass*.

Unlike simpler plant structures, the *eel grass* foliage floats and interacts with the flow in a more complex manner. Thus, within the canopy patch, turbulence intensity peaks at the canopy top, where foliage movement is most pronounced. It rises from the water surface down to the canopy and then declines from the canopy to the roots, with a turning point at the canopy top level. As turbulence is responsible for the exchange of flow, mass and momentum fluxes are high in this location. The quadrant analysis revealed a predominance of sweep events below the canopy, while ejections dominate above and at the canopy top, similarly to what happens in fully-distributed canopies. However, ejections interact with sweeps, thus, higher-speed fluid transported by sweeps around the canopy mixes with lower-speed fluid brought up from near the bed by ejection or outward interactions. reducing flow, momentum and energy and influencing sediment and pollutant transport. These unique turbulent patterns are likely a result of the irregular motion of eelgrass foliage, which affects turbulent flow differently than artificial rigid or flexible plant models.

Devi and Kumar 2016b conducted experimental measurements on a turbulent channel partially covered by submerged flexible rice stems, at different transverse locations to explore the difference in flow characteristics in the vegetated and non-vegetated regions and at the junction between the two. They highlighted the role of vegetation in the flow path in redirecting the flow from the vegetated area towards the non-vegetated region, resulting in erosion within the non-vegetated zone. This is attributed to the fact that, as flow progresses downstream, an increase in flow properties like velocity, Reynolds stress, and turbulence intensity is observed in the non-vegetated region, while the reduction in these flow characteristics within the vegetated zone suggests that the flow is intensified in the non-vegetated zone. An examination of the Reynolds stress distribution shows also in this case that peaks occur near the canopy top within the vegetated region and close to the bed in the open water, indicating these locations as primary sources of turbulence in their respective zones. Elevated Reynolds stress and turbulence intensities also appear at the boundary between vegetated and non-vegetated areas, likely due to lateral flow and momentum exchange across this interface. Again, quadrant analysis highlights the significant roles of sweeps and ejections in momentum transfer between regions, with sweeps notably dominant within the vegetated zone.

Caroppi et al. 2021 investigated the impact of incorporating natural plants through experimental simulation of a flow in a partly vegetated channel, using Acoustic Doppler Velocimetry (ADV). They found that, with respect to rigid cylinders, lateral flow distributions were governed by factors like shear layer differential velocity, bulk vegetative drag, and the presence of large-scale vortexes. However, the flexible, natural-like vegetation introduced unique flow-altering mechanisms, especially at the junction between the vegetated side and the open water region. Features like plant morphology, spacing, and the dynamic movement of flexible foliage enabled vortexes to penetrate deeper into the vegetated zone, with shear penetration being $6-10$ times greater than that for rigid cylinders, expanding the areas for momentum exchange with adjacent open water significantly. Moreover, lateral momentum transport efficiency in cases with flexible foliated vegetation was up to 40% higher than in rigid cylinder setups. This suggests that natural riparian systems with flexible vegetation allow for more extensive and efficient momentum transfer across vegetated interfaces and within the canopy compared to rigid vegetation models.

The above mentioned scenarios suggested that modeling submerged vegetation as rigid cylinders fails to accurately replicate vegetated shear layers influenced by reconfiguring foliage, highlighting the importance for major improvements in representing natural-like vegetation to better understand flow processes in partly-vegetated natural systems like rivers.

2.4 Filament Dynamics

Several studies focused on characterizing the behavior of plants and filaments when hit by an incoming flow, given its importance on natural and industrial processes. For instance, the movement of vegetation may alter the photosynthesis of the plants, since it alters the amount of light which reaching plants through shedding, but also the growth of the plants themselves (Sinoquet et al. 2001, H. M. Nepf 2012). Another example includes new technologies focused on the production on clean photovoltaic using of high efficiency flexible inorganic films and photovoltaic fibers and filaments, for which the flux of light hitting these structures must be maximized (Dolez 2021).

When examining flexible filaments affected by flow, a strong coupling between the dynamics of the fluid and the structure exists, as the filaments not only alter the fluid behavior above the canopy but are also influenced by the flow itself. Therefore, a deep understanding of the couple dynamic is essential. Py, E. D. Langre, et al. 2006 developed a fully coupled model in which wind fluctuations and plant dynamics interact via a drag term, which impacts canopy dynamics and is therefore integrated into the linearized momentum equation. This allowed to demonstrate that a lock-in mechanism arise, similarly to that observed in vortex-structure interaction problems, thereby further illustrating the strong coupling between the filaments and fluid behavior.

The impact of fluid flow over canopies causes the flexible filaments to bend due to the currents, leading to a morphological change known as *reconfiguration* (Vogel 1994), which results in a more streamlined shape (E. d. Langre 2008, Tschisgale et al. 2021). A flexible body hit by a flow or a current adjusts its shape until the drag force is balanced by the restoring force generated by its stiffness (H. M. Nepf 2012). Reconfiguration depends on the Cauchy number, which influences shape changes in plants exposed to flow and decreases the effective cross-sectional area exposed to the flow, with implications on the drag exerted by the filaments (E. d. Langre 2008, H. M. Nepf 2012). Indeed, flexible systems bending in steady flows are known to experience reduced drag compared to their rigid counterparts (Alben et al. 2002, Leclercq and E. d. Langre 2016). As highlighted by Alben et al. 2002, the classical theory of high-speed flows fails to predict the drag exerted by flexible filaments, as it estimates the drag exerted by moving rigid objects as a quadratic law of the velocity. However, the reshaping of flexible filaments is speed-dependent, causing plant drag to increase more gradually than what the quadratic law would predict. The drag force is predicted to scale as $D \propto U^{2+\gamma}$, where γ is the Vogel exponent, whose value falls in between 0 and -0.7 (H. M. Nepf 2012) with an estimated value of $\gamma = -2/3$ by Alben et al. 2002.

As mentioned in section 2.1, the Kelvin-Helmholtz instability present in the mixing layer above canopies generates vortexes that are advected downstream by the mean flow, resulting in a waving motion of the vegetation referred to as *homani/monami* (Ackerman and Okubo 1993). Several studies focused on characterizing this collective motion of the filaments. Fang et al. 2022 focused on a deep characterization of the interaction between fluid and vegetation canopy within the mixing layer forming on top of it due to the coherent vortexes arising, as previously described. In the case of less rigid canopies, their resistance to the flow is minimal, resulting in a static reconfiguration where the filaments are fully deflected. This configuration acts as a barrier, inhibiting the vertical exchange of momentum between the interior and exterior of the canopy. As bending rigidity increases, a flapping state occurs, characterized by greater resistance from the filaments while they remain less deflected, permitting a vertical movement of low-energy flow from within the canopy to the outside. Following this, a transitional dual state is observed, where only patches of vegetation exhibit flapping behavior, leading to a regular waving state when the bending rigidity is sufficiently high. Finally, a rigid static state is reached when the filaments become almost completely non-flexible: the filaments are less deflected but still exhibit coherent motion.

Ghisalberti and H. M. Nepf 2002 gave an explanation for the mechanism generating the *monami/honami*. When boundary layer flow meets vegetative drag, the lower fluid slows down, redirecting the flow above the canopy. This creates a mixing layer profile where Kelvin-Helmholtz instabilities arise, forming coherent vortexes sustained by the shear at the canopy top and moving downstream. As a result, plants experience a sequence of vortexes and an oscillating streamwise velocity, which induces a synchronized, progressive waving motion in the vegetation. The *monami/homani* motion characterizes all canopies, irrespective of filament flexibility, as demonstrated by Monti, Olivieri, et al. 2023 through direct numerical simulations. Consequently, the most flexible canopy exhibits passive behavior, being entirely driven by the turbulent flow and not displaying the structural response of the filaments, as also pointed out by Tschisgale et al. 2021.

When turbulent flows hit a clamped flexible fiber, two oscillating states are to be found, one in which the natural structural response dominates, thus the filament vibrates at his natural frequency f_{nat} and another one where the fiber oscillates at the characteristic frequency of the largest turbulent eddies f_{turb}. Later on, Rota et al. 2024 demonstrated that this applies also for flexible canopies with filaments fully-distributed on the bottom wall of the domain. While the first scenario is characteristic of the most rigid filaments, the latter scenario corresponds a motion of the filament which is compliant with that of the flow, independently on its structural parameters (Foggi Rota et al. 2024). Py, E. D. Langre, et al. 2006 referred to the state in which the instability frequency locks onto the swaying frequency of the plants as *lock-in*. The lock-in effect confirms that the governing mechanism for the dynamic motion of vegetation is indeed a coupling of the mixing layer and structural property.

2.5 Numerical Simulations of Canopy Flows

The majority of the studies in literature concerning canopy flows are experimental. Rigid plants are usually modeled as cylinders made of wood (e.g. C. Liu, Hu, et al. 2018), plastic (e.g. Yan, Duan, W.-H. Wai, et al. 2022) or steel (e.g. Devi and Kumar 2016a), while flexible filaments are represented either by real vegetation (e.g. Py, E. d. Langre, et al. 2005, Pang et al. 2014, Caroppi et al. 2021) or flexible plastic fibers (e.g. Zeng and C.-W. Li 2014).
Different experimental approaches have been adopted. For example, Py, E. d. Langre, et al. 2005 used Particle-Imaginery-Velocimetry (PIV) algorithms. However, Acoustic Doppler Velocimetry (ADV) is the most widely used (e.g. Pang et al. 2014, Caroppi et al. 2021). Moreover, to highlight large-scale coherent structures arising in canopy flows, tracer dye visualization have been performed. For example, C. Liu, Hu, et al. 2018 used fluorescein dye excited by a ultraviolet light, while Yan, Duan, W.-H. Wai, et al. 2022 used green tracer dye. However, as highlighted by Monti, Olivieri, et al. 2023, experimental investigations face significant technical

challenges, particularly in measuring the spatial configuration of fluid flow within the canopy region and isolating the effects of various governing parameters, such as the Cauchy and Reynolds numbers, the solid-to-fluid density ratio, and reduced velocity. These challenges can be addressed by complementing experimental studies with computational approaches, such as direct numerical simulations (DNS) or large-eddy simulations (LES), which provide valuable support in analyzing these complex dynamics.

The mathematical characterization of canopy flows remains an area of active theoretical investigation, with ongoing efforts to develop models that capture the phenomena accurately without imposing overly restrictive simplifications. Cui and Neary 2008 highlighted how Reynolds-Averaged Navier-Stokes (RANS) models with isotropic turbulence closures successfully simulate the time-averaged flow features, but are not universal and provide only limited descriptions of turbulence statistics, since they solve Reynolds equations for the mean velocity field, while the Reynolds stresses, which appear as unknowns, are modeled. Among the different closure models, Rahimi et al. 2023, for example, used the $k - \varepsilon$ closure model. Large Eddy Simulation (LES) appeared to be in fairly good agreement with the measurements, but there are no significant improvements compared to RANS simulations, as sown by Cui and Neary 2008. Their study demonstrated the capability of LES models in providing detailed information about the tridimensional turbulence field and anisotropy of the Reynolds stresses, which seemed to be really difficult to obtain using even the most advanced experimental methods.

Direct Numerical Simulations (DNS) are employed to achieve a high level of accuracy in the analysis of turbulence and turbulent flows. DNS has proven invaluable in complementing experimental studies by offering detailed insights that are unattainable through other methods. However, the main limitation of DNS lies in its substantial computational cost, which scales approximately with Re^3 for turbulent channel flows. This steep increase in computational expense with higher Reynolds numbers restricts DNS to low or moderate Reynolds number flows. Despite this limitation, the Reynolds numbers characteristic of canopy flows typically fall within the range that DNS can effectively handle (Pope 2000).

2.6 Present Thesis

Although the works presented by Yan, Duan, W.-H. Wai, et al. 2022, Yan, Duan, Y.-H. Zhang, et al. 2023, Yan, Jia, et al. 2023 and Unigarro Villota et al. 2023 are one step forward in the study of the complex phenomena and turbulence dynamics happening in fully submerged canopy patches, they do not account for the majority of natural scenarios. Indeed, the vegetation in still modeled as rigid cylinders, while in most real applications of these kind of flows vegetation needs to be modeled as flexible elements. Pang et al. 2014 and Caroppi et al. 2021 went one step further, considering complex geometries which aim to resemble aquatic plants with branches like *Potamogeton Malaianus* or *Myriophyllum Spicatum.* On the other hand, flexible filaments are frequently employed to simulate the response of underwater seagrass like *Zostera Marina* or *Vallisneria Spiralis.* While rigid cylinders represent a pure fluid-dynamics problem, the importance of the fluid-structure interaction in flexible canopy patches is still an interesting scenario, which needs further investigation. Indeed, understanding the filaments motion regimes may give interesting insight in many fields.

Another important aspect of research on canopy flows involves their mathematical modeling. It has been observed that the majority of studies addressing canopy flows rely predominantly on experimental techniques. While this experimental approach is effective for investigating rigid canopies, certain challenges arise when dealing with flexible elements. For instance, although the movement of plants and vegetation in response to fluid flow is visually apparent, accurately measuring this motion presents several difficulties. As highlighted by E. d. Langre 2008, most plants are characterized by their lightweight and flexible structures, which contrasts sharply with the properties of most devices used for displacement monitoring. Even minor modifications, such as adding a few grams or attaching a small spring to a plant organ, can significantly alter its dynamics and consequently affect the results. Furthermore, while Reynolds-Averaged Navier–Stokes (RANS) and Large Eddy Simulation (LES) approaches are effective for capturing mean flow characteristics, Direct Numerical Simulation (DNS), despite its considerably higher computational cost, remains the most precise method for analyzing the complex interactions within canopy flows.

Given the aforementioned challenges, high-fidelity direct numerical simulations have been conducted as part of this thesis to investigate the flow within a partially obstructed channel containing submerged patches of vegetation. The primary objective is to analyze both the flow behavior and the dynamics of the filaments, with the goal of highlighting the interconnection between the two.

Chapter 3

Simulation Setup and Methods

3.1 Simulation Setup

3.1.1 Computational Domain

For each of the considered scenarios - canopy patch, full canopy and open channel - the computational domain consists in a three-dimensional box, whose dimensions are scaled with respect to the parameter H which denotes the height of the channel:

$$L_x \times L_y \times L_z = 2\pi H \times H \times 1.5\pi H$$

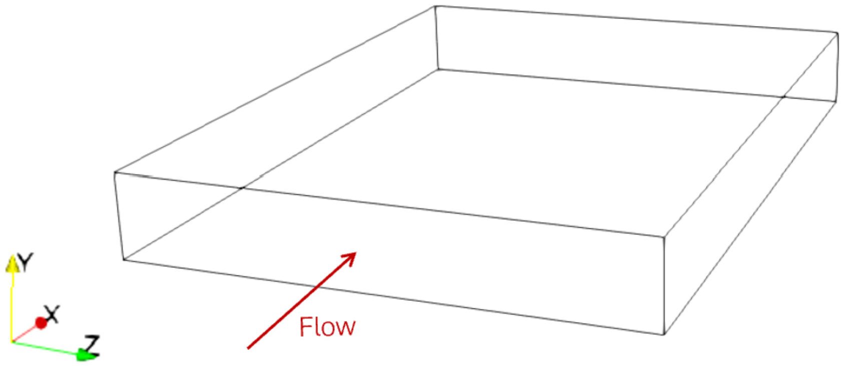

Figure 3.1: The Computational Domain is a box, whose dimensions $L_x \times L_y \times L_z = 2\pi H \times H \times 1.5\pi H$, where H is the height of the channel.

As highlighted by Rota et al. 2024, the domain length in the homogeneous direction is adequate to contain the largest turbulent structures, while the vertical extent of the domain with respect to the height of the filaments indicates that the simulated canopy is submerged.

A Cartesian right-handed reference frame is adopted, with the flow streaming in a direction aligned with the x axis. The y axis represents the wall-normal direction and extends vertically from the bottom wall of the channel, while the z axis corresponds to the spanwise direction and closes the reference frame, as in figure 3.1.

3.1.2 Filaments

While the open channel scenario does not include filaments, both the canopy patch and fully-distributed canopy configurations incorporate filaments that are clamped to the bottom wall of the domain. These filaments are arranged in a semi-random pattern to minimize preferential flow effects. In the fully-distributed canopy configuration, the filaments completely cover the bottom wall, whereas in the canopy patch configuration, the filaments occupy only a portion of the domain. This partial coverage divides the domain into two distinct regions: one vegetated and the other non-vegetated, as shown in figure 3.2. As a result, the arrangement of the filaments introduces an additional edge aligned with the streamwise direction, in addition to the horizontal edge formed at the top of the canopy.

To arrange the filaments, the vegetated region of the domain was divided into a grid

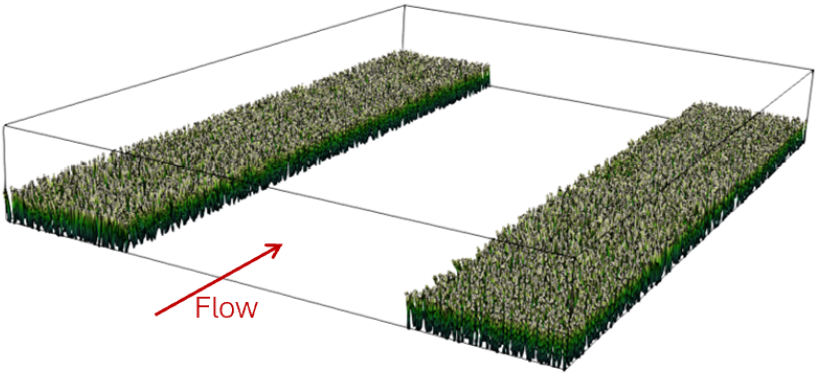

Figure 3.2: Configuration of the filaments in the computational domain for the canopy patch scenario. The bottom wall of the domain has been divided into $n_x \times n_z = 144 \times 54$ tiles, each containing a randomly allocated filament.

of $n_x \times n_z = 144 \times 54$ tiles for the canopy patch configuration and $n_x \times n_z = 144 \times 108$ tiles for the fully distributed canopy. Within each tile, a single filament was placed in a random position. Consequently, the canopy patch contains a total of 7776 filaments, while the fully distributed canopy includes 15,552 filaments. Each filament is modeled as a line of $n_L = 32$ Lagrangian points, which generalize the Euler-Bernoulli beam model. This approach allows for finite deflections while enforcing an inextensibility constraint. The undeflected height of the filaments is set to one-quarter of the channel height, such that $h = 0.25H$.

As introduced in Chapter 1, the flexibility of the filaments is described through the Cauchy number:

$$Ca = \frac{\rho_f d h^3 U_b^2}{2\gamma},$$

where ρ_f is the density of the fluid, h is the height of the filaments, U_b is the bulk velocity and γ is the bending rigidity of the filaments. It represents the ratio of the force exerted on the filament by the fluid to the restoring force exerted by the filaments. Two different values of the Cauchy number are considered, specifically $Ca = 10$ and $Ca = 100$. Since a higher Cauchy number corresponds to greater filament flexibility, the first value represents a scenario where the filaments are nearly rigid but still exhibit some bending under the influence of the flow. In contrast, the latter value corresponds to highly flexible filaments that fully deflect in response to the flow, capturing two limiting cases of filament behavior. This is further supported by the findings of Foggi Rota et al. 2024, who demonstrated that for sufficiently high Cauchy numbers ($Ca > 50$) the response of the filaments approach a frequency which is independent from their structural characteristics. Conversely, at lower Cauchy numbers, the filaments oscillate predominantly at their natural frequency.

3.1.3 Fluid Flow

We assume that the fluid can be modeled as an incompressible Newtonian fluid, governed by the mass conservation and the momentum balance equations:

$$\begin{cases} \nabla \cdot \mathbf{u} = 0, \\ \frac{\partial \mathbf{u}}{\partial t} + \nabla \cdot (\mathbf{u}\mathbf{u}) = -\frac{1}{\rho_f} \nabla p + \nu \nabla^2 \mathbf{u} + \mathbf{f}_{fib} + \mathbf{f}_{for}, \end{cases} \tag{3.1}$$

where $\mathbf{u}(\mathbf{x}, t)$ denotes the velocity field, ρ_f the fluid vdensity, $p(\mathbf{x}, t)$ the pressure field, ν the kinemantic viscosity. Two forcing terms have been taken into account: $\mathbf{f}_{fib}$ accounts for the presence of the filaments in the fluid flow describing the force field acting on the fluids and computed though a Lagrangian Immersed Boundary Method, while $\mathbf{f}_{for}$ is the homogeneous force field, uniformly applied to achieve at every time step the desired flow rate.

When performing numerical simulations of flow within a duct, an external forcing to drive fluid motion against viscous friction is required. Typically, this is achieved by maintaining a constant value for either the flow rate or the pressure gradient (Hasegawa et al. 2014). In order to obtain the desired flow rate, the forcing term $\mathbf{f}_{for}$ introduced in paragraph 3.1.3 is the pressure gradient, computed as:

$$\mathbf{f}_{for} = \frac{U_b - \hat{U}}{dt}\hat{x},$$

where $\hat{x}$ is the versor in the streamwise direction, dt is the simulation time-step, U_b is the bulk velocity and $\hat{U}$ is the streamwise velocity component averaged over the entire domain volume V

$$\hat{U} = \frac{1}{V}\iiint_V u dV,$$

Therefore, for all the considered scenarios, the bulk Reynolds number is constant and set to the value

$$Re_b = \frac{U_b H}{\nu} = 5000,$$

where H is the height of the channel, ν is the kinematic viscosity and U_b is the bulk velocity defined as

$$U_b := \frac{\iiint_V u(x,y,z)dV}{\iiint_V dxdydz},$$

(V is the volume of the computational domain). Establishing that constant bulk Reynolds number enables fully developed turbulence above the vegetated region.

To discretize the fluid flow, for all the three scenarios an Eulerian grid made up of $N_x \times N_y \times N_z = 1152 \times 384 \times 864$ points has been adopted. While the spacing is homogeneous in both the streamwise x and spanwise z directions, a stretched grid is adopted in the wall-normal direction in order to capture the sharp velocity gradients arising near the canopy tip. Thus, the spacing in the streamwise and spanwise direction is set to $\Delta x/H = 0.0055$ and $\Delta z/H = 0.0055$ respectively, while the wall-normal spacing, starting from a uniform spacing of $\Delta y/H = 0.002$ for $y/h \in [0.0, 0.3]$, gradually increases, reaching $\Delta y/H = 0.004$ at the top wall of the domain, that is $y/H = 1$. This was proven to be compliant with the grid requirements for Direct Numerical Simulation (DNS) of turbulent flows. In fact, the accuracy of turbulence statistics predictions near the wall in DNS of turbulent flows is highly sensitive to the resolution of the computational grid, particularly in the wall-normal direction. To effectively capture the boundary layer behavior, the grid must adequately resolve all three regions of the inner layer: the viscous sub-layer, the buffer layer, and the logarithmic layer. Insufficient grid resolution in one or more directions can lead to errors in both mean flow properties and higher-order turbulence statistics. To ensure grid spacing is independent of the

Reynolds number, it is typically defined in terms of the non-dimensional wall unit, y^+. Standard guidelines for DNS grids in wall-bounded turbulent flows include placing the first grid point below $y^+ = 1$ and ensuring at least 10 grid points are within $y^+ = 10$. These conditions are often achieved by locating the first grid point close to the wall $y^+ = 1$ and increasing the grid spacing away from the wall, often using a geometric progression (Ghiasi et al. 2018).

3.2 Mathematical Methods

The simulations have been performed with OIST's in-house solver *Fujin* (*Fujin Code* 2020). We, therefore, consider the generic mathematical formulation:

$$\begin{cases} \rho\left(\frac{\partial u_i}{\partial t} + \frac{\partial u_i u_j}{\partial x_j}\right) = \frac{\partial \sigma_{ij}}{\partial x_j} + f_i, & \sigma_{ij} = -p\delta_{ij} + \mu\left(\frac{\partial u_i}{\partial x_j} + \frac{\partial u_j}{\partial x_i}\right) \\ \frac{\partial u_i}{\partial x_i} = 0, & \end{cases} \tag{3.2}$$

representing the 3D incompressible Cauchy equation.

3.2.1 Time Advancement

To deal with the incompressibility constraint, a fractional step-method is adopted for the temporal advancement of the numerical solution. Indeed, the primary challenge in achieving a time-accurate solution for incompressible flow stems from the absence of an explicit time-derivative in the continuity equation. Thus, mass conservation is enforced through an implicit coupling between the continuity equation and pressure within the momentum equations, which leads to the Poisson equation (Kim and Moin 1985).

The fractional-step method consists in the following steps (Wendt 2009):

1. **Prediction Step**: assuming a random pressure distribution p^*, a velocity field V^* which does not necessary satisfy the incompressibility constraint, given by the diverge free velocity field $\nabla \cdot V = 0$, is calculated by solving the momentum equation.

2. **Projection Step**: to enforce incompressibility, the intermediate velocity field calculated during the prediction step is projected onto a divergence-free field and the correct pressure field is calculated.

3. **Correction Step**: once the pressure field such that the continuity equation is satisfied is calculate, the final divergence-free velocity field can be calculated

Prediction Step

In order to calculated the predicted velocity field, we consider the momentum equation 3.2:

$$\frac{\partial u_i}{\partial t} = -\frac{\partial u_i u_j}{\partial x_j} + \frac{1}{\rho}\frac{\partial \sigma_{ij}}{\partial x_j} + f_i, \qquad \sigma_{ij} = -p^*\delta_{ij} + \mu\left(\frac{\partial u_i}{\partial x_j} + \frac{\partial u_j}{\partial x_i}\right) \tag{3.3}$$

where p^* is the assumed pressure field which does not necessarily satisfy the continuity equation. A second order Adams-Bashforth scheme for the time stepping is adopted. Considering a generic ODE:

$$y'(t) = f(t, y(t)), \tag{3.4}$$

and integrating it between a generic time interval $[t_{n+1}, t_{n+2}]$, we obtain:

$$y(t_{n+2}) = y(t_{n+1}) + \int_{t_{n+1}}^{t_{n+2}} f(t, y(t))dt, \tag{3.5}$$

However, the integral cannot be computed directly, as it depends from $y(t)$ which is unknown, thus it must be approximated.

The idea behind multi-step methods is based on the fact that the integral can be approximated using polynomials of varying degrees, where the order of the scheme is determined by the degree of the polynomial function. Specifically, if the polynomial used to approximate the integrand is of degree k, the method will be of order $k + 1$. Within the multi-step methods, the Adams method are distinguished into:

- Explicit methods, known as Adams-Bashforth methods;
- Implicit methods, known as Adams-Moulton methods.

Implicit methods are unconditionally stable, but they do not allow for a determination of the intermediate field. Since our objective in the prediction step is to determine the intermediate velocity field, it is essential to refer to the explicit methods. This is also due to the fact that, when considering an IBM method, the fluid-structure interaction is accounted for through an external moment/force exerted by the structure on the surrounding fluid. Because the introduction of the external forcing is taken into account in the uncorrected predicted field, it is immediately clear that the latter must be known.

The second order Adams-Bashforth scheme, in order to evaluate the integral

$$\int_{t_{n+1}}^{t_{n+2}} f(y, t)dt,$$

adopts a linear polynomial interpolation between t_n and t_{n+1} and the value at t_{n+2} is extrapolated. The calculations of the integral have been reported in Appendix A, leading to the numerical method:

$$y_{n+2} = y_{n+1} + \Delta t \left(\frac{3}{2} f(y_{n+1}, t_{n+1}) - \frac{1}{2} f(y_n, t_n) \right). \tag{3.6}$$

Applying the second order Adams-Bashforth scheme to equation 3.3, we can determine the predicted velocity field u_i^*:

$$\frac{u_i^* - u_i^n}{\Delta t} = \frac{3}{2} rhs_i^n - \frac{1}{2} rhs_i^{n-1}, \tag{3.7}$$

with the right hand side:

$$rhs_i = -\frac{\partial u_i u_j}{\partial x_j} + \frac{1}{\rho}\frac{\partial \sigma'_{ij}}{\partial x_j} + \frac{f_i}{\rho},$$

where u_i^n is the velocity field at the n-th time step which respects the continuity equation, while rhs_i^n and rhs_i^{n-1} are the right-hand side of equation 3.3 at the time steps n-th and $(n-1)$-th respectively. Finally:

$$u_i^* = u_i^n + \Delta t \left(\frac{3}{2} rhs_i^n - \frac{1}{2} rhs_i^{n-1} \right).$$

Projection Step

The predicted velocity field $\mathbf{V}^*$ is used to calculate the correct pressure field. This is achieved by solving the numerical Poisson equation, which, in the case of constant density, writes as:

$$\begin{aligned} \frac{\partial^2 p}{\partial x_i \partial x_i} &= \frac{\rho}{\Delta t}\frac{\partial u_i^*}{\partial x_i} \\ &= S_i, \qquad\qquad i = 1,2,3 \end{aligned}$$

where $u_i^*, i = 1,2,3$ are the three components of the predicted velocity field. Since we are dealing with a 3D problem, the left-hand side of the equation, leads to an epta-diagonal matrix:

$$\frac{p_{i-1,j,k} - 2p_{i,j,k} + p_{i+1,j,k}}{\Delta x^2} + \frac{p_{i,j-1,k} - 2p_{i,j,k} + p_{i,j+1,k}}{\Delta y^2} + \frac{p_{i,j,k-1} - 2p_{i,j,k} + p_{i,j,k+1}}{\Delta z^2}.$$

The pressure field can be divided into to contributes:

$$p = p^* + p', \tag{3.8}$$

where p^* is the assumed pressure field considered in the prediction step, p' is the pressure correction and p is the pressure field such that the velocity field respects the incompressibility constraint. Thus, p^* is known and by substituting p' into the Poisson Equation, we can obtain a pressure correction which leads to the desired pressure field. It is worth noting that an analogous approach consists in not considering the pressure field in the projection step, thus considering $p^* = 0$, which leads to $p = p'$.

Different methods can be adopted to solve the Poisson Equation. As highlighted by Dorr 1970, discrete models of the Poisson Equation involve systems of very large dimensions, which cause direct methods like Gaussian elimination not efficient. Other direct methods which take advantage of the block structure of the linear equations, but, when dealing with really large matrices, they become expensive from both a computational and a memory point of view. Tensor products approaches have also taken into consideration, but, given the huge amount of multiplications involved, they are not really efficient. Instead, an efficient way to solve the Poisson equation and simplify the matrix structure involves the computing of Fourier transforms, commonly used in the Fourier series methods. The discrete Fourier transform is computed in the homogeneous directions:

$$\tilde{p}_{i,j,k} = \mathcal{F}_i(p_{i,j,k}),$$

thus obtaining a reduced system which is solved through the Gaussian elimination method. Finally, an inverse discrete Fourier transform allows to return to the physical space.

Correction Step

As the pressure correction is now known, considering once again the momentum equation:

$$\frac{u_i^{n+1} - u_i^*}{\Delta t} = -\frac{1}{\rho}\frac{\partial p'}{\partial x_i},$$

the correct velocity field is calculated

$$u_i^{n+1} = u_i^* - \frac{\Delta t}{\rho}\frac{\partial p'}{\partial x_i},$$

and the incompressibility equation is respected.

The step project method has been summarized in the scheme in figure 3.3.

3.2.2 Space Discretization

A second order central finite difference scheme is used for space discretization of variables. Therefore, the first derivative of a generic variable f with respect to a generic direction x computed in a generic point x_0:

$$\left.\frac{\partial f}{\partial x}\right|_{x_0} \simeq \frac{f(x_0+h)-f(x_0-h)}{2h},$$

while the second derivative:

$$\left.\frac{\partial^2 f}{\partial x^2}\right|_{x_0} \simeq \frac{f(x_0+h)-2f(x_0)+f(x_0-h)}{h^2}.$$

Additionally, a staggered grid arrangement is used, where velocity components are defined at the cell faces, while other variables, including pressure, are located at the cell centers. Linear interpolation is applied to facilitate data transfer between the faces and centers.

3.2.3 Filament Dynamics and Lagrangian-IBM

When considering flexible filaments, we no longer deal with a pure fluid-dynamics problem, since there is a strong coupling between the filament and the fluid dynamics (Py, E. D. Langre, et al. 2006). Thus, the fluid-structure interaction is addressed to with a Lagrangian Immersed Boundary Layer Method.

As previously mentioned, each flexible filament is modeled as a line of $n_L = 32$ Lagrangian points. This choice is not random: as highlighted by Rota et al. 2024, as flexible filaments tend to follow the flow, their velocity is closer to that of the fluid if compared to rigid filaments, resulting in too strict implications on the time step if a higher number of Lagrangian filaments was adopted.

The dynamics of the filaments is modeled using the approach proposed by Banaei et al. 2020, which is an extended version of the Distributed-Lagrangian-Multiplier/Fictitious-Domain (DLM/FD, Yu 2005) formulation. The flexible filaments are described with the generalized Euler-Bernoulli beam model coupled

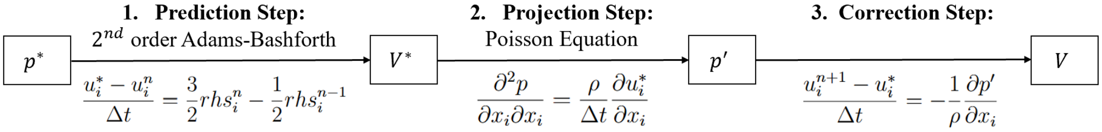

Figure 3.3: Scheme of the Step Projection Method

with the inextensibility constraint (Yu 2005, Huang et al. 2007, Banaei et al. 2020). Given $X(s,t)$ the position of a Lagrangian point in the filament as a function of the curvilinear abscissa s and of time t:

$$\begin{cases} \Delta\tilde{\rho}\frac{\partial^2 \mathbf{X}}{\partial t^2} = \frac{\partial}{\partial s}\left(T\frac{\partial \mathbf{X}}{\partial s}\right) - \gamma\frac{\partial^4 \mathbf{X}}{\partial s^4} - \mathbf{F}, \\ \frac{\partial \mathbf{X}}{\partial s}\cdot\frac{\partial \mathbf{X}}{\partial s} = 1, \end{cases} \tag{3.9}$$

where T is the tension force along the filament axis, γ the bending rigidity, F the forced exerted by the fluid on the filament and $\Delta\tilde{\rho} = (\rho_s - \rho_f)\pi d^2/4$ the density difference between the filaments and the surrounding fluid.
The system of equation 3.9 is then closed enforcing boundary conditions. In fact, the filaments are clamped on the bottom wall ($s = 0$), while their extreme ($s = h$) is free to oscillate, thus:

$$\begin{cases} \mathbf{X}|_{s=0} = \mathbf{X}_0 & s = 0 \\ \frac{\partial \mathbf{X}}{\partial s}|_{s=0} = (0,1,0) & s = 0 \\ \frac{\partial^2 \mathbf{X}}{\partial s^2}|_{s=h} = \frac{\partial^3 \mathbf{X}}{\partial s^3}|_{s=h} = 0 & s = h \\ \mathbf{T}|_{s=h} = 0 & s = h \end{cases} \tag{3.10}$$

Equation 3.9 along with the boundary conditions is solved following the approach outlined by Huang et al. 2007. Thus, the fluid motion, defined on an Eulerian grid, and the filament motion, defined on a Lagrangian grid, are independently solved, while the fluid-structure interaction is accounted through a feedback law. At every time step the fluid velocity $\mathbf{u}$ is calculated and then interpolated at the structure points. We call $\mathbf{u_L}$ the fluid velocity interpolated on a specific Lagrangian point of the structure and $\mathbf{u_{IBM}}$ the velocity of the filament at the same Lagrangian point. The transformation of the velocity between the fluid-Eulerian grid and the filament-Lagrangian grid is realized through the Dirac delta function:

$$\mathbf{u_L}(s,t) = \int_\Omega \mathbf{u}(\mathbf{x},t)\delta(\mathbf{X}(s,t) - \mathbf{x})d\mathbf{x}.$$

The Lagrangian force exerted by the fluid on the filaments is a linear function of the difference between these two velocities:

$$\mathbf{F} = \beta(\mathbf{u_{IBM}} - \mathbf{u_L}),$$

where β is a properly defined coefficient. Finally, the Lagrangian force is projected on the Eulerian grid to compute the back-reaction of the filaments on the nearby fluid:

$$\mathbf{f}(\mathbf{x},t) = \rho\int_\Gamma \mathbf{F}(s,t)\delta(x - \mathbf{X}(s,t))ds.$$

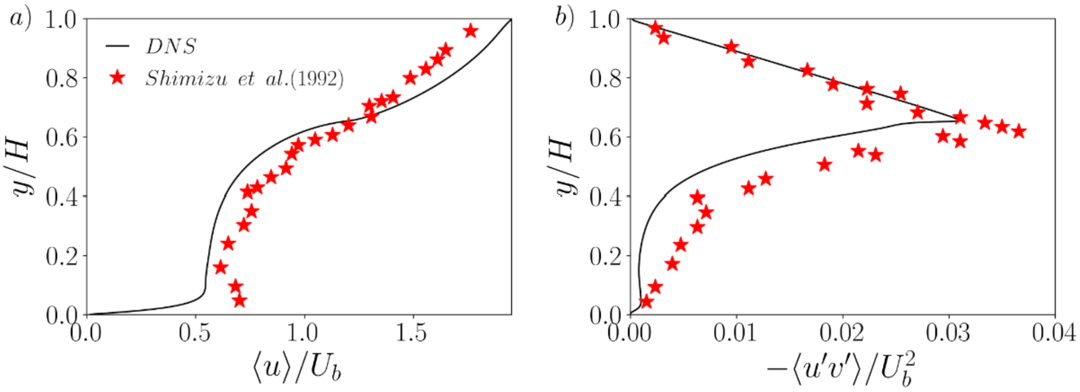

Figure 3.4: Comparison of the mean streamwise velocity profile and Reynolds shear stress between experimental data by Shimizu et al. 1991 and numerical data computed with the code. Rota et al. 2024.

3.3 Code Validation

The accuracy of a code is typically assessed by comparing its predictions to real-world observations, indicating how well the mathematical model represents actual conditions or behaviors. Thus, the importance of validation when dealing with computational models (Borg et al. 2014).

3.3.1 Fluid

A comparison between simulation results and experimental data, as presented by Rota et al. 2024 and Monti, Olivieri, et al. 2023, is shown in figure 3.4. Both the mean streamwise velocity profile and the Reynolds shear stress obtained from the simulations are compared to the experimental measurements of Shimizu et al. 1991, which investigated turbulent flow at $Re_b = 7070$ over a rigid canopy with a height of $h = 0.65H$. The agreement between the simulation and experimental results demonstrates that the code accurately captures the fluid dynamics of the studied phenomena.

3.3.2 IBM

The validation of the Lagrangian-IBM, available at *Fujin Code* 2020, has been conducted basing on either the results obtained by Huang et al. 2007 or theoretical results. A filament of length c and flexibility γ, with a density difference $\Delta\tilde{\rho}$ between the filament and the fluid, is considered. Initially held stationary with an

	S1	S2	S3
c	$1\,m$	$1\,m$	$1\,m$
n_L	100	100	65
$\Delta\tilde{\rho}$	$1\,kg/m$	$1\,kg/m$	$1.5\,kg/m$
γ	$0.01\,kgm^3/s^2$	$0.01\,kgm^3/s^2$	$0.0015\,kgm^3/s^2$
g	$10\,m/s^2$	-	$0.5\,m/s^2$
ν	-	-	$0.005\,m^2/s$

Table 3.1: Parameters used in the three considered scenarios for validating the IBM code: a hanging filament under gravity (S1), a unsupported and cantilevered fiber with no loads applied (S2) and a hanging filament in a uniform form with velocity V (S3).

angle of 0.1π from the vertical direction, after being released, the filament starts oscillating. It is discretised with a total of h_L Lagrangian points. Three different scenarios, whose sketches are shown in 3.5 have been simulated:

1. A hanging filament under gravity, where the driving force is the gravity force;
2. A unsupported and cantilevered fiber under no loads, thus subjected to free vibrations;
3. An hanging filament in a uniform flow with velocity V, where the driving force is a combined effect of the viscous fluid flow ν and gravity force g

The values of the parameters for the three analyzed scenarios have been reported in table 3.1.

Graphs in figure 3.6 compare the values computed by the code with either data obtained by Huang et al. 2007 or theoretical formulations.

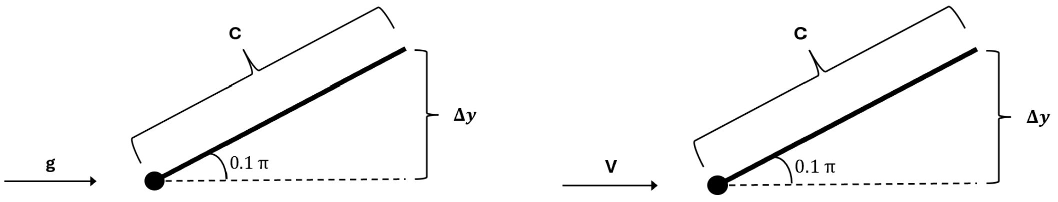

(a) Hanging filament under gravity **(b)** Hanging filament in uniform flow

Figure 3.5: Sketch of the problems considered for IBM validation: a hanging filament sujected to gravity force (a) and a hanging filament in a uniform flow (b)

For the filament oscillating under the gravity force (figure 3.6a) and for the hanging filament in a uniform flow (3.6c), the time evolution of the y-coordinate of the free-end of the filament has been reported. Results obtained by Huang et al. 2007 are shown as red dots, while the numerical results obtained by the code are reported as blue lines. On the other hand, for the filament performing free oscillations 3.6b, the frequency of the free oscillations computed (red dots) is plot against the analytical solution (blue lines), described by:

$$\begin{cases} f = \frac{22.3733}{2\pi c^2}\sqrt{\frac{\gamma}{\Delta\tilde{\rho}}} & \text{Free fiber} \\ f = \frac{3.5161}{2\pi c^2}\sqrt{\frac{\gamma}{\Delta\tilde{\rho}}} & \text{Clamped fiber} \end{cases}$$

The graphs confirm the ability of the code of addressing the dynamics of the filaments, as evidenced by the correspondence between the code's calculated data and the comparative data.

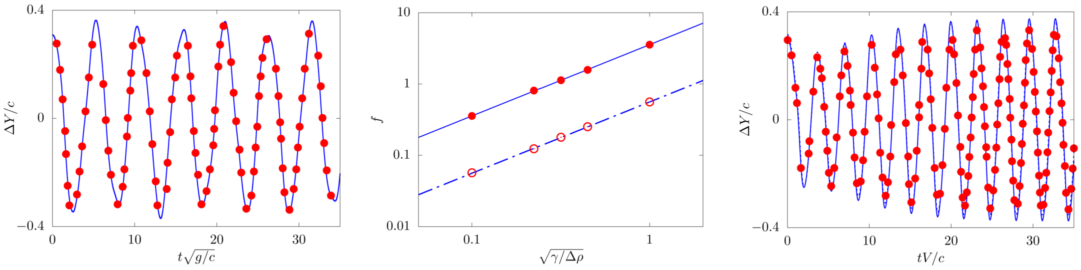

(a) S1 **(b)** S2 **(c)** S3

Figure 3.6: Filament code validation, *Fujin Code* 2020. Time evolution of the y-coordinate of the free end of the filament is shown for the cases of the filament oscillating under gravity (Panel (a)) and the hanging filament in a uniform flow (Panel (c)). Red dots represent results from Huang et al. (2007), while blue lines indicate the numerical results from the current code. For the case of the filament performing free oscillations (Panel(b)), the computed frequency of oscillations (red dots) is plotted against the analytical solution (blue lines)

3.4 Convergence of the Simulations

Channel flows require external forcing to counterbalance the viscous forces that arise, which is typically achieved by either specifying a constant flow rate or a fixed pressure gradient Hasegawa et al. 2014. In our simulations, we employed the latter approach, thus, to verify the convergence of the simulations, we examined the stabilization of the pressure gradient toward a constant value. Since in channel flows pressure is a function of only the streamwise direction and is independent of the other two spatial directions (Pope 2000), the pressure gradient writes as

$$\frac{\partial p}{\partial x} = \frac{dp}{dx},$$

as in figure 3.7. For both the canopy patch simulations ($Ca = 10$ in panel 3.7a and $Ca = 100$ in panel 3.7b), after eliminating the initial transitory, the pressure gradient stabilizes, oscillating within an amplitude range of 0.003.

To further verify convergence, we looked at the shape of the streamwise velocity profiles (Figure 3.8). The velocity profiles in both the vegetated (panels 3.8a and 3.8c) and non-vegetated regions (panels 3.8b and 3.8d) were compared between the final iteration (blue profiles) and the profiles at three-quarters of the total iterations (red profiles), ensuring that significant changes do not occur in the profile shape as the simulation progresses, which would indicate non-convergence.

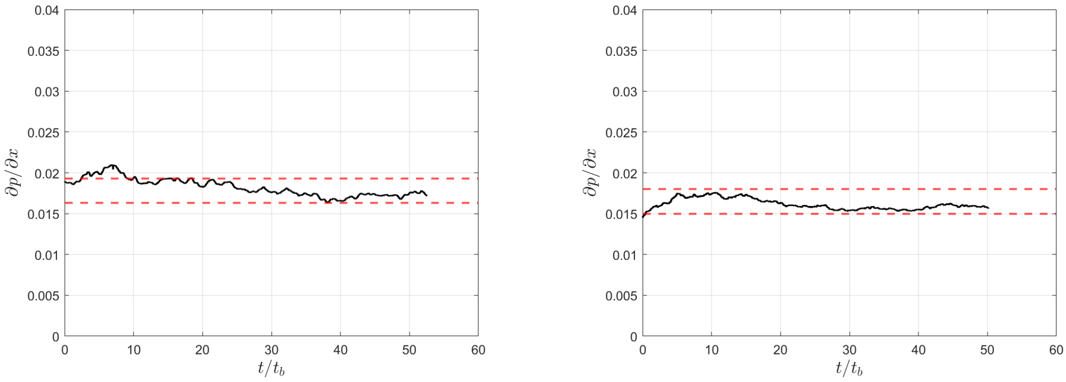

(a) $Ca = 10$

(b) $Ca = 100$

Figure 3.7: Numerical convergence of the simulations for $Ca = 10$ (a) and $Ca = 100$ (b). For both simulations, the value of the pressure gradient oscillates in a range of values of amplitude 0.003, thus the simulations can be considered to have reached convergence.

The limited fluctuation of the pressure gradients and the velocity profiles indicate that the simulations have reached convergence.

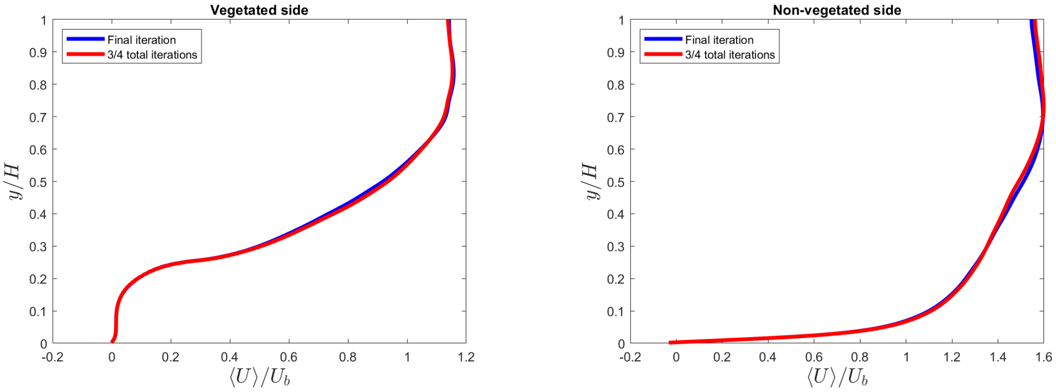

(a) Vegetated side, $Ca = 10$ **(b)** Non vegetated side, $Ca = 10$

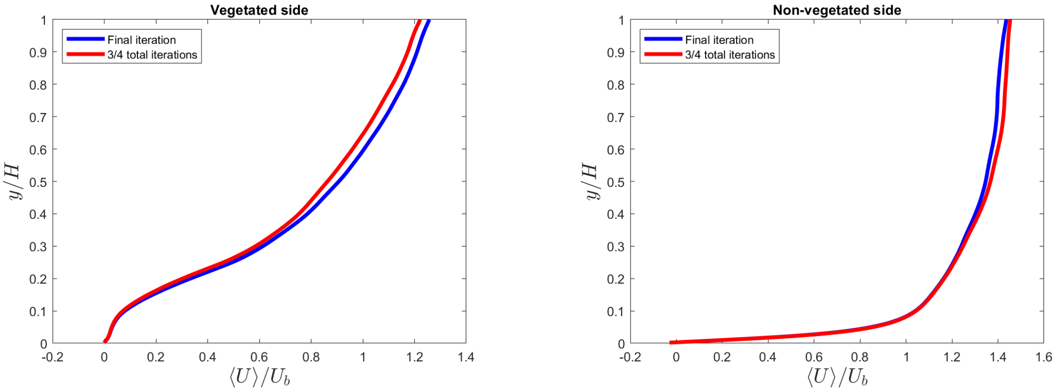

(c) Vegetated side, $Ca = 100$ **(d)** Non vegetated side, $Ca = 100$

Figure 3.8: Numerical convergence of the simulations for $Ca = 10$ (panels (a) and (b)) and $Ca = 100$ (panels (c) and (d)). The velocity profiles in both the vegetated (panels (a) and (c)) and non-vegetated regions (panels (b) and (d)) were compared between the final iteration and the profiles at three-quarters of the total iterations.

Chapter 4

Results

Since the goal of the thesis is to study the behavior of both the fluid and the filaments, the results have been divided into two parts. Section 4.1 focuses on fluid dynamics, starting with the mean flow and velocity profiles 4.1.1, followed by an analysis of fluctuations. This includes examining how they balance the forcing term in the shear equation on average 4.1.2, then investigating instantaneous events 4.1.3 and correlations 4.1.4. Once the behavior of the fluid is known, section 4.2 focuses on filament dynamics by examining the mean position of canopy tips 4.2.1, the average deflection of filaments 4.2.2 and the spectral analysis of the velocity of the tips to better understand how the filaments oscillate 4.2.3.

Knowing that the domain is divided into two regions and considering for convenience the system as a natural canopy, in the following we will address the regions covered by filaments as the vegetated side, while the region without filaments as the non-vegetated side.

4.1 Fluid Dynamics

4.1.1 Mean Flow and Velocity Profiles

To gain deeper insight into the fluid's behavior as it flows above and through a canopy region, it is essential to first examine the mean fluid field and analyze the different velocity components. Quantities denoted with angle brackets $\langle \cdot \rangle$ are averaged both in time and along the homogeneous directions. For the fully distributed canopy and open channel scenarios, this averaging is performed over both the streamwise and spanwise directions. In contrast, for the canopy patch scenario, averaging is carried out only in the streamwise direction. Consequently, while velocity profiles in the fully distributed canopy and open channel scenarios depend solely on the wall-normal coordinate, in the canopy patch scenario, they

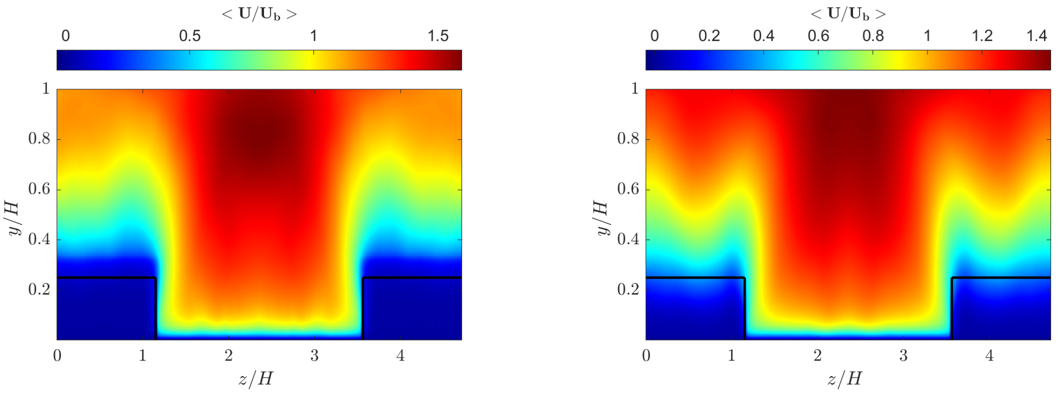

(a) $Ca = 10$ **(b)** $Ca = 100$

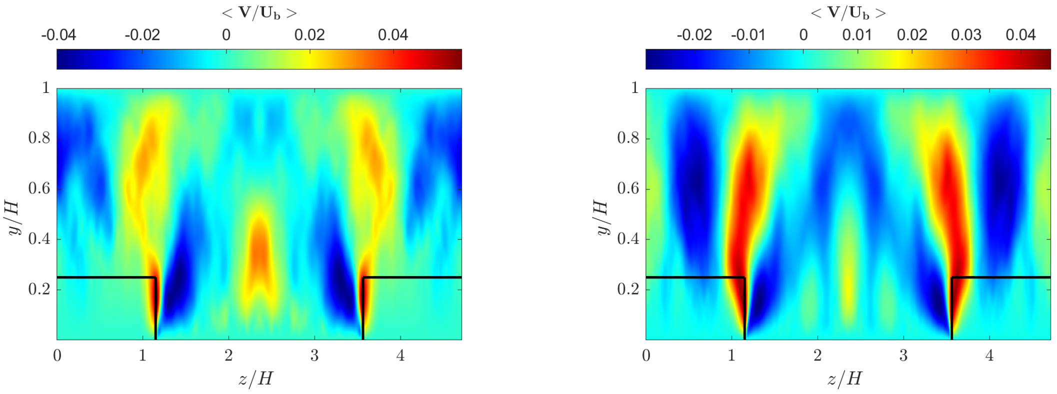

(c) $Ca = 10$ **(d)** $Ca = 100$

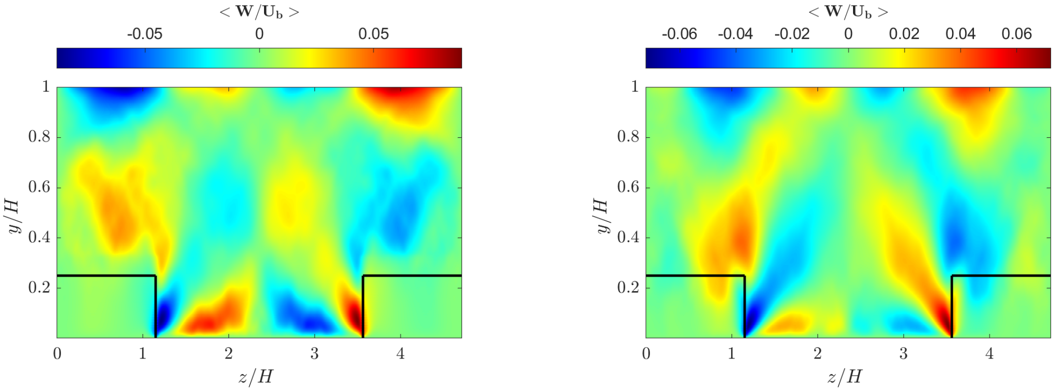

(e) $Ca = 10$ **(f)** $Ca = 100$

Figure 4.1: Streamwise, Wall-normal and Spanwise velocity fields averaged in time and in the streamwise direction for $Ca = 10$ (a) and $Ca = 100$ (b). The black lines represent the extent of the canopy region when the filaments are at rest without deflection.

vary with both the wall-normal and spanwise coordinates.

Focusing on the canopy patch scenario, Figure 4.1 illustrates the distribution of the velocity components, each normalized by the global bulk velocity U_b, for the two Cauchy numbers, $Ca = 10$ and $Ca = 100$. It is worth remembering that the z/H represents the spanwise direction, while y/H is the wall-normal direction, both normalized basing on the height of the channel H.

Several key features can be observed. Starting with the streamwise velocity component $\langle u \rangle / U_b$, the highest velocity values are found in the upper region, where no vegetation is present, and the fluid flow is less affected by the canopy. Conversely, within the canopy itself, the velocity decreases towards zero, as highlighted by Bennett et al. 2002, indicating that the filaments act as a barrier to the flow. The presence of the canopy is noticeable even above the filaments, with the undeflected height of the filaments marked by the black horizontal line. The black vertical lines indicate the boundary between the vegetated and non-vegetated regions. In the rigid scenario $Ca = 10$, the shielding effect is evident even above the canopy, where the velocity gradually increases outward from the canopy. This contrasts with the more flexible scenario $Ca = 100$ where the velocity increases more slowly. This difference may be attributed to the greater deflection of the filaments in the flexible scenario, which results in a different perturbation of the flow just above the canopy.
As for the wall-normal $\langle v \rangle / U_b$ and spanwise $\langle w \rangle / U_b$ velocity components, the mean

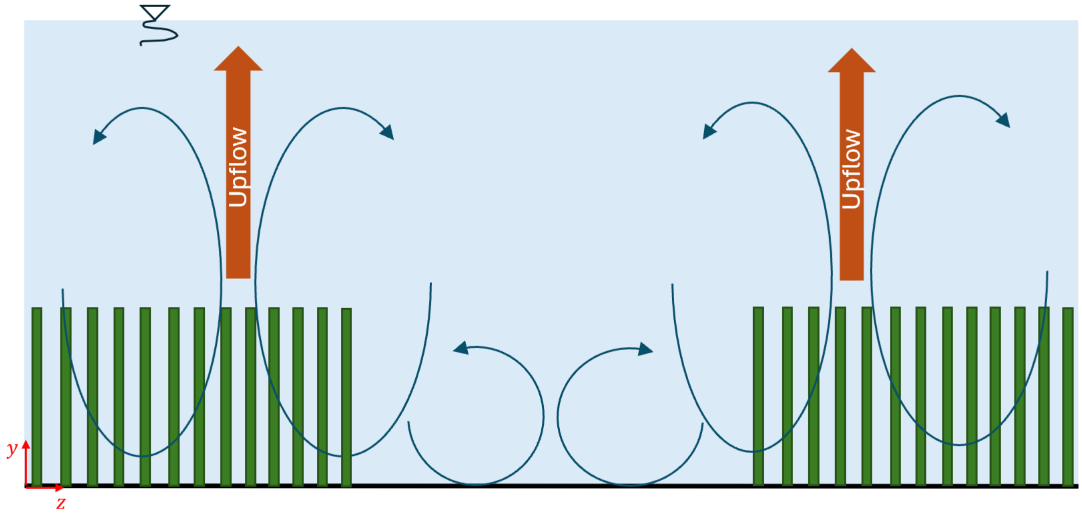

Figure 4.2: Illustration of the secondary circulation and the associated upflow generated by it.

behavior of the flow suggests the emergence of vortex structures in the domain, similar to the secondary circulations highlighted by Unigarro Villota et al. 2023. The trends of the span-wise and wall-normal velocities are consistent with this result. These vortexes induce an updraft of low-energy flow above the canopy.

Having established the behavior of the mean flow in the canopy patch scenario, it is now important to compare it with the fully-distributed canopy and open channel scenarios. This comparison will help determine whether the problem can be simplified into two two-dimensional problems, one where the flow above the vegetated region is treated as a fully-distributed submerged canopy, and the other where the flow in the main non-vegetated channel is modeled as an open channel. To achieve this, the vertical velocity profiles must be analyzed.

It is important to note that, unlike the fully-distributed canopy scenario, where the filaments cover the entire bottom wall of the domain, in the canopy patch scenario, only half of the bottom wall is covered by vegetation. Therefore, it is of interest to investigate whether the canopy patch scenario behaves as an intermediate case between the two other scenarios under consideration. The averaging is performed over both time and the homogeneous directions. In the canopy patch scenario, there is only one homogeneous direction - the streamwise direction - whereas in the

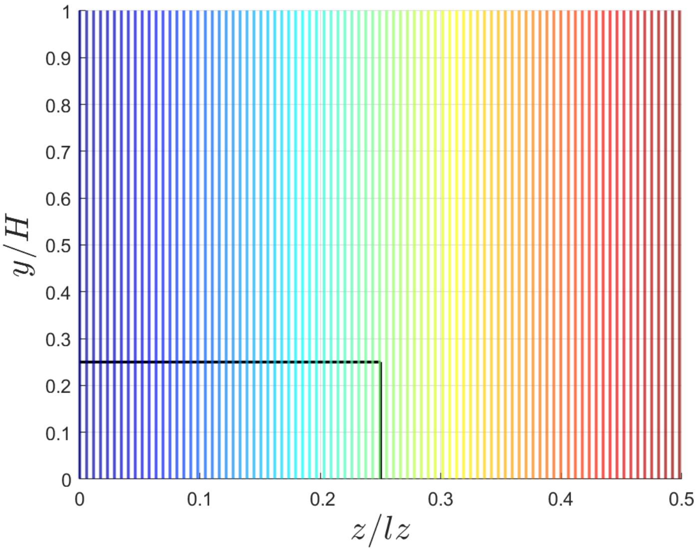

Figure 4.3: Spanwise locations at which the velocity profiles have been computed. The blue profiles are located deep inside the canopy, while the red ones are positioned towards the center of the non-vegetated region. Black lines represent the extent of the non-deflected filaments.

fully-distributed canopy and open channel scenarios, there are two homogeneous directions, the streamwise and the spanwise. To account for this, several spanwise coordinates in the canopy patch scenario have been considered, as shown in Figure 4.3. For each of these spanwise coordinates, the profiles of the different velocity components have been plotted. The profiles colored in blue represent locations deep within the canopy, closer to where the periodic condition is imposed, while those in red are positioned towards the center of the non-vegetated area. The black lines indicate the extent of the undeflected filaments and are included to clarify the locations where the profiles have been computed. Only half of the domain is considered, as the domain is symmetric in the spanwise direction, meaning that the results are identical for the other half.

Figure 4.4 depicts the streamwise vertical velocity profiles at the different spanwise coordinates considered, for the two different Cauchy number $Ca = 10$ in panel 4.4a and $Ca = 100$ in panel 4.4b. The streamwise velocity is normalized on the global bulk velocity U_b. The dashed profile is the one at the boundary between the vegetated and non-vegetated regions, while the dashed horizontal line represents the canopy tip position when not deflected. The figure highlights the presence of inflection points, indicated by black dots, in some but not all of the velocity profiles for both filament flexibilities. According to Rayleigh's theorem, the existence of an

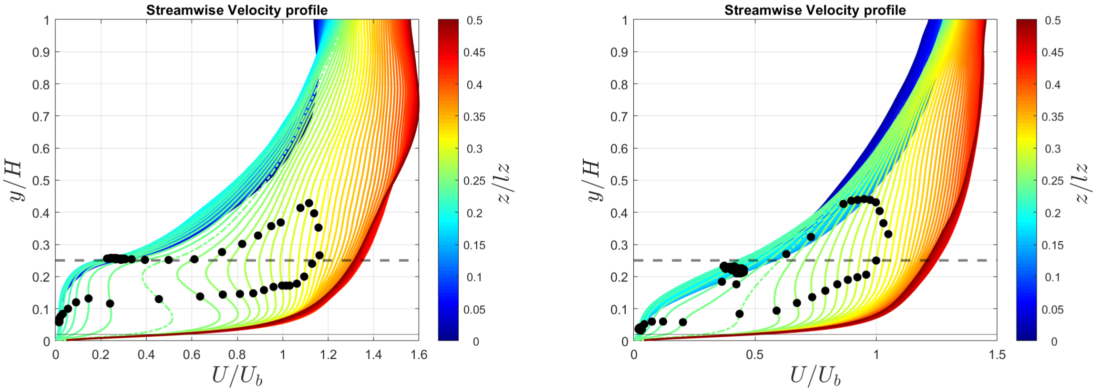

(a) $Ca = 10$ **(b)** $Ca = 100$

Figure 4.4: Streamwise velocity profiles computed at different locations in the spanwise direction for $Ca = 10$ and $Ca = 100$. The blue profiles are located deep inside the canopy, while the red ones are positioned towards the center of the non-vegetated region. The dashed profile is located at the boundary between the vegetated and non-vegetated side. Black dots represent inflection points of the velocity profiles. The horizontal dashed line represent the position of the canopy tips when not deflected.

inflection point in the velocity profile is a necessary condition for flow instability, making the flow more susceptible to shear instabilities, such as the Kelvin-Helmholtz instability. Starting with the profiles inside the vegetated region (colored blue) and moving towards the center of the domain, two inflection points are identified. These points then merge into a single inflection point and, since the last velocity profile within the canopy is the dashed one, this merging occurs in the non-vegetated region for both Cauchy numbers. This suggests that the canopy may induce flow instability - and potentially vortex formation - even outside the vegetated area. The outer inflection point is located near the canopy tip, while the inner inflection point is within the canopy and closer to the bottom wall. This observation aligns with the findings of Rota et al. 2024, who identified an outer inflection point due to the drag discontinuity above the canopy, and an inner inflection point that merges the velocity profile with the no-slip condition imposed at the bottom wall. As we move deeper into the canopy from the non-vegetated region, the outer inflection points stabilize at a height corresponding to the tip of the filaments, whereas the inner inflection points do not stabilize. This suggests that as we approach the periodicity condition in the spanwise direction, the flow tends to a configuration that can be modeled as a fully-distributed canopy. For a higher flexibility, the outer inflection point moves below the canopy top.

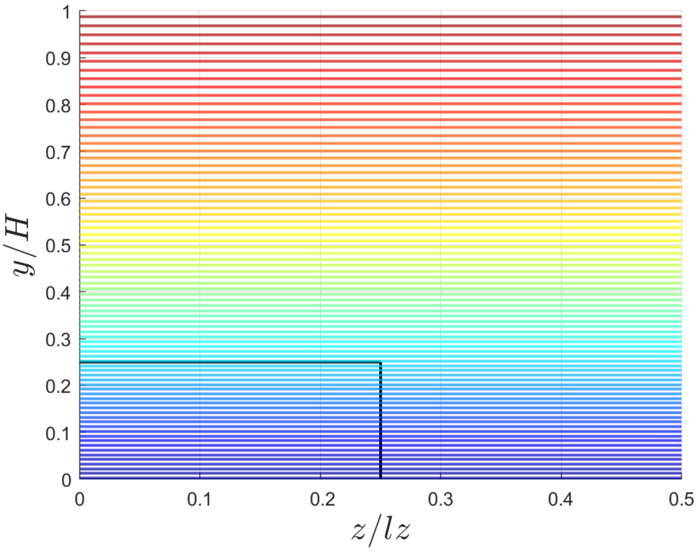

Figure 4.5: Wall-normal locations at which the velocity profiles have been computed. The blue profiles are located close to the bottom wall of the domain, while the red ones are positioned towards the top wall of the domain. Black lines represent the extent of the non-deflected filaments.

In order to evaluate the effect of the lateral interface, figure 4.6 shows at fixed locations in the wall-normal direction, the dependence of the average streamwise velocity, normalized on the global bulk velocity U_b, on the spanwise direction, for the two different Cauchy numbers $Ca = 10$ (panel 4.6a) and $Ca = 100$ (panel 4.6b). Thus, profiles colored in blue are located closer to the bottom wall of the domain, while the red ones are close to the top wall, as shown in figure 4.5. In both cases, the dashed profile is the one located at the average position of the deflected canopy tips, thus separating the vegetated region to the above flow. The analyzed velocity profiles reveal the presence of inflection points, indicating the potential formation of coherent structures at the lateral interface, similarly to what occurs in partially obstructed channels with emergent vegetation. This is due to the inhomogeneity in the spanwise direction, which creates an abrupt change in velocity between the vegetated and the non-vegetated sides.

To compare the canopy patch scenario with the fully-distributed canopy and open channel scenarios, it is essential to examine the vertical profiles of the streamwise velocity. In fact, in the two limiting scenarios, the spanwise direction is homogeneous, meaning that the velocity does not vary in the transverse direction and the velocity profiles in figure 4.6 cannot be considered.To enable a meaningful comparison, the velocity profiles shown in figure 4.4 must be normalized to ensure a unit area under each profile. For this purpose, a new quantity is introduced, the local bulk velocity,

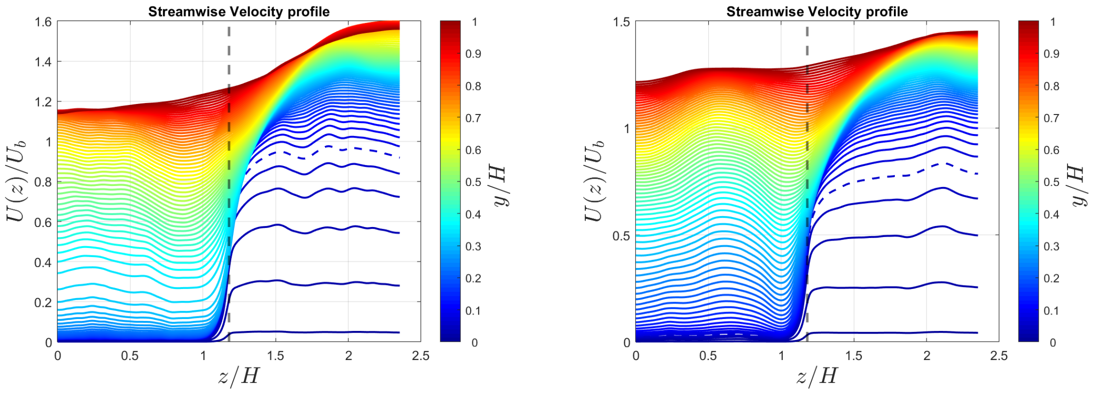

(a) $Ca = 10$ **(b)** $Ca = 100$

Figure 4.6: Streamwise velocity profiles as a function of the spanwise direction $U(z)/U_b$ computed at different locations in the wall-normal direction for $Ca = 10$ and $Ca = 100$. The blue profiles are located closer to the bottom wall of the domain, while the red ones are positioned towards the top wall of the domain. The dashed vertical line is located at the boundary between the vegetated and non-vegetated side.

$U_b(z)$, that is the bulk velocity calculated at fixed spanwise coordinates $\overline{z}$. It may be defined considering the general definition of bulk velocity:

$$U_b := \frac{\iint_A \langle u(y,z) \rangle dydz}{\iint_A dydz}, \tag{4.1}$$

taking into account that y and z are the coordinates in the wall-normal and spanwise direction respectively, u is the velocity component in the streamwise direction, while the symbol $\langle \cdot \rangle$ represents the averaging in time and in the homogeneous direction. Given a fixed position in the spanwise direction $\overline{z}$, the local bulk velocity $U_b(\overline{z})$:

$$U_b(\overline{z}) = \frac{\int_0^H \langle u(y,\overline{z}) \rangle dy}{\int_0^H dy}, \tag{4.2}$$

where H is the height of the channel. This normalization allows to obtain the velocity profiles in 4.7. The colored lines represent the canopy patch scenario, with velocity profiles computed at the same spanwise coordinates as in the previous figure. The blue profiles were computed deep within the canopy, close to the periodic condition, while the red ones are located near the center of the non-vegetated region. For the other two scenarios, only one velocity profile is shown, as the averaging

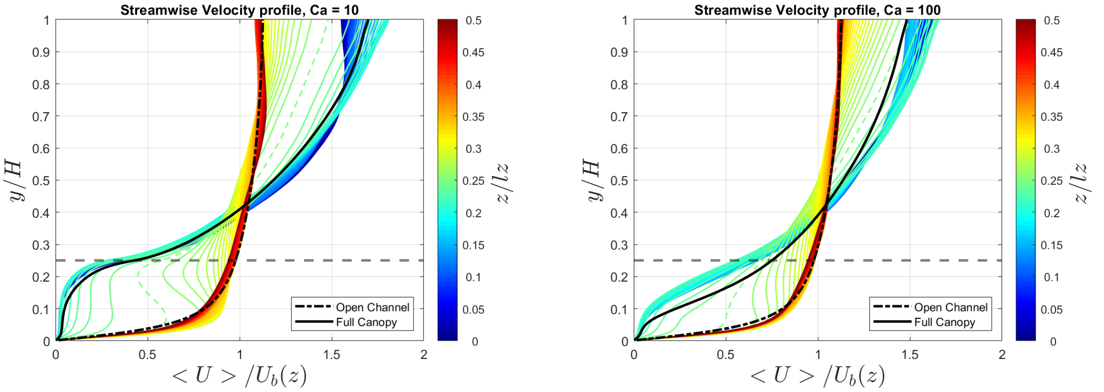

(a) $Ca = 10$ **(b)** $Ca = 100$

Figure 4.7: Velocity profiles of the streamwise velocity component at different positions in the spanwise direction. The streamwise velocity component is averaged in time and in the homogeneous direction and has been normalized with the local U_b in order to compare it to the velocity profiles of the open channel (solid black line) and of the fully-distributed canopy (dash-dotted black line). The dashed profile is located at the boundary between the vegetated and non-vegetated regions. The horizontal dashed line represent the position of the canopy tips when not deflected.

is done over time and in both homogeneous directions. Thus, the solid black line represents the average velocity profile for the fully-distributed canopy scenario, and the dashed-dot black line corresponds to the open channel scenario. Finally, the horizontal dashed line represents the tip of the filaments in their undeflected state.

As the velocity profiles in the canopy patch scenario falls between the two limiting cases of the open channel and fully-distributed canopy, the canopy patch scenario represents as an intermediate case between the other two. In fact, as the analysis moves deeper into the vegetated region, the velocity profiles tend to align more closely with those of the fully-distributed canopy. On the other hand, in the non-vegetated region, the velocity profiles increasingly resemble those of the open channel scenario. This behavior is particularly pronounced in the more rigid case $Ca = 10$, where the velocity profiles within the canopy approach the fully-distributed canopy condition more distinctly. In contrast, in the more flexible case, $Ca = 100$, the velocity profiles within the canopy do not fully converge to the fully-distributed canopy scenario. This discrepancy is likely attributable to the increased deflection and movement of the filaments in the flexible configuration, which alters the flow dynamics within the canopy.

4.1.2 Shear Equation

Once the dynamics of the mean flow has been studied, we focus on understanding the behavior of the velocity fluctuations by subtracting the mean flow to the instantaneous flow field. To do so, we can start by having a look at their role on average in counterbalancing the forcing term, that is the pressure gradient. To do so, this section focuses on deriving and analyzing the shear equation, highlighting the role of the different terms and that of the fluctuations over time.

Taking into account the momentum equation in the streamwise direction

$$\frac{\partial u}{\partial t} + u\frac{\partial u}{\partial x} + v\frac{\partial u}{\partial y} + w\frac{\partial u}{\partial z} = -\frac{\partial p}{\partial x} + \frac{1}{Re}\left(\frac{\partial^2 u}{\partial x^2} + \frac{\partial^2 u}{\partial y^2} + \frac{\partial^2}{\partial z^2}\right) - D, \tag{4.3}$$

where D is the drag exerted by the filaments, first the Reynolds decomposition is introduced:

$$u = \langle U\rangle + u', \qquad v = \langle V\rangle + v', \qquad W = \langle W\rangle + w', \qquad P = \langle P\rangle + p', \tag{4.4}$$

where $\langle(\cdot)\rangle$ is a double average in time and in space, while $(\cdot)'$ refers to the fluctuation terms. Since we want to find an expression that is valid in all three analyzed scenarios—canopy patch, fully-distributed canopy, and open channel—the average in space is performed only in the streamwise direction, which is a common homogeneous direction. Therefore, the expression will contain some terms that are zero for the fully-distributed canopy and open channel, where the spanwise direction is also homogeneous.

By introducing the Reynolds decomposition into the momentum equation 4.3 and averaging both in time and in the homogeneous direction, some terms can be simplified, yielding the following expression:

$$\begin{aligned}\langle u\rangle\frac{\partial\langle u\rangle}{\partial x}+\langle u'\frac{\partial u'}{\partial x}\rangle+\langle v\rangle\frac{\partial\langle u\rangle}{\partial y}+\langle v'\frac{\partial u'}{\partial y}\rangle+\langle w\rangle\frac{\partial\langle u\rangle}{\partial z}+\langle w'\frac{\partial u'}{\partial z}\rangle=\\ =-\frac{\partial\langle p\rangle}{\partial x}+\frac{1}{Re}\left[\frac{\partial^2\langle u\rangle}{\partial y^2}+\frac{\partial^2\langle u\rangle}{\partial z^2}\right]-\langle D\rangle.\end{aligned}$$

By reordering the terms:

$$\begin{aligned}\frac{1}{Re}\left(\frac{\partial^2\langle u\rangle}{\partial y^2}+\frac{\partial^2\langle u\rangle}{\partial z^2}\right)=\frac{\partial\langle p\rangle}{\partial x}+\langle u\rangle\frac{\partial\langle u\rangle}{\partial x}+\langle u'\frac{\partial u'}{\partial x}\rangle+\langle v\rangle\frac{\partial\langle u\rangle}{\partial y}+\\ +\langle v'\frac{\partial u'}{\partial y}\rangle+\langle w\rangle\frac{\partial\langle u\rangle}{\partial z}+\langle w'\frac{\partial u'}{\partial z}\rangle+\langle D\rangle,\end{aligned}\tag{4.5}$$

which is the average momentum balance. It is important to note that the Reynolds number is based on the global bulk velocity U_b:

$$Re=\frac{\mu}{\rho U_b H},\tag{4.6}$$

where μ is the fluid viscosity, ρ the density and H the height of the channel. By integrating expression 4.5 between the bottom wall ($y=0$) and a generic coordinate in the wall-normal direction y, and explicitly expressing the Reynolds number, it is possible to derive an expression for the wall shear stress:

$$\begin{aligned}-\frac{\tau_w}{\rho U_b H}=-\frac{\mu}{\rho U_b H}\frac{\partial\langle u\rangle}{\partial y}\bigg|_y-\frac{\mu}{\rho U_b H}\int_0^y\frac{\partial^2\langle u\rangle}{\partial z^2}dy+\frac{\partial\langle p\rangle}{\partial x}\cdot y+\int_0^y\langle u'\frac{\partial u'}{\partial x}\rangle dy+\\ +\int_0^y\langle v\rangle\frac{\partial\langle u\rangle}{\partial y}dy+\int_0^y\langle v'\frac{\partial u'}{\partial y}\rangle dy+\int_o^y\langle w\rangle\frac{\partial\langle u\rangle}{\partial z}dy+\int_0^y\langle w'\frac{\partial u'}{\partial z}\rangle dy+\int_0^y\langle D\rangle dy,\end{aligned}\tag{4.7}$$

where the wall shear stress term arises from the following integration:

$$\frac{\mu}{\rho U_b H}\int_0^y\frac{\partial^2\langle u\rangle}{\partial y^2}dy=\frac{\mu}{\rho U_b H}\frac{\partial\langle u\rangle}{\partial y}\bigg|_y-\frac{\mu}{\rho U_b H}\frac{\partial\langle u\rangle}{\partial y}\bigg|_0=\frac{\mu}{\rho U_b H}\frac{\partial\langle u\rangle}{\partial y}\bigg|_y-\frac{\tau_w}{\rho U_b H}.$$

It is worth noting that, in the most general scenario where there is only one direction of homogeneity, all the quantities in brackets $\langle\cdot\rangle$ are functions of both the spanwise and wall-normal directions.

By integrating again equation 4.5 but between the bottom wall ($y = 0$) and the top wall of the domain ($y = H$):

$$\cancelto{0}{\frac{\mu}{\rho U_b H} \cdot \left.\frac{\partial \langle u \rangle}{\partial y}\right|_{y=H}} - \frac{\tau_w}{\rho U_b H} + \frac{\mu}{\rho U_b H} \int_0^H \frac{\partial^2 \langle u \rangle}{\partial z^2} dy = \frac{\partial \langle p \rangle}{\partial x} \cdot H + \int_0^H \langle u' \frac{\partial u'}{\partial x} \rangle dy +$$
$$+ \int_0^H \langle v \rangle \frac{\partial \langle u \rangle}{\partial y} dy + \int_0^H \langle v' \frac{\partial u'}{\partial y} \rangle dy + \int_0^H \langle w \rangle \frac{\partial \langle u \rangle}{\partial z} dy + \int_0^H \langle w' \frac{\partial u'}{\partial z} \rangle dy + \int_0^H \langle D \rangle dy, \tag{4.8}$$

where the term $\frac{\mu}{\rho U_b H} \cdot \left.\frac{\partial \langle u \rangle}{\partial y}\right|_{y=H}$ simplifies, as a free-shear condition is enforced at the top wall of the domain.

By substituting the expression for the wall-shear stress from 4.7 into equation 4.8, and rearranging all terms, we finally obtain the final form of the shear equation:

$$\left| \frac{\partial p}{\partial x} \right| \left(1 - \frac{y}{H} \right) \cdot H = \int_y^H \langle D \rangle dy + \frac{\mu}{\rho U_b H} \left. \frac{\partial \langle u \rangle}{\partial y} \right|_y - \frac{\mu}{\rho U_b H} \int_y^H \frac{\partial^2 \langle u \rangle}{\partial z^2} dy +$$
$$+ \int_y^H \left[\langle v \rangle \frac{\partial \langle u \rangle}{\partial y} + \langle w \rangle \frac{\partial \langle u \rangle}{\partial z} \right] dy + \int_y^H \left[\langle u' \frac{\partial u'}{\partial x} \rangle + \langle v' \frac{\partial u'}{\partial y} \rangle + \langle w' \frac{\partial u'}{\partial z} \rangle \right] dy. \tag{4.9}$$

Several terms can be identified, each playing a role in describing how momentum is transferred, diffused, or advected in the flow, considering both viscous and turbulent effects:

- $\int_y^H \langle D \rangle dy$ is the mean canopy drag term, representing the mean drag exerted by the filaments;
- $\frac{\mu}{\rho U_b H} \left. \frac{\partial \langle u \rangle}{\partial y} \right|_y$ is the viscous shear term due to the viscosity of the fluid, involving the mean velocity gradient in the wall-normal direction $\frac{\partial \langle u \rangle}{\partial y}$;
- $\frac{\mu}{\rho U_b H} \int_y^H \frac{\partial^2 \langle u \rangle}{\partial z^2} dy$ is the viscous diffusion term, linked to the diffusion of momentum due to viscous forces in the spanwise direction and involving the second derivative of the mean velocity with respect to the spanwise direction $\frac{\partial^2 \langle u \rangle}{\partial z^2}$;
- $\int_y^H \left[\langle v \rangle \frac{\partial \langle u \rangle}{\partial y} + \langle w \rangle \frac{\partial \langle u \rangle}{\partial z} \right] dy$ is the mean advection term, representing the advection of momentum by the mean flow;
- $\int_y^H \left[\langle u' \frac{\partial u'}{\partial x} \rangle + \langle v' \frac{\partial u'}{\partial y} \rangle + \langle w' \frac{\partial u'}{\partial z} \rangle \right] dy$ is the turbulent shear term, which describes the mean contribute of fluctuations in transferring momentum.

Each term plays a different role in balacing the imposed pressure gradient along the flow direction $\left|\frac{\partial p}{\partial x}\right|\left(1-\frac{y}{H}\right)\cdot H$ driving the flow. The factor $\left(1-\frac{y}{H}\right)\cdot H$ accounts for the variation of the shear stress with height.

Equation 4.9 is valid for all three analyzed scenarios, as it is averaged only in the streamwise direction. For the fully-distributed canopy and open channel scenarios, where the spanwise direction is also homogeneous, the equation does not depend on the spanwise direction, unlike in the canopy patch. Therefore, to obtain a single plot for each case, the equation is also averaged in the spanwise direction, resulting in the plots shown in 4.8. The panels in the first column, 4.8a and 4.8d, refer to the fully-distributed canopy scenario, those in the middle column, 4.8b and 4.8e, to the open channel scenario, and the panels in the third column, 4.8c and 4.8f,

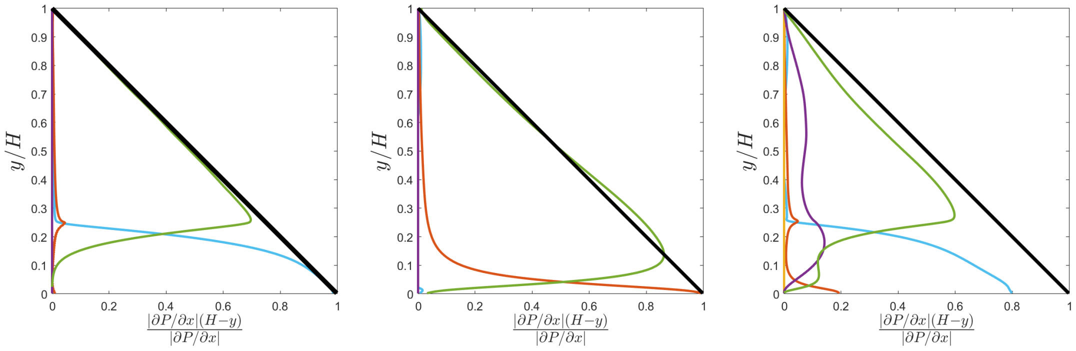

(a) $Ca = 10$, full canopy **(b)** Open Channel **(c)** $Ca = 10$, Canopy Patch

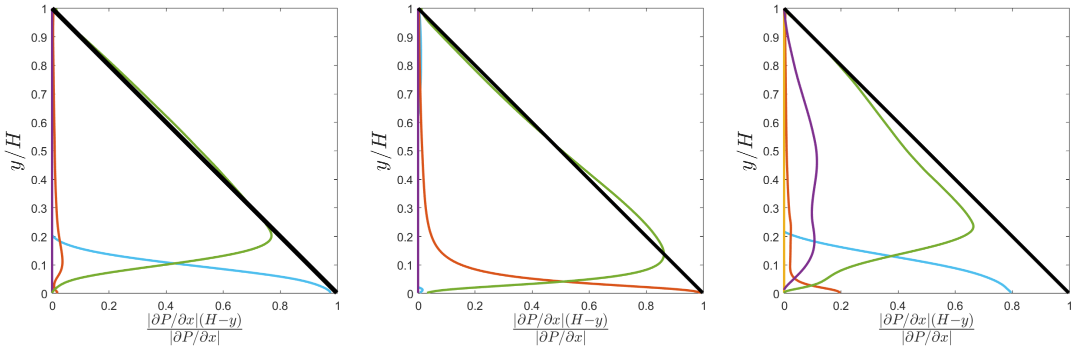

(d) $Ca = 100$, full canopy **(e)** Open Channel **(f)** $Ca = 100$, Canopy Patch

Figure 4.8: Shear stress balance for the three different scenarios - fully-distributed canopy, open channel and canopy patch - and for different values of Cauchy number - $Ca = 10$ and $Ca = 100$. The forcing term (black line) is balanced by the canopy drag (light blue line), the viscous shear (red line), the viscous diffusion (yellow line), the mean advection (purple line) and the turbulent shear (green line).

to the canopy patch scenario. Each row takes into a account a different flexibility of the filaments, with the panels in the first row referring to the more rigid case $Ca = 10$ and the ones in the second row referring to the more flexible scenario $Ca = 100$. Each line represents a different contribution to balancing the driving pressure gradient, represented by the black line: canopy drag (light blue), viscous shear (red), viscous diffusion (yellow), mean advection (purple), and turbulent shear (green).

Starting with the fully-distributed canopy scenario, it is evident that the forcing term is balanced by three main contributions: the viscous shear (red line), the turbulent shear (green line), and the canopy drag (light blue line). Near the bottom wall of the domain, the canopy drag dominates, fully balancing the forcing term at the wall. As we move in the wall-normal direction, the canopy drag decreases and becomes zero at the deflected tips of the filaments, as expected. In contrast, the turbulent shear increases as we move away from the bottom wall, becoming the dominant term just below the filament tips. Lastly, the viscous shear, although less significant compared to the other two contributions, reaches its peak at different locations. In the rigid scenario, it peaks at the deflected filament tips, while in the flexible scenario, its maximum occurs within the canopy, just below the top.

In the open channel scenario, instead, the primary contributors are the viscous shear and the turbulent shear, but there is no drag at all, consistent with the absence of filaments in the domain. Near the bottom wall the viscous shear is more significant, but overall, the turbulent shear has a dominant role.

For the canopy patch scenario, also the mean flow plays a key role in balancing the forcing term. In addition to the viscous shear, turbulent shear, and canopy drag, mean advection also contributes significantly. At the bottom wall, the canopy drag remains the most important term, as in the fully-distributed canopy scenario. However, unlike in the fully-distributed canopy, the canopy drag is not the only contributor at the bottom wall, since there is also a contribution from the viscous shear. While in the fully-distributed canopy scenario the viscous shear showed a single peak near the deflected filament tips for $Ca = 10$ and into the canopy for $Ca = 100$, in the canopy patch, the highest contribution of viscous shear occurs at the bottom wall, more similarly to the open channel scenario. This is expected, given that the shear balance equation was also averaged in the spanwise direction, and in the canopy patch, half of the domain is vegetated while the other half is not. This confirms that when the filaments are arranged such that they occupy only half of the domain, creating two edges aligned with the flow direction, the situation represents an intermediate case between having no vegetation and having the entire bottom wall covered by vegetation.

To highlight which term is predominant, figure 4.9 shows the wall-normal integrated contributions, normalized such that their sum equals one. The colors associated to each contribute are consistent to the ones previously used. In both the fully-distributed canopy and canopy patch scenarios, a lower Cauchy number shows a higher contribution of canopy drag in balancing the driving pressure gradient, indicating that the resistance exerted by the filaments on the flow is stronger when the filaments are more rigid, while greater flexibility reduces this effect. Viscous shear has the highest contribution for the open channel scenario, where it is one of the two primary terms balancing the driving force, whereas its role is marginal in both the fully-distributed canopy and canopy patch scenarios. Viscous diffusion is a negligible contribution in all three scenarios. Unlike the fully-distributed canopy and open channel, where the mean advection is negligible, the canopy patch scenario also exhibits a contribution from the mean advection. Lastly, turbulent fluctuations are by far the dominant term in the shear balance equation, thus highlighting their fundamental role over time.

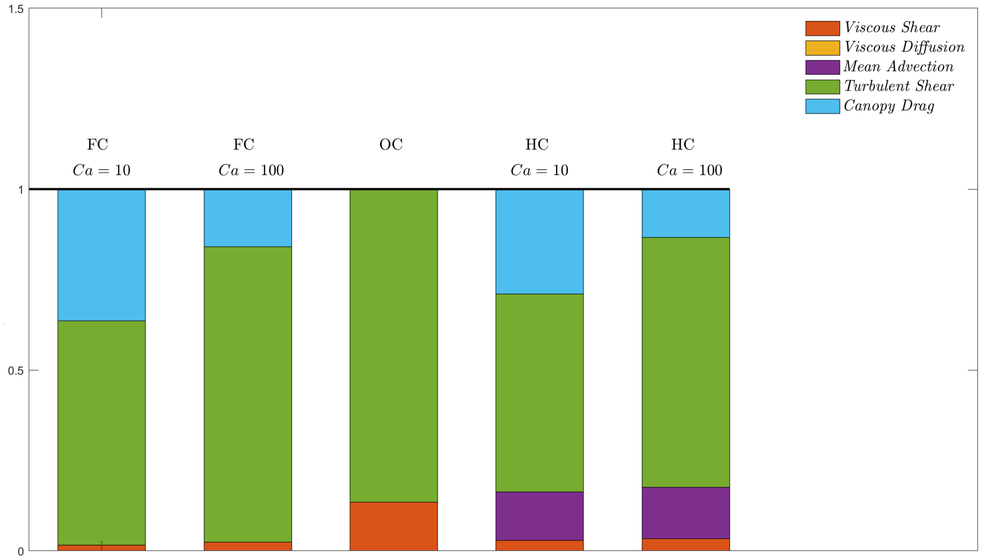

Figure 4.9: Wall-normal integration of the shear balance equation for the fully-distributed canopy (FC), open channel (OC), and canopy patch (HC) scenarios. Each color represents a different contribution balancing the forcing term: viscous shear (red), viscous diffusion (yellow), mean advection (purple), turbulent shear (green) and canopy drag (light blue). The contributions are normalized, such that their sum equals one.

4.1.3 Quadrant Analysis

The analysis of the shear equation highlighted the significant role of turbulent fluctuations in balancing the driving pressure gradient. However, it did not provide any insight into the instantaneous contributions of velocity fluctuations, which could offer a deeper understanding of the fluid dynamics and how the flow inside the canopy interacts with that on the outside. Therefore, the instantaneous velocity fields are now investigated by subtracting the mean flow, which has been averaged over both time and the homogeneous directions, as discussed previously in section 4.1.1. This approach, as outlined by Rota et al. 2024, allows to focus on the events occurring above the canopy and, in the canopy patch scenario, on the vertical plane separating the vegetated and non-vegetated regions. Studying the events is crucial in order to have a deeper understanding of how the flow inside the canopy interacts with the flow outside the canopy exchanging mass and momentum (Shen and Leclerc 1997.

In order to define what an event is, taking into account figure 4.10, we will call as u' the velocity fluctuation aligned with the direction of the flow and v' the velocity fluctuation in the direction perpendicular to the plane where the events are studied. In particular, we are interested in investigating the conditions under which the product of the two fluctuations is negative:

$$u'v' < 0, \tag{4.10}$$

which is equivalent to stating that the two fluctuations have opposite signs. Depending on the sign of the aforementioned velocity fluctuations, we distinguish two kind of events, named ejections and sweeps:

$$\begin{cases} u' < 0, \ \ v' > 0 & \textbf{Ejections} \\ u' > 0, \ \ v' < 0 & \textbf{Sweeps} \end{cases} \tag{4.11}$$

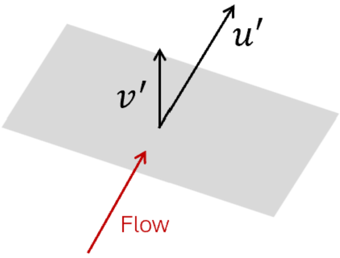

Figure 4.10: Definition of a generic event.

In order to understand the importance of events in the exchange of flow between the different regions of the domain, they have been studied on the planes which separate the canopy from the outer waters, as depicted in red in figure 4.11. In the fully-distributed canopy scenario, instantaneous events can only be analyzed on a horizontal plane above the canopy, as there is only the horizontal edge. As noted by Rota et al. 2024, the strongest sweeps and ejections are observed near the top of the canopy, thus the wall-normal location where the events are studied corresponds to the mean height of the deflected canopy tips. This applies also for the patch canopy above the vegetated region. However, for the canopy patch, it is also interesting to study the events occurring on the vertical planes separating the vegetated and non-vegetated regions. As a consequence, the definition in 4.1.3 varies depending on the plane being analyzed: on horizontal planes the relevant fluctuating velocity components are the streamwise u' and the wall-normal v', while on vertical planes the streamwise u' and the spanwise w'.

Ejections occur when the instantaneous velocity component aligned with the flow direction is lower than the mean velocity in that direction, while the instantaneous velocity component perpendicular to the plane where the events are studied is higher than the mean velocity in the same direction. This means that, when studied on the surface of the canopy, ejections tend to transport low-energy flow from inside the canopy to the outside. The opposite applies in the case of sweeps, which tend to transport high-energy flow from outside the canopy into the interior.

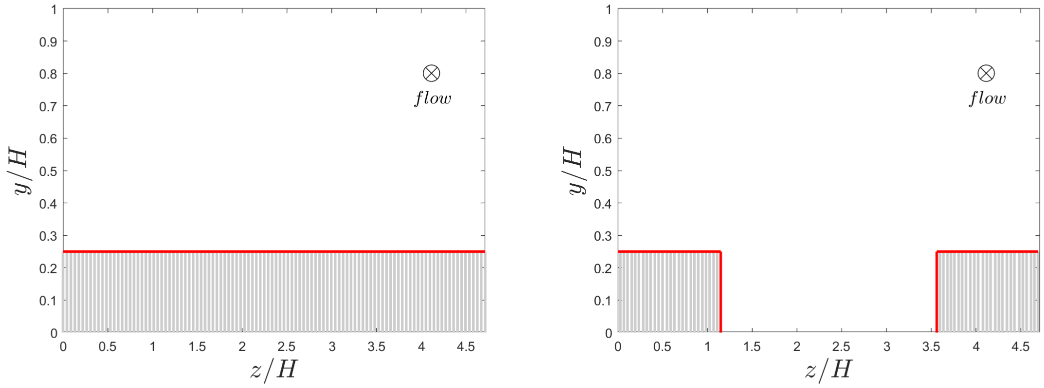

(a) fully-distributed canopy **(b)** Canopy Patch

Figure 4.11: Planes highlighted in red are the regions in which the events have been studied for both the fully-distributed canopy and the canopy patch scenarios.

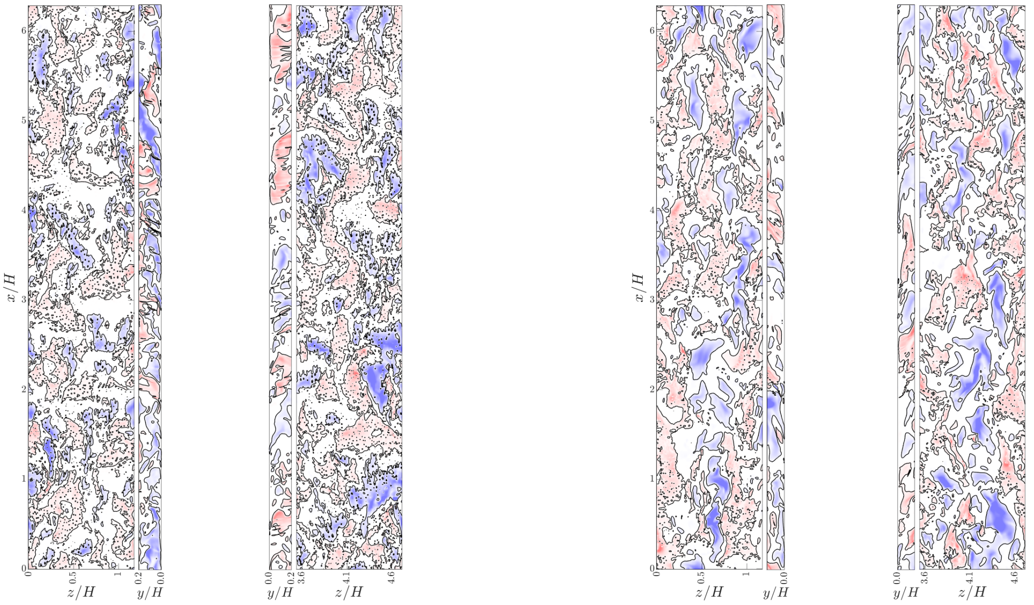

(a) Canopy patch, $Ca = 10$ **(b)** Canopy patch, $Ca = 100$

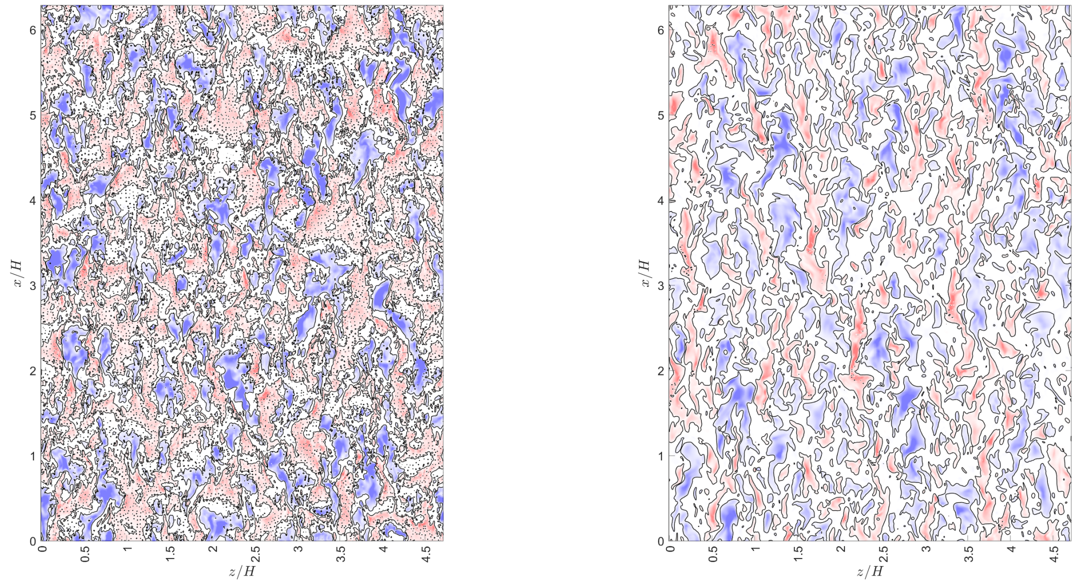

(c) fully-distributed canopy, $Ca = 10$ **(d)** fully-distributed canopy, $Ca = 100$

Figure 4.12: Events happening above the canopy at the average tips position. Sweeps are colored in blue while ejections in red. The panels in the first row refer to the canopy patch scenario, while the ones in the second row refer to the fully-distributed canopy. Panels (a) and (c) are for $Ca = 10$, while (b) and (d) for $Ca = 100$.

Figure 4.12 illustrates the instantaneous events happening above the canopy for the canopy patch scenario (panels in the first row) and both on the horizontal and lateral edge for the fully-distributed canopy scenario (panels in the second row), for the two different Cauchy number $Ca = 10$ (4.12a and 4.12c) and $Ca = 100$ (4.12b and 4.12d). For each panel corresponding to the canopy patch scenario, the first and last subplots represent events on horizontal planes where the streamwise u' and wall-normal v' velocity fluctuations are analyzed. The second and third subplots, on the other hand, depict events occurring at the interface between the vegetated and non-vegetated regions of the domain, where the streamwise u' and spanwise w' velocity fluctuations are considered. Sweeps are represented in blue, while ejections are shown in red. Consistent with the findings of Rota et al. 2024, the turbulence intensity appears higher in the more rigid case ($Ca = 10$), for both scenarios. This is indicated by a greater prevalence of coherent events compared to the more flexible case ($Ca = 100$) where such events are less pronounced.

To gain a more quantitative understanding of the dominant events over time, a quadrant analysis for the instantaneous Reynolds stresses $-u(t)v(t)$ was conducted. Referring again to figure 4.10, we recall that u' represents the streamwise velocity fluctuation, while v' is the velocity fluctuation perpendicular to the plane where events are analyzed. Consequently, the definition varies depending on whether the horizontal or vertical plane is considered. The joint probability density function (J-PDF) is then calculated and displayed on a $u' - v'$ plane (Wallace 2016) which is divided into four quadrants, basing on the approach first outlined by Raupach 1981:

$$\begin{cases} Q1 : u' > 0, v' > 0 & \text{outward interaction} \\ Q2 : u' < 0, v' > 0 & \text{ejection} \\ Q3 : u' < 0, v' < 0 & \text{inward interaction} \\ Q4 : u' > 0, v' < 0 & \text{sweep} \end{cases}$$

Depending on the quadrant where the peak of the joint probability density function lays, we can define which of the above mentioned interactions dominates.

This analysis was performed at the horizontal edge of the canopy and, in the case of the canopy patch, also at the vertical edge, for both Cauchy numbers. Thus, figure 4.13 reports the contour of the J-PDFs computed on the horizontal planes above the canopy highlighted in figure 4.11 for the canopy patch (panels 4.13a and 4.13b in the first row) and for the fully-distributed canopy (panels 4.13c and 4.13d in the second row), while figure 4.14 shows the J-PDFs computed on the vertical planes separating the vegetated side to the non-vegetated one. The peaks of the

J-PDFs, shown as black dots in the graphs, highlight which event is dominant over time.

Several studies already showed that, for the fully-distributed canopy scenario, the peak of the joint probability density function is located in the second quadrant $u' < 0$ and $v' > 0$ (e.g. Rota et al. 2024), indicating that ejections dominate over sweeps over time. The J-PDFs stretch into the fourth quadrant $u' > 0$ and $v' < 0$, highlighting the presence of less dominant sweep events. The same pattern is observed also for the canopy patch, with ejections as the dominant events and a similar shape of the J-PDFs, suggesting that, regardless of vegetation distribution on the bottom-wall of the domain, the dynamics of the events happening above the canopy in the vegetated region is not altered, with a more frequent exchange of low momentum fluid from inside the canopy.

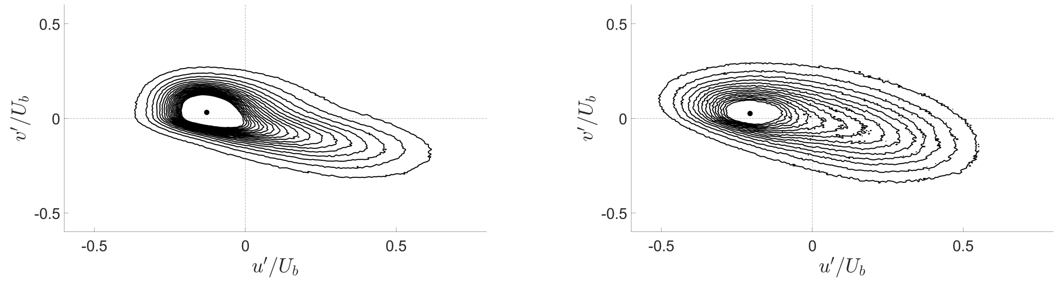

(a) Canopy patch, $Ca = 10$ **(b)** Canopy patch, $Ca = 100$

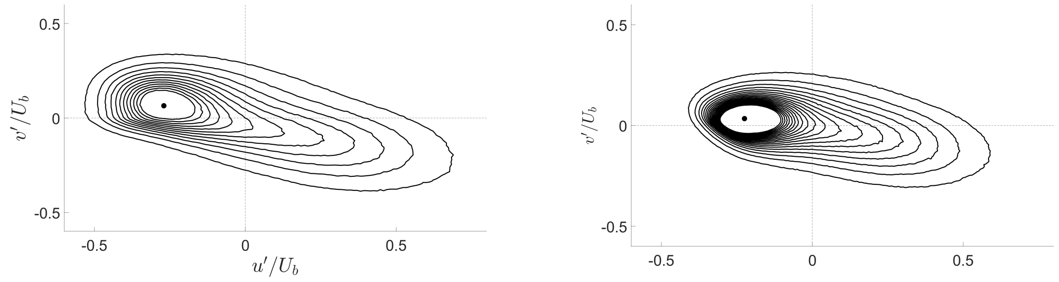

(c) fully-distributed canopy, $Ca = 10$ **(d)** fully-distributed canopy, $Ca = 100$

Figure 4.13: Joint Probability Density Function (J-PDF) of the velocity fluctuations streamwise u' and wall-normal v' on the horizontal planes above the canopy. The panels in the first row refer to the canopy patch scenario, while the ones in the second row refer to the fully-distributed canopy. Panels (a) and (c) are for $Ca = 10$, while (b) and (d) for $Ca = 100$. The black dots correspond to the peaks of the J-PDFs.

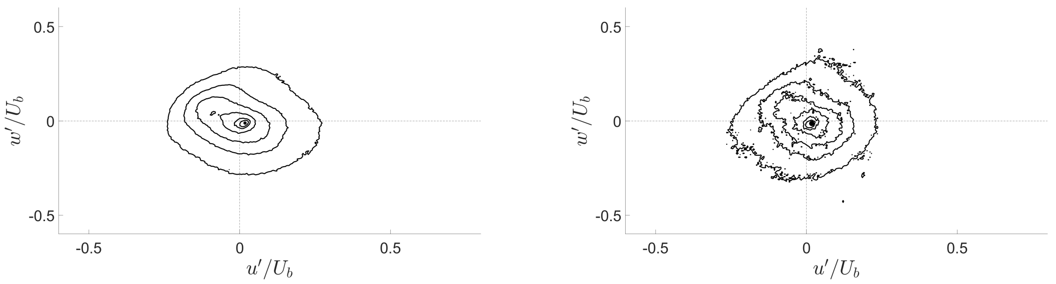

(a) Canopy patch, $Ca = 10$ **(b)** Canopy patch, $Ca = 100$

Figure 4.14: Joint Probability Density Function (J-PDF) of the velocity fluctuations streamwise u' and spanwise w' on the vertical planes for the canopy patch scenario. Panels (a)is for $Ca = 10$, while (b) for $Ca = 100$. The black dots correspond to the peaks of the J-PDFs.

Figure 4.14 presents the joint probability density functions (J-PDFs) of the streamwise and spanwise velocity fluctuations (u' and w', respectively) on the vertical planes that separate the vegetated region from the non-vegetated region within the canopy patch. In this case, the peak of the J-PDFs is situated in the fourth quadrant ($u' > 0$, $w' < 0$), indicating that sweeps are the dominant events occurring on these vertical planes. This suggests that the lateral edge of the canopy is dominated by the exchange of high-momentum flow coming from the main channel, in a completely opposite way with respect to the event dynamics over the horizontal edge.

4.1.4 Two-point Correlations

At the beginning of the present study, by characterizing the mean flow properties, we concluded that when vegetation partially obstructs the channel, as in the configuration considered here, the flow can be modeled as either a fully-distributed canopy or an open turbulent channel, depending on the region of the domain and its distance from the lateral junction. It is interesting to investigate whether this conclusion also applies to velocity fluctuations. Although the quadrant analysis provided some insights into the turbulent motion - suggesting that the distribution of vegetation in the domain is not a critical factor influencing the events occurring above the horizontal edge of the canopy - examining the two-point correlations of velocity fluctuations for the canopy patch scenario, and comparing them with the two limiting scenarios, allows us to explore whether this decomposition into two simpler problems is also valid for turbulent activity.

The two-point spatial correlation is a statistical measure used to quantify the spatial relationships between two points in a random field, such as a velocity field, scalar field, or any other physical quantity. Since we aim to understand the velocity fluctuations, we focus on the streamwise velocity fluctuations u', which were identified, through a comparison with the other two velocity fluctuation components, as the most dominant. It can be defined as:

$$R_{u'u'}(\mathbf{r},\mathbf{x},t) = \langle u'(\mathbf{x},t)u'(\mathbf{x}+\mathbf{r},t)\rangle,$$

where $u'(\mathbf{x},t)$ and $u'(\mathbf{x}+\mathbf{r},t)$ are the streamwise velocity fluctuations at positions $\mathbf{x}$ and $\mathbf{x}+\mathbf{r}$, $\mathbf{r}$ is the space separation between two points and $\langle\cdot\rangle$ denotes a temporal average (Pope 2000).

The correlations were computed for all the analyzed scenarios and compared at two fixed wall-normal coordinates. For the fully-distributed canopy and the turbulent open channel, where homogeneity in the spanwise direction is present, a single correlation function was obtained for each wall-normal position considered. In contrast, for the canopy patch, due to its inhomogeneity in the spanwise direction, three representative spanwise coordinates were selected: one within the canopy, one at the center of the non-vegetated main channel, and one at the junction between the two regions, as in figure 4.15. Thus, the coordinate vector $\mathbf{x}$:

$$\mathbf{x} = (x, \overline{y}, \overline{z}). \tag{4.12}$$

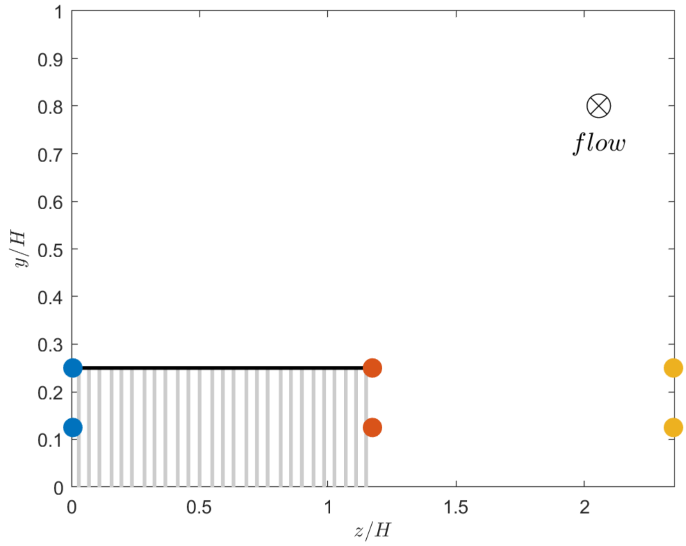

Figure 4.15: Locations in which the correlations have been computed.

Once computed, the two-point correlation functions have been normalized as:

$$R_{u'u'}(\mathbf{r}, \mathbf{x}, t) = \frac{\langle u'(\mathbf{x}, t) u'(\mathbf{x} + \mathbf{r}, t) \rangle}{\langle u'(0, \overline{y}, \overline{z}, t)^2 \rangle}.$$

The results suggest that, outside the junction region, the shape of the correlations

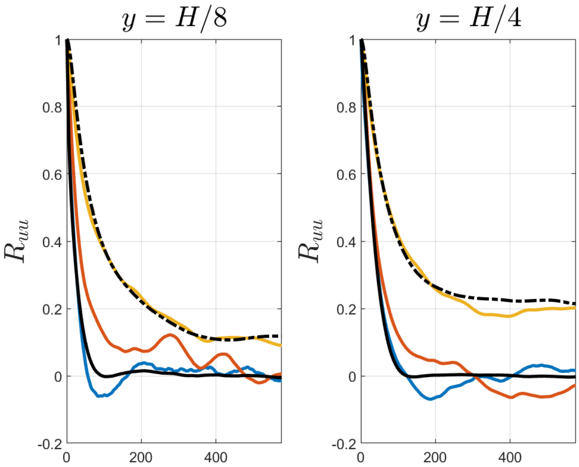

(a) $Ca = 10$

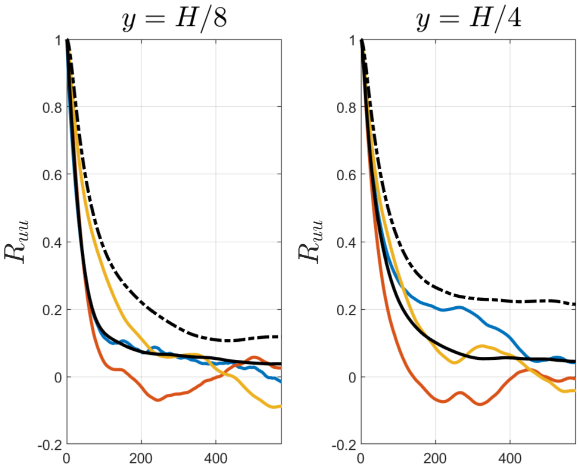

(b) $Ca = 100$

Figure 4.16: Two-point correlations of streamwise velocity fluctuations at different spanwise coordinates, with the wall-normal coordinate fixed. The solid black line represents the fully distributed canopy, while the dashed black line corresponds to the turbulent open channel. The colored lines indicate specific positions in the spanwise direction, with the color scheme matching that used in Figure 4.15.

for the canopy patch scenario closely resembles those of the two limiting scenarios, providing further confirmation that the problem can be modeled using two simplified cases. This resemblance is more apparent for the scenario with more rigid filaments, while in the more flexible case, the motion of the filaments may introduce additional dynamics that alter the turbulent characteristics.

4.2 Filament Dynamics

THaving characterized the fluid dynamics, we now turn to the behavior and movement of the filaments within the flow. When dealing with flexible filaments, the problem shifts from a purely fluid-dynamics problem to one more to fluid-structure interaction. We begin by examining the mean position of the canopy tips in Section 4.2.1, followed by an analysis of the average deflection of each filament in Section 4.2.2, and conclude with a study of their oscillatory behavior through the velocity fluctuation spectra in Section 4.2.3.

4.2.1 Average tip position

Since the filaments are flexible, they deflect when impacted by the incoming flow, adopting a more streamlined shape in a process known as *reconfiguration*. The extent of the deflection depends on the filament's flexibility, which is governed by

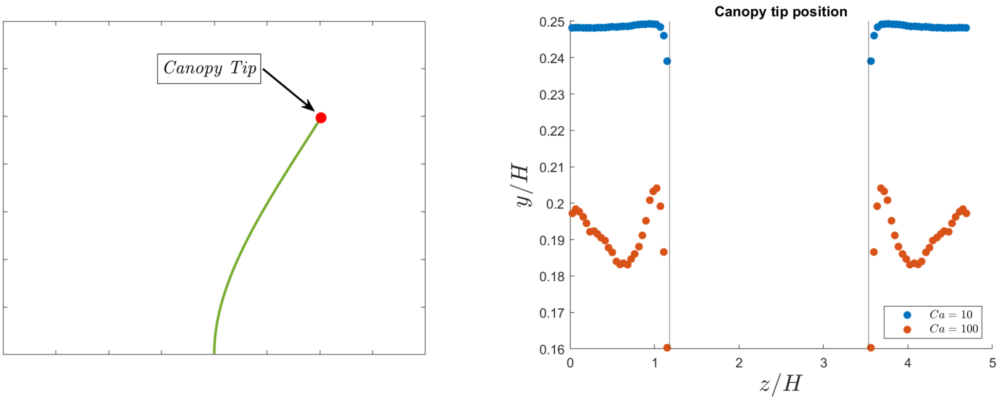

(a) **(b)**

Figure 4.17: Panel (a) displays a generic deflected canopy tip. Panel (b) shows the time- and streamwise-averaged positions of filament tips for the more rigid case (blue dots, $Ca = 10$) and the more flexible case (red dots, $Ca = 100$). The vertical black line represent the boundary between the vegetated and the non-vegetated sides.

the Cauchy number: the higher the Cauchy number, the greater the deflection. Given that the extremities of the filaments are expected to experience the most deflection, we begin by analyzing the average position of the canopy tips (figure 4.17a) in the canopy patch scenario. It is a double average in time and in the homogeneous streamwise direction.

Figure 4.17 shows the front view of the average height of the deflected filaments. The blue dots refer to the more rigid case ($Ca = 10$), while the red dots to the more flexible case ($Ca = 100$). The black vertical lines indicate the boundary between

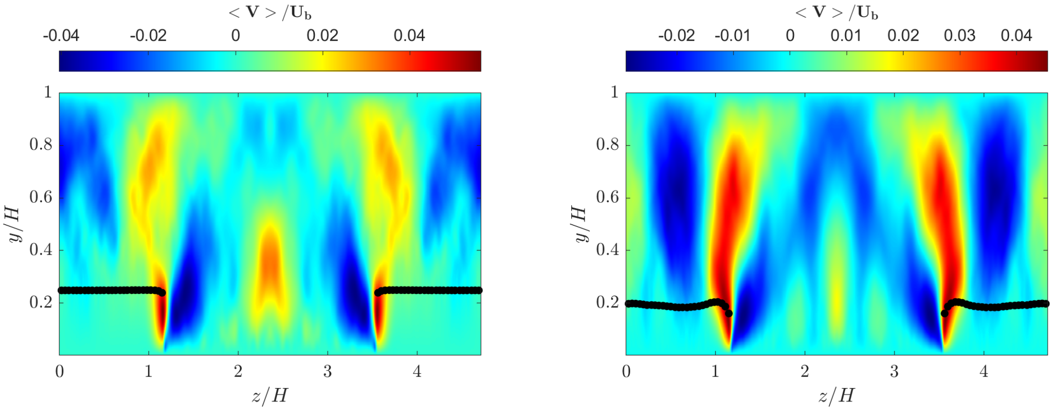

(a) $\langle V\rangle/U_b$, $Ca = 10$ **(b)** $\langle V\rangle/U_b$, $Ca = 100$

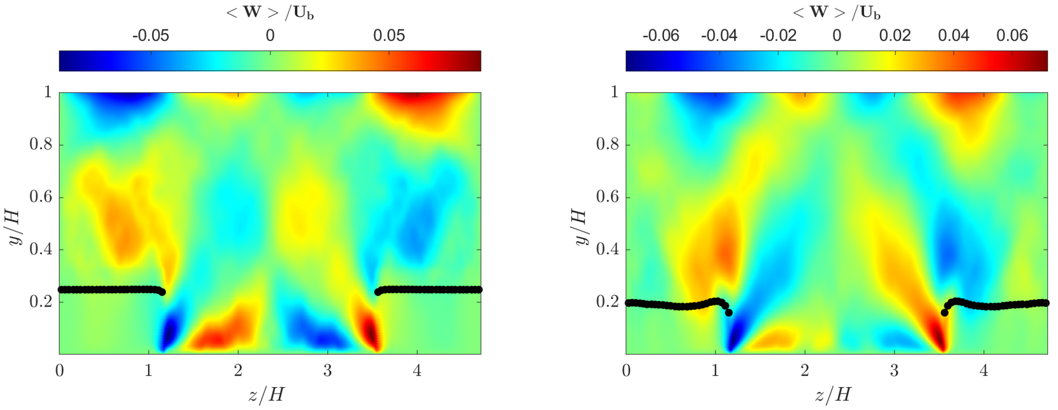

(c) $\langle W\rangle/U_b$, $Ca = 10$ **(d)** $\langle W\rangle/U_b$, $Ca = 100$

Figure 4.18: Average positions of the canopy tips (black dots) at varying spanwise positions of the filaments, displayed against the mean velocity field in the background for $Ca = 10$ (panels (a) and (c)) and for $Ca = 100$ (panels (b) and (d)). Panels in the first row show the mean wall-normal velocity, while panels in the second row show the mean spanwise velocity.

the vegetated and non-vegetated regions. As expected, the more rigid filaments generally exhibit less deflection than the more flexible ones. A decreased average height of flexible canopies displaces the canopy shear layer closer to the bed, leading to a notable increase in near-bed turbulence levels, weaking momentum transfer in the shear layer and diminishing vertical mixing (Abdolahpour et al. 2018).
The extent of deflection varies with the spanwise position of the filaments, with those closer to the non-vegetated region showing greater deflection. This observation suggests that the filaments act as a shield for one another, providing mutual protection against deflection. Moreover, being the filaments more deflected in the more flexible case, the frontal area of the canopy seen by the incoming flow is smaller than in the more rigid case, resulting in less blockage of the incoming flow.

The pattern of filament heights across the spanwise direction indicates that some filaments within the canopy deflect more than others. By displaying the average positions of the canopy tips against the mean flow field, we gain better insight into the interaction between the flow and the filaments, as illustrated in figure 4.18. Panels in the first row show the mean wall-normal velocity component, while panels in the second row show the mean spanwise velocity. Where the filaments are less deflected, the wall-normal velocity component indicates an updraft of fluid moving from inside the canopy to the outside. In contrast, near the boundary between the vegetated and non-vegetated regions, where the filaments are more deflected, the flow tends to be directed from outside the canopy to the inside. As discussed in 4.1.1, this flow pattern arises from the presence of mean vortexes forming within the domain, as suggested by the correspondence between the wall-normal and spanwise velocity distributions.

4.2.2 Average deflection

By analyzing the height of the filaments, we observed a dependence of their deflection behavior on the spanwise coordinate. Therefore, we aim to investigate whether this pattern is also evident when examining the average deflection of the entire filaments, rather than just the canopy tips. For this reason, we consider a total of six filaments at different spanwise locations, as illustrated in figure 4.19. For each filament, we examine the mean deflection in the streamwise and in the spanwise directions along with the average root mean square of the oscillations. As with previous analyses, the averaging is conducted both over time and in the homogeneous streamwise direction.

Figure 4.20 displays the average streamwise deflection (black solid line) of the analyzed filaments for the two levels of flexibility. The shaded regions represent the root mean square of the displacements from the mean position, indicating that the filaments do not reach a static fully deflected state. Instead, they oscillate around their average deflected position. Filaments at the boundary between the vegetated and non-vegetated regions experience greater average deflection compared to those located deeper within the canopy, further confirming the shielding effect of the filaments. Additionally, the oscillations around the mean position are more pronounced at the boundary than for the filaments situated further inside the canopy.

Similar conclusions can be drawn from examining the mean deflection behavior of the filaments in the spanwise direction, as shown in figure 4.21b. In this case as well, the filament separating the vegetated and non-vegetated sides tends to oscillate more than those located deeper within the canopy.
Both the streamwise and spanwise deflections confirm that a higher Cauchy number leads to increased filament flexibility, resulting in greater deflection. This, in turn, reduces the cross-sectional area of the canopy and decreases the obstruction of the channel, thereby confirming the reduced drag in this configuration.

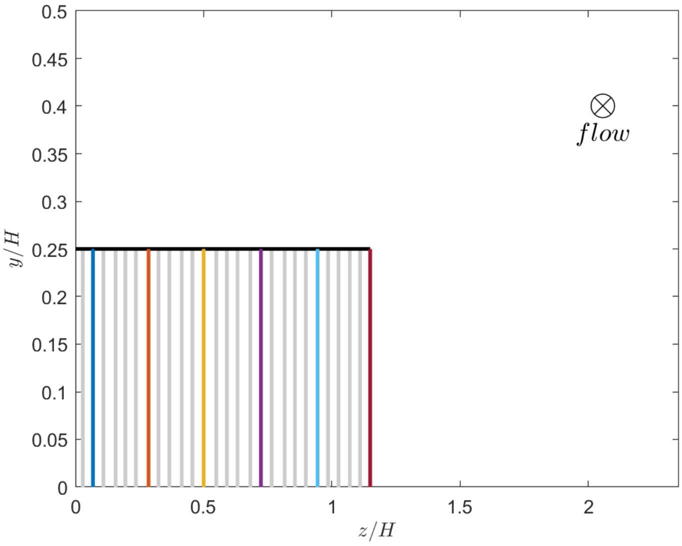

Figure 4.19: Spanwise location of the analyzed filaments

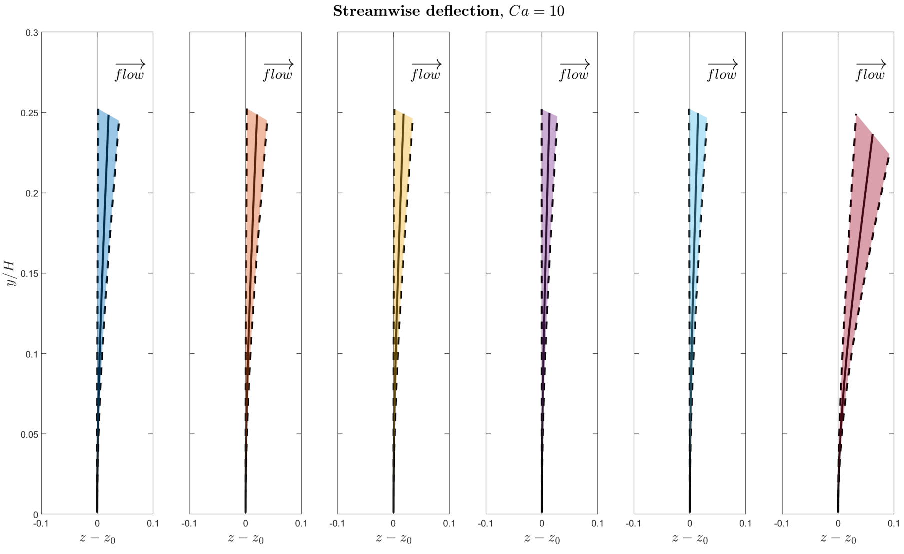

(a) $Ca = 10$

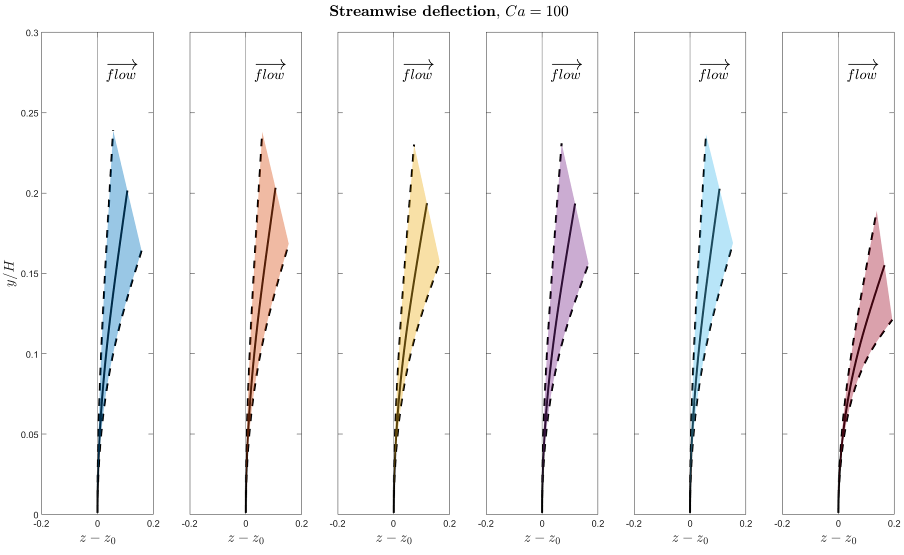

(b) $Ca = 100$

Figure 4.20: Time and streamwise average deflection of the filaments in the streamwise direction. The black solid line represents the mean streamwise position of the filament, while the colored regions represent the root mean square of the filaments oscillations.

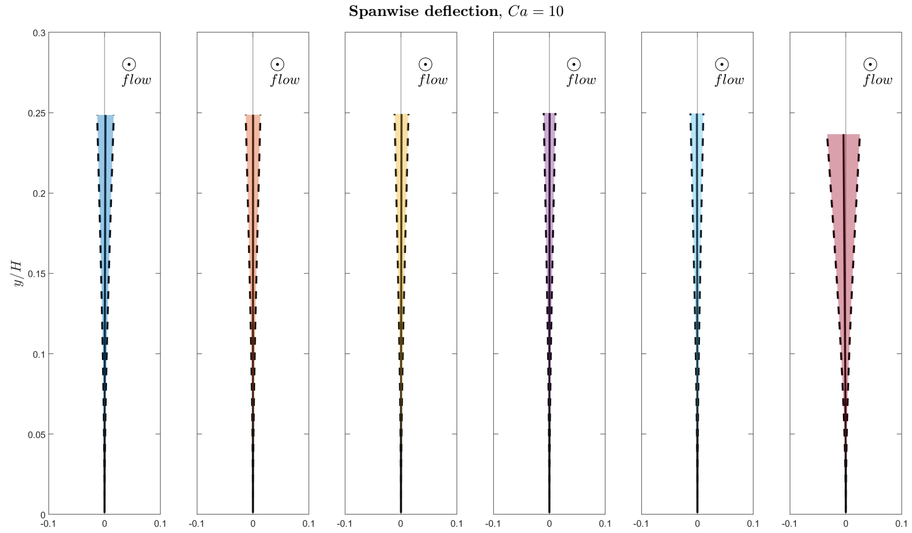

(a) $Ca = 10$

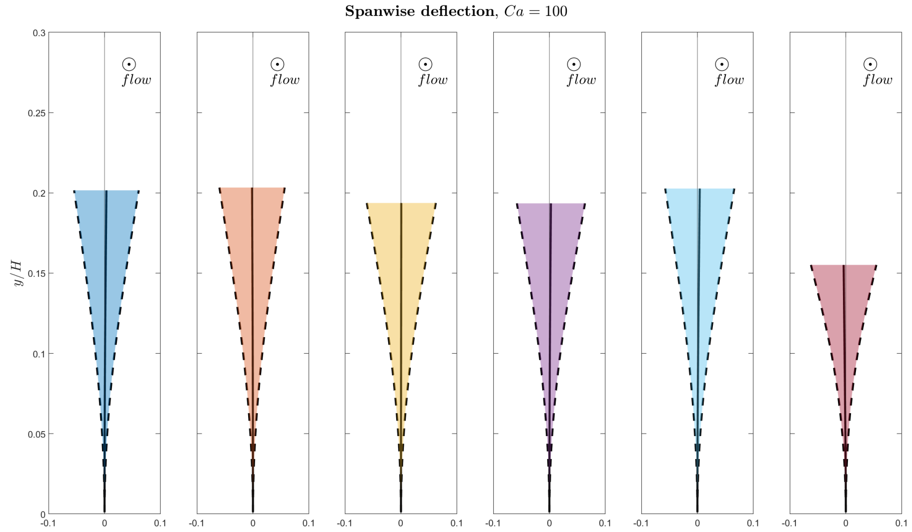

(b) $Ca = 100$

Figure 4.21: Time and streamwise average deflection of the filaments in the spanwise direction. The black solid line represents the mean streamwise position of the filament, while the colored regions represent the root mean square of the filaments oscillations.

4.2.3 Canopy tip velocity spectra

By analyzing the mean deflection of the filaments and the root mean square of their displacement, we highlighted their oscillatory nature. The filaments do not reconfigure into a static, fully deflected state, but instead sway around their average position. To gain further insight into the dynamics of these oscillations, we now focus on the spectra of velocity fluctuations at the tips of the canopies. As observed previously, we expect a dependence on the spanwise direction, with filaments closer to the non-vegetated region exhibiting more intense oscillations. Therefore, for each spanwise position of the filaments, we computed the Fourier Transform of the spanwise velocity at the filament tips, yielding 3D spectra.

Figure 4.22 presents a top view of the resulting 3D spectra for the two flexibility cases, spanning from the location where the periodic boundary condition is applied to the center of the non-vegetated region, showing only half of the domain due to its symmetry. The y-axis represents the logarithm of the frequency, normalized by the channel height H and the bulk velocity U_b. As confirmed by Foggi Rota et al. 2024 and Rota et al. 2024, the more rigid filaments tend to oscillate at a frequency close to their natural frequency, while the more flexible filaments oscillate at a relatively constant frequency, independent of their structural characteristics, corresponding to the bulk turbulence frequency. The black dashed-dotted line

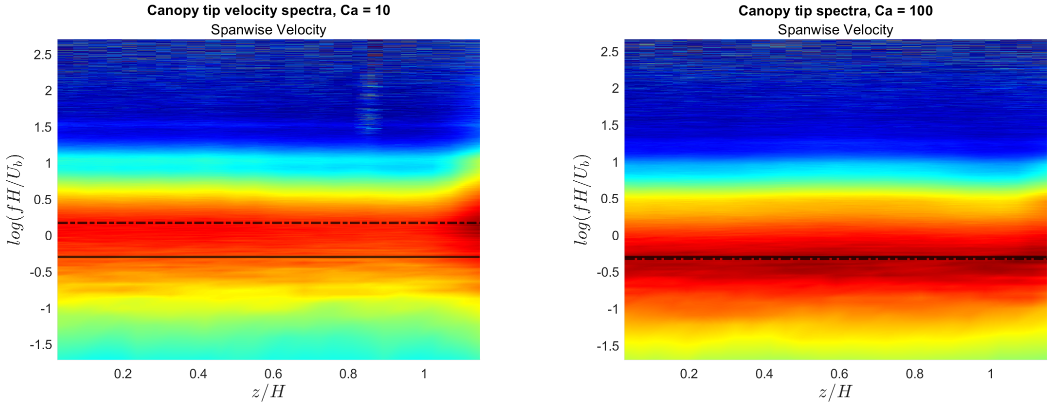

(a) $Ca = 10$ **(b)** $Ca = 100$

Figure 4.22: Top view of the 3D spectra of the spanwise velocity of the filament tips for $Ca = 10$ (a) and $Ca = 100$ (b). The dashed dotted line corresponds to the natural frequency of the filaments f_{nat}, while the solid line represents the bulk turbulence frequency.

represents the logarithm of the natural frequency of the filaments, defined as:

$$f_{nat} = \frac{3.516}{dh^2\sqrt{\gamma/(\rho_s \pi^3)}},$$

where d is the cross-section diameter of the filaments, h is their length, γ is their bending rigidity and ρ_s is their density. On the other hand, the black solid line represent the logarithm of the bulk turbulence frequency:

$$f_{turb} = 0.5\frac{U_b}{H}.$$

The plots confirm that for the more rigid filaments ($Ca = 10$), the oscillation frequency is closer to the filaments' natural frequency, whereas more flexible filaments ($Ca = 100$) approach the constant bulk turbulent frequency. This latter scenario resembles the result obtained by Tschisgale et al. 2021, who concluded that vegetation responds almost passively to the fluid, thus reflecting the local flow conditions.

The more notable finding, however, is that the oscillatory behavior of the filaments indeed depends on their spanwise location, as already highlighted previously. Filaments nearer to the non-vegetated region not only exhibit a greater extent of oscillations, but also sway over a broader range of frequencies compared to those positioned deeper within the canopy.

Chapter 5

Discussion

Through Direct Numerical Simulations, we analyzed the dynamics of both the fluid and the filaments in a canopy patch consisting of 7776 flexible filaments occupying half of the bottom wall. The domain is, thus, divided into two regions, one with vegetation and the other one without. Two levels of filament flexibility were analyzed - one where the filaments are nearly rigid and another where they deflect significantly under the incoming flow. The results were then compared with two limiting cases, an open channel with no filaments and a full canopy, where filaments cover the entire bottom wall of the domain. The latter case, extensively studied by Rota et al. 2024, paved the way for exploring more complex filament configurations in the domain.

5.1 Mean flow characteristics

An analysis of the mean flow suggests that the canopy acts as a shield to the incoming flow, as the velocity tends to zero inside the canopy. This is due to the resistance exerted by the filaments, which slows the flow in the canopy region. As the filaments are flexible, we can assume that the drag follows the scaling proposed by Alben et al. 2002 $D \propto U^{4/3}$, instead of the quadratic law, which was shown to not correctly predict the drag, due to their reshaping.

Due to the abrupt change in the flow velocity both in the vertical and transverse directions, two shear layers form and coexist: an horizontal one above the canopy and a vertical one on the lateral edge. Thus, starting from inside the vegetated region and moving either vertically or laterally, the streamwise velocity increases. As the canopy patch inhibits the flow from flowing, the flow is redirected in the main-channel, where the mass flow is higher than that in the non-vegetated region. This enhances erosion and sediment transportation processes in the river bed of the main channel, as suggested by Colomer and Serra 2021 and W.-x. Huai et al.

2021. The shielding effect of the filament is felt also outside of the canopy region, with a greater extent in the case of the more rigid filaments.

5.1.1 Horizontal edge

Given the transverse inhomogeneity of the computational domain due to the finite width of the canopy, there is a dependence of the vertical streamwise velocity profiles from the location in the spanwise direction. In fact, profiles inside the canopy resemble those of the submerge fully-distributed canopy, while profiles towards the center of the non-vegetated region, thus, in the middle of the main open-channel, resemble those of a turbulent open channel without vegetation. This suggests not only that the canopy patch lays in between the other two limit scenarios, but also that, far from the lateral edge of the canopy patch, the flow can be simplified into bi-dimensional problems. Thus, far from the junction, the vegetated region can be modeled as a fully-distributed submerged canopy, while the non-vegetated region can be modeled as an open channel without vegetation. In this way, while for profiles in the middle of the non-vegetated region no inflection points are to be found, two inflection points are observed in the profiles inside the canopy region, as also highlighted by Rota et al. 2024, one within the canopy and another near the canopy top. These two inflection points gradually merge as we move toward the center of the domain (non-vegetated region), indicating that the influence of the canopy extends also in the main non-vegetated channel.
A better understanding of the flow near the lateral edge is needed. In the junction region and, especially, at the main-channel side, the velocity profiles perform a more marked S-shape profiles, unlike Nezu and Onitsuka 2001 who highlighted a almost-linear velocity profile at the interface between the rigid cylinders and the open water, due to the influence of both the vegetated and the non-vegetated regions. This is probably due to the flexible nature of the filaments considered in our study, but which aligns well with the study performed by Pang et al. 2014 on patch of real vegetation, that is *eel grass*. The S-shape becomes more irregular at a higher flexibility of the filaments.

As for the Rayleigh theorem, an inflection point in the velocity profile is a necessary condition for flow instability. Inflectional instability is responsible for the generation of vortex structures, which are responsible for the exchange of mass between the inside and the outside of the canopy. Similarly to the secondary currents highlighted by Unigarro Villota et al. 2023, two counter-rotating cells form above the vegetated region, resulting in an updraft of low-energy flow from inside the canopy to the outside. This is an interesting result for many applications, as this particular flow structure could have an impact on the vertical transport of sediments and particles, reducing their accumulation on the ground. This is a fertile ground for future studies.

5.1.2 Vertical edge

To better understand the flow dynamics at the lateral edge of the canopy patch, a look at the horizontal streamwise velocity profiles was given. An abrupt increase of velocity is to be found at the junction, with flow slowed down inside the canopy and accelerated in the main channel. This abrupt change is more marked inside the canopy and, as we move up above the canopy top, the discontinuity in the streamwise velocity is less marked, with velocity profiles close to the top of the computational domain that do not reach unperturbed condition. This is due to the fact that the flow accelerates over the canopy. Thus, the height of the channel represents a parameters, whose influence on the flow structure would be interesting to be further investigated.

An inflection point forms right in at the interface between the vegetated and the non-vegetated regions, leading to a flow instability and the generation of vortex structures similar to those forming above the canopy. Those structures are responsible, over time, for bringing high-energy flow from the main channel into the canopy through the lateral edge. Thus, flow enters the canopy through the lateral edge end than exits through the horizontal edge, as a consequence of secondary currents arising from the transverse inhomogeneity of the domain.

5.2 Shear Balance Equation

Mean flow plays a significant role also in balancing the pressure gradient, which is the driving force of the flow, unlike in the open unvegetated channel and in the submerged fully-distributed canopy. Besides this, the shear stress balance equation suggests again that the canopy patch is a scenario which lays in between the limiting ones considered.

In the open channel, indeed, two terms play a key role, the viscous shear, which reaches its peak in the river bed, and the turbulent shear, which gives the highest contribution. On the other hand, for the fully-distributed submerge canopy, the viscous shear plays a secondary role, with the drag exerted by the filaments and the turbulent shear being the predominant terms. In particular, the first one has its highest value in the near-bed region and becomes zero at the top of the canopy, as above this region there are no filaments. Turbulent shear, instead, reaches its peaks in the near top region, as expected from the turbulence activity which is higher in this location, as widely-documented in literature (e.g. White and H. M. Nepf 2008).

Given the inhomogeneity in the spanwise direction, to obtain a single shear balance equation, the quantities have been averaged also in the spanwise direction, thus obtaining an average balance of the whole domain. A part from the mean flow which has a contribute, turbulent shear has still the a major role, reaching its peak near the canopy top. On the other hand, although playing a key role, the drag term isn't the only contribute in the near-bed region, as the viscous shear reaches a peak value in this location, even if with a weaker contribute, thus resembling the open channel scenario.

The effect of flexibility in balancing the forcing pressure gradient is to be found in the drag term, which decreases with an increase in the filament flexibility in spite of an increase in the turbulent shear. This is due to the reduced drag experienced by flexible filaments, as highlighted by Alben et al. 2002. The higher the filament flexibility, the greater they bend when hit by the flow, resulting in a movement of the shear layer closer to the river bed. This explains also the location of the peak of the turbulent shear (and at the same time of when the drag term reaches the zero), which moves towards the channel bed as a result.

5.3 Velocity fluctuations

The analysis of the shear balance equation revealed the importance of turbulent activity and, thus, velocity fluctuations. However, it provides only an average perspective on their role, but it is essential to focus on their instantaneous behavior as well. As we concluded that the highest turbulent activity is to be found near the canopy top, a characterization of the events happening here is essential. Moreover, given the existence of a lateral edge, an analysis of the turbulent activity here is also important.

Sweeps and ejections have been reported to have a dominant role, with respect to outer and inner interaction, in the exchange of mass and momentum between the inside and the outside of the vegetated region (Devi and Kumar 2016a). Ejections dominate over sweeps on horizontal planes above the vegetated regions, similarly to what happen for fully-distributed submerged canopies (Nezu and Sanjou 2008, Foggi Rota et al. 2024). Moreover, joint probability contours display consistent shapes across the two different vegetation distributions. This result suggests that the instantaneous interaction between the outer flow and the flow within the canopy is primarily driven by the outward transport of low-momentum fluid from within the canopy. On the other hand, on the vertical plane that separates the vegetated and non-vegetated regions, sweeps predominate, transporting high-momentum flow from the outer region into the canopy, thus suggesting that an opposite mechanism works here.

Further insights into the role of fluctuations were obtained by analyzing the two-point correlations of the streamwise velocity fluctuations, u'. Two wall-normal locations were selected for this analysis, and for each, correlations were calculated at three distinct spanwise coordinates. The results confirm that also the turbulence dynamics in the canopy patch scenario lie between those observed in the open channel and full canopy cases. Specifically, correlations at spanwise positions within the canopy tend to align with those of the full canopy, whereas correlations at the center of the non-vegetated region are more similar to those of the open channel.

5.4 Filament Dynamics

Since dealing with flexible filaments, it is no more a pure fluid-dynamics problem, but a strong coupling between fluid and filament dynamics is to be found. When the flow hits the canopy patches, filaments deflect in the same direction of the streaming flow, thus assuming a stream-shaped configuration which has been called *reconfiguration* (Vogel 1994). The higher the flexibility of the structures, the more streamlined their shape. Thus, the average position of the tip of the filament is lower than in their undeflected state, as also supported by the location of the outer inflection point in the velocity profiles, which tend to move below the canopy top for the more flexible filaments and, so, the horizontal shear layer. This results in a reduced cross-sectional area and, consequently, a lower obstruction of the channel by the canopy, compared to more rigid filaments, explaining the reduced drag in flexible configurations, as highlighted by Alben et al. 2002.

A dependence on the spanwise position is shown. The mean position of the tips of the canopy aligns well with that of the mean flow. It was, indeed, highlighted that secondary circulation arises in the domain in the form of vertical circulating cells which result in a vertical upflow. Where the vertical upflow is to be found, the tip of the filaments is less deflected, thus suggesting a strong coupling with the mean properties of the flow.

Filaments do not assume a static state, but instead, oscillate around their mean position both in the streamwise and spanwise direction, with more flexible filaments having a greater extent of oscillation. Although the overall dynamics of the filaments in the patch scenario resemble those in the full canopy, the oscillatory behavior varies based on spanwise position. Filaments closer to the non-vegetated region show greater deflection and tend to oscillate across a wider frequency range compared to those located deeper within the canopy. The frequency of the oscillation dictates which one between the structural properties of the filaments and the vortex structures dominates. Spectra of velocity fluctuations at the canopy tip showed that, in the more rigid scenario, filaments oscillate near their natural frequency f_{nat}, while in the more flexible scenario, they oscillate at the characteristic bulk turbulence frequency f_{turb}, which remains constant regardless of flexibility. These findings are consistent with results by Foggi Rota et al. 2024, who analyzed a single filament's dynamics, and later confirmed by Rota et al. 2024 in full-distributed canopy. In regimes where the frequency of the instability approaches and equals the swaying frequency of the filaments, a lock-in regime arises, which resembles that characteristic of vortex-structure interaction problems (Py, E. D. Langre, et al. 2006).

Chapter 6

Conclusions and concluding remarks

Vegetation plays a crucial role in rivers and marine environments, growing in various distributions, often forming patches that alter the natural development of the flow. When the height of the plants is shorter than the water depth, the structures are fully submerged, resulting in multiple edges forming around the vegetation patches. These edges give rise to complex turbulent structures in the flow domain.

In this thesis, we considered a partially obstructed channel where submerged flexible filaments extend longitudinally along both sides of the channel. This configuration forms a horizontal and a lateral edge extending in the streamwise direction. The analysis of both the flow and filament dynamics has revealed several key findings:

1. **Flow characteristics and intermediate behavior**

   The characteristics of the main flow, turbulent structures, and energy balance indicate that the canopy patch scenario behaves as an intermediate case between the limiting scenarios of a fully distributed canopy and an unvegetated open channel. Consequently:

   - In the vegetated region, far from the lateral boundary, the system can be simplified by modeling it as a fully distributed canopy covering the bottom wall. Here, vertical streamwise velocity profiles display two inflection points.
   - In the non-vegetated region, the flow can be modeled as an open channel, with no inflection points in the velocity profile.

2. **Influence of the near-junction region**

   The near-junction region, influenced by both vegetated and non-vegetated areas, exhibits distinct characteristics and must be treated separately. In this region:

- S-shaped velocity profiles persist on the main-channel side, even in the absence of vegetation, with two inflection points.
- These inflection points approach each other and merge as the flow transitions to the open channel condition.

3. **Kelvin-Helmholtz instability**

   The presence of inflection points in both vertical and transverse streamwise velocity profiles suggests susceptibility to Kelvin-Helmholtz instabilities and the formation of coherent structures. These structures, also referred to as secondary circulations, facilitate mass and momentum exchange between the canopy and the outer flow by:

   - Inducing an upflow above the horizontal edge of the canopy.
   - Causing inflow at the lateral edge.

   Thus, high-energy flow enters the vegetated region laterally and exits from the top of the canopy, ensuring mass conservation.

4. **Quadrant analysis and turbulent events**

   Quadrant analysis revealed that:

   - Ejections dominate above the vegetated regions, regardless of the vegetation distribution, and the shape of the joint probability density function (J-PDF) remains consistent;
   - Sweeps dominate at the lateral interface of the canopy.

5. **Coupling between flow and filament dynamics**

   The coupling between the flow and filament dynamics is evident:

   - Filaments bend under the flow's influence and oscillate around their mean deflected position, regardless of vegetation distribution.
   - Filaments near the boundary between vegetated and non-vegetated regions exhibit greater deflection and oscillate over a broader range of frequencies compared to those deeper within the canopy. This behavior confirms the shielding effect of inner filaments, which inhibits larger deflections.
   - In rigid filaments, the structural response dominates, with oscillations occurring at their natural frequency. In more flexible configurations, the structural response diminishes, and filaments oscillate at frequencies characteristic of the larger turbulent structures in the flow.

Those results highlight the challenging nature of these kind of flow. Many more questions may arise, which can pave the way for future research. First of all, in this thesis we considered two filament configurations, but it would be interesting to study different geometries of the canopy patches, to investigate their effect to the different flow properties. Moreover, we highlighted an upflow generated by turbulent structures within the domain, which may play a crucial role in sediment and particle transport. Investigating how scalars are transported by the flow could enhance our understanding of these dynamics and have significant implications in many practical applications.

Appendix A

Second Order Adams-Bashforth Scheme

Considering a generic ODE:

$$y'(t) = f(t, y(t)), \tag{A.1}$$

and integrating it between a generic time interval $[t_{n+1}, t_{n+2}]$, we obtain:

$$y(t_{n+2}) = y(t_{n+1}) + \int_{t_{n+1}}^{t_{n+2}} f(t, y(t))dt. \tag{A.2}$$

However, the integral cannot be computed directly, as it depends from $y(t)$ which is unknown. The second order Adams-Bashforth scheme, to evaluate the integral

$$\int_{t_{n+1}}^{t_{n+2}} f(y, t)dt,$$

adopts a linear polynomial interpolation betweeen t_n and t_{n+1} and the value at t_{n+2} is extrapolated. We consider $\tau \in [t_n, t_{n+1}]$:

$$\begin{aligned} f(y,t) &= \frac{\tau - t_n}{t_{n+1} - t_n} f(y_{n+1}, t_{n+1}) + \frac{t_{n+1} - \tau}{t_{n+1} - t_n} f(y_n, t_n) \\ &= \frac{\tau - t_n}{\Delta t} f(y_{n+1}, t_{n+1}) + \frac{t_{n+1} - \tau}{\Delta t} f(y_n, t_n). \end{aligned}$$

Therefore, the integral:

$$\begin{aligned}
\int_{t_{n+1}}^{t_{n+2}} f(y,t)dt &= \int_{t_{n+1}}^{t_{n+2}} \left[\frac{\tau - t_n}{\Delta t} f(y_{n+1}, t_{n+1}) + \frac{t_{n+1} - \tau}{\Delta t} f(y_n, t_n)\right] d\tau \\
&= \left[\frac{(\tau - t_n)^2}{2 \cdot \Delta t} f(y_{n+1}, t_{n+1}) + \frac{(t_{n+1} - \tau)^2}{(-2) \cdot \Delta t} f(y_n, t_n)\right]_{t_{n+1}}^{t_{n+2}} \\
&= \frac{1}{2} \frac{(t_{n+2} - t_n)^2}{\Delta t} f(y_{n+1} t_{n+1}) - \frac{1}{2} \frac{(t_{n+1} - t_{n+2})^2}{\Delta t} f(y_n, t_n) - \\
&- \frac{1}{2} \frac{(t_{n+1} - t_n)^2}{\Delta t} f(y_{n+1}, t_{n+1}) \\
&= \frac{1}{2} \frac{(2 \cdot \Delta t)^2}{\Delta t} f(y_{n+1}, t_{n+1}) - \frac{1}{2} \frac{(-\Delta t)^2}{\Delta t} f(y_{n+1}, t_{n+1}) - \\
&- \frac{1}{2} \frac{(\Delta t)^2}{\Delta t} f(y_n, t_n) \\
&= \frac{3}{2} f(y_{n+1}, t_{n+1}) \Delta t - \frac{1}{2} f(y_n, t_n) \Delta t,
\end{aligned}$$

which leads to the Adams-Bashforth method (Atkinson et al. 2009):

$$y_{n+2} = y_{n+1} + \Delta t \left(\frac{3}{2} f(y_{n+1}, t_{n+1}) - \frac{1}{2} f(y_n, t_n)\right). \tag{A.3}$$

Bibliography

Abdolahpour, M., M. Ghisalberti, K. McMahon, and P. S. Lavery (2018). «The impact of flexibility on flow, turbulence, and vertical mixing in coastal canopies». en. In: *Limnology and Oceanography* 63.6, pp. 2777–2792. ISSN: 1939-5590 (cit. on pp. 15, 71).

Ackerman, J. D. and A. Okubo (1993). «Reduced Mixing in a Marine Macrophyte Canopy». In: *Functional Ecology* 7.3. Publisher: [British Ecological Society, Wiley], pp. 305–309. ISSN: 0269-8463 (cit. on pp. 11, 26).

Alben, S., M. Shelley, and J. Zhang (Dec. 2002). «Drag reduction through self-similar bending of a flexible body». en. In: *Nature* 420.6915. Publisher: Nature Publishing Group, pp. 479–481. ISSN: 1476-4687 (cit. on pp. 15, 26, 77, 80, 81).

Anjum, N. and N. Tanaka (2020). «Investigating the turbulent flow behaviour through partially distributed discontinuous rigid vegetation in an open channel». en. In: *River Research and Applications* 36.8, pp. 1701–1716. ISSN: 1535-1467 (cit. on p. 9).

Ashie, Y., V. Thanh Ca, and T. Asaeda (May 1999). «Building canopy model for the analysis of urban climate». In: *Journal of Wind Engineering and Industrial Aerodynamics* 81.1, pp. 237–248. ISSN: 0167-6105 (cit. on p. 4).

Atkinson, K. E., W. Han, and D. Stewart (2009). «Multistep methods». en. In: *Numerical Solution of Ordinary Differential Equations*. John Wiley & Sons, Ltd, pp. 95–109. ISBN: 978-1-118-16449-5 (cit. on p. 88).

Banaei, A. A., M. E. Rosti, and L. Brandt (Jan. 2020). «Numerical study of filament suspensions at finite inertia». English. In: *JOURNAL OF FLUID MECHANICS* 882. Num Pages: 27 Place: New York Publisher: Cambridge Univ Press Web of Science ID: WOS:000506238300005, A5. ISSN: 0022-1120, 1469-7645 (cit. on pp. 39, 40).

Belcher, S. E., N. Jerram, and J. C. R. Hunt (July 2003). «Adjustment of a turbulent boundary layer to a canopy of roughness elements». en. In: *Journal of Fluid Mechanics* 488, pp. 369–398. ISSN: 1469-7645, 0022-1120 (cit. on p. 12).

Bennett, S. J., T. Pirim, and B. D. Barkdoll (Apr. 2002). «Using simulated emergent vegetation to alter stream flow direction within a straight experimental channel». In: *Geomorphology* 44.1, pp. 115–126. ISSN: 0169-555X (cit. on pp. 13, 18, 49).

Borg, A., B. Paulsen Husted, and O. Njå (May 2014). «The concept of validation of numerical models for consequence analysis». In: *Reliability Engineering & System Safety*. Special issue of selected articles from ESREL 2012 125, pp. 36–45. ISSN: 0951-8320 (cit. on p. 41).

C3S seasonal lookback: summer 2024 | Copernicus (2024) (cit. on p. 3).

Caroppi, G., K. Västilä, P. Gualtieri, J. Järvelä, M. Giugni, and P. M. Rowiński (2021). «Comparison of Flexible and Rigid Vegetation Induced Shear Layers in Partly Vegetated Channels». en. In: *Water Resources Research* 57.3, e2020WR028243. ISSN: 1944-7973 (cit. on pp. 10, 24, 27, 29).

Coceal, O. and S. E. Belcher (2004). «A canopy model of mean winds through urban areas». en. In: *Quarterly Journal of the Royal Meteorological Society* 130.599, pp. 1349–1372. ISSN: 1477-870X (cit. on p. 4).

Colomer, J. and T. Serra (Jan. 2021). «The World of Edges in Submerged Vegetated Marine Canopies: From Patch to Canopy Scale». en. In: *Water* 13.17. Number: 17 Publisher: Multidisciplinary Digital Publishing Institute, p. 2430. ISSN: 2073-4441 (cit. on pp. 19, 77).

Cui, J. and V. S. Neary (May 2008). «LES study of turbulent flows with submerged vegetation». In: *Journal of Hydraulic Research* 46.3, pp. 307–316. ISSN: 0022-1686 (cit. on pp. 14, 28).

Devi, T. B. and B. Kumar (June 2016a). «Experimentation on submerged flow over flexible vegetation patches with downward seepage». In: *Ecological Engineering* 91, pp. 158–168. ISSN: 0925-8574 (cit. on pp. 10, 22, 27, 80).

— (Sept. 2016b). «Flow characteristics in an alluvial channel covered partially with submerged vegetation». In: *Ecological Engineering* 94, pp. 478–492. ISSN: 0925-8574 (cit. on pp. 10, 19, 24).

Diwan, S. S. (Jan. 2015). «Necessary conditions for spatial inviscid instability». en. In: *Proceedings of the Royal Society A: Mathematical, Physical and Engineering Sciences* 471.2173, p. 20140607. ISSN: 1364-5021, 1471-2946 (cit. on p. 11).

Dolez, P. I. (Jan. 2021). «Energy Harvesting Materials and Structures for Smart Textile Applications: Recent Progress and Path Forward». en. In: *Sensors* 21.18. Number: 18 Publisher: Multidisciplinary Digital Publishing Institute, p. 6297. ISSN: 1424-8220 (cit. on p. 25).

Dorr, F. W. (1970). «The Direct Solution of the Discrete Poisson Equation on a Rectangle». In: *SIAM Review* 12.2, pp. 248–263 (cit. on p. 38).

Dupuis, V., S. Proust, C. Berni, and A. Paquier (Mar. 2017). «Mixing layer development in compound channel flows with submerged and emergent rigid vegetation over the floodplains». en. In: *Experiments in Fluids* 58.4, p. 30. ISSN: 1432-1114 (cit. on p. 16).

European Commission, E. E. A. (Dec. 2008). *Directive - 2008/105 - EN - EUR-Lex*. en. Doc ID: 32008L0105 Doc Sector: 3 Doc Title: Directive 2008/105/EC of the European Parliament and of the Council of 16 December 2008 on environmental quality standards in the field of water policy, amending and subsequently repealing Council Directives 82/176/EEC, 83/513/EEC, 84/156/EEC, 84/491/EEC, 86/280/EEC and amending Directive 2000/60/EC of the European Parliament and of the Council Doc Type: L Usr_lan: en (cit. on p. 3).

— (2021). *COMMUNICATION FROM THE COMMISSION TO THE EUROPEAN PARLIAMENT, THE COUNCIL, THE EUROPEAN ECONOMIC AND SOCIAL COMMITTEE AND THE COMMITTEE OF THE REGIONS Pathway to a Healthy Planet for All EU Action Plan: 'Towards Zero Pollution for Air, Water and Soil'*. en (cit. on p. 3).

— (Oct. 2024). *Europe's state of water 2024: the need for improved water resilience.* en (cit. on pp. 2, 3).

Fang, Z., C. Gong, A. Revell, and J. O'Connor (Feb. 2022). «Fluid–structure interaction of a vegetation canopy in the mixing layer». In: *Journal of Fluids and Structures* 109, p. 103467. ISSN: 0889-9746 (cit. on pp. 15, 26).

Finnigan, J. (Jan. 2000). «Turbulence in Plant Canopies». en. In: *Annual Review of Fluid Mechanics* 32.Volume 32, 2000. Publisher: Annual Reviews, pp. 519–571. ISSN: 0066-4189, 1545-4479 (cit. on p. 11).

Foggi Rota, G., M. Koseki, R. Agrawal, S. Olivieri, and M. Rosti (Jan. 2024). «Forced and natural dynamics of a clamped flexible fiber in wall turbulence». In: *Physical Review Fluids* 9, p. L012601 (cit. on pp. iii, 27, 33, 75, 80, 82).

Folkard, A. M. (June 2011). «Flow regimes in gaps within stands of flexible vegetation: laboratory flume simulations». en. In: *Environmental Fluid Mechanics* 11.3, pp. 289–306. ISSN: 1573-1510 (cit. on p. 9).

Fujin Code (Mar. 2020) (cit. on pp. 35, 41, 43).

Ghiasi, Z., D. Li, J. Komperda, and F. Mashayek (Nov. 2018). «Near-wall resolution requirement for direct numerical simulation of turbulent flow using multidomain Chebyshev grid». In: *International Journal of Heat and Mass Transfer* 126, pp. 746–760. ISSN: 0017-9310 (cit. on p. 35).

Ghisalberti, M. and H. M. Nepf (2004). «The limited growth of vegetated shear layers». en. In: *Water Resources Research* 40.7. ISSN: 1944-7973 (cit. on p. 13).

Ghisalberti, M. and H. Nepf (June 2006). «The Structure of the Shear Layer in Flows over Rigid and Flexible Canopies». en. In: *Environmental Fluid Mechanics* 6.3, pp. 277–301. ISSN: 1567-7419, 1573-1510 (cit. on p. 11).

Ghisalberti, M. and H. M. Nepf (2002). «Mixing layers and coherent structures in vegetated aquatic flows». en. In: *Journal of Geophysical Research: Oceans* 107.C2, pp. 3–1–3–11. ISSN: 2156-2202 (cit. on pp. 11, 13, 26).

Gillerot, L., D. Landuyt, P. De Frenne, B. Muys, and K. Verheyen (Feb. 2024). «Urban tree canopies drive human heat stress mitigation». In: *Urban Forestry & Urban Greening* 92, p. 128192. ISSN: 1618-8667 (cit. on p. 4).

Gurnell, A. (2014). «Plants as river system engineers». en. In: *Earth Surface Processes and Landforms* 39.1, pp. 4–25. ISSN: 1096-9837 (cit. on p. 3).

Hasegawa, Y., M. Quadrio, and B. Frohnapfel (July 2014). «Numerical simulation of turbulent duct flows with constant power input». en. In: *Journal of Fluid Mechanics* 750, pp. 191–209. ISSN: 0022-1120, 1469-7645 (cit. on pp. 34, 44).

Huai, W.-x., S. Li, G. G. Katul, M.-y. Liu, and Z.-h. Yang (June 2021). «Flow dynamics and sediment transport in vegetated rivers: A review». en. In: *Journal of Hydrodynamics* 33.3, pp. 400–420. ISSN: 1878-0342 (cit. on pp. 19, 77).

Huai, W.-X., J. Zhang, W.-J. Wang, and G. G. Katul (June 2019). «Turbulence structure in open channel flow with partially covered artificial emergent vegetation». In: *Journal of Hydrology* 573, pp. 180–193. ISSN: 0022-1694 (cit. on pp. 9, 16–18).

Huang, W. X., S. J. Shin, and H. J. Sung (2007). «Simulation of flexible filaments in a uniform flow by the immersed boundary method». en. In: *Journal of Computational Physics* 226.2, pp. 2206–2228. ISSN: 0021-9991 (cit. on pp. 40–43).

Ikeda, S. and M. Kanazawa (Nov. 1996). «Three-Dimensional Organized Vortices above Flexible Water Plants». EN. In: *Journal of Hydraulic Engineering* 122.11. Publisher: American Society of Civil Engineers, pp. 634–640. ISSN: 0733-9429 (cit. on p. 11).

Kim, J. and P. Moin (1985). «Application of a fractional-step method to incompressible Navier-Stokes equations». In: *Journal of Computational Physics* 59.2. Publisher: Elsevier, pp. 308–323 (cit. on p. 35).

Langre, E. de (Jan. 2008). «Effects of Wind on Plants». In: *Annual Review of Fluid Mechanics* 40, pp. 141–168. ISSN: 0066-4189 (cit. on pp. 26, 29).

Leclercq, T. and E. de Langre (Jan. 2016). «Drag reduction by elastic reconfiguration of non-uniform beams in non-uniform flows». In: *Journal of Fluids and Structures* 60, pp. 114–129. ISSN: 0889-9746 (cit. on p. 26).

Li, D., W. Huai, Y. Guo, and M. Liu (May 2022). «Flow characteristics in partially vegetated channel with homogeneous and heterogeneous layouts». en. In: *Environmental Science and Pollution Research* 29.25, pp. 38186–38197. ISSN: 0944-1344, 1614-7499 (cit. on pp. 10, 22).

Li, F., Y. Shan, M. Li, Y. Guo, and C. Liu (2024). «Insights for River Restoration: The Impacts of Vegetation Canopy Length and Canopy Discontinuity on Riverbed Evolution». en. In: *Water Resources Research* 60.7, e2023WR036473. ISSN: 1944-7973 (cit. on p. 12).

Li, J., N. Claude, P. Tassi, F. Cordier, A. Vargas-Luna, A. Crosato, and S. Rodrigues (2022). «Effects of Vegetation Patch Patterns on Channel Morphology: A Numerical Study». en. In: *Journal of Geophysical Research: Earth Surface* 127.5, e2021JF006529. ISSN: 2169-9011 (cit. on p. 9).

Liu, C., Z. Hu, J. Lei, and H. Nepf (Feb. 2018). «Vortex Structure and Sediment Deposition in the Wake behind a Finite Patch of Model Submerged Vegetation». EN. In: *Journal of Hydraulic Engineering* 144.2. Publisher: American Society of Civil Engineers, p. 04017065. ISSN: 1943-7900 (cit. on pp. 3, 9, 27).

Liu, C., Y.-s. Gao, X.-r. Dong, Y.-q. Wang, J.-m. Liu, Y.-n. Zhang, X.-s. Cai, and N. Gui (Apr. 2019). «Third generation of vortex identification methods: Omega and Liutex/Rortex based systems». en. In: *Journal of Hydrodynamics* 31.2, pp. 205–223. ISSN: 1878-0342 (cit. on p. 15).

Liu, M., S. Yuan, H. Tang, W. Huai, and J. Yan (Nov. 2024). «Investigation of turbulence and interfacial exchange features of the gap area within the fully developed Shallow-Submerged canopy flow». In: *Journal of Hydrology* 643, p. 131938. ISSN: 0022-1694 (cit. on p. 13).

McLaren, P., S. H. Hill, and D. Bowles (Dec. 2007). «Deriving transport pathways in a sediment trend analysis (STA)». In: *Sedimentary Geology*. From Particle Size to Sediment Dynamics 202.3, pp. 489–498. ISSN: 0037-0738 (cit. on p. 3).

Monti, A., M. Omidyeganeh, and A. Pinelli (June 2019). «Large-eddy simulation of an open-channel flow bounded by a semi-dense rigid filamentous canopy: Scaling and flow structure». In: *Physics of Fluids* 31.6, p. 065108. ISSN: 1070-6631 (cit. on p. 11).

Monti, A., S. Olivieri, and M. E. Rosti (Mar. 2023). «Collective dynamics of dense hairy surfaces in turbulent flow». en. In: *Scientific Reports* 13.1. Publisher: Nature Publishing Group, p. 5184. ISSN: 2045-2322 (cit. on pp. 27, 41).

Nakagawa, H. and I. Nezu (Apr. 1977). «Prediction of the contributions to the Reynolds stress from bursting events in open-channel flows». en. In: *Journal of Fluid Mechanics* 80.1, pp. 99–128. ISSN: 1469-7645, 0022-1120 (cit. on p. 14).

Naot, D., I. Nezu, and H. Nakagawa (Nov. 1996). «Hydrodynamic Behavior of Partly Vegetated Open Channels». EN. In: *Journal of Hydraulic Engineering* 122.11. Publisher: American Society of Civil Engineers, pp. 625–633. ISSN: 0733-9429 (cit. on p. 21).

Nepf, H., M. Ghisalberti, B. White, and E. Murphy (2007). «Retention time and dispersion associated with submerged aquatic canopies». en. In: *Water Resources Research* 43.4. ISSN: 1944-7973 (cit. on p. 13).

Nepf, H. M. (June 2012). «Hydrodynamics of vegetated channels». In: *Journal of Hydraulic Research* 50.3, pp. 262–279. ISSN: 0022-1686 (cit. on pp. 11, 25, 26).

Nezu, I. and K. Onitsuka (Dec. 2001). «Turbulent structures in partly vegetated open-channel flows with LDA and PI V measurements». In: *Journal of Hydraulic Research* 39.6, pp. 629–642. ISSN: 0022-1686 (cit. on pp. 18, 20, 78).

Nezu, I. and M. Sanjou (Oct. 2008). «Turburence structure and coherent motion in vegetated canopy open-channel flows». English. In: *JOURNAL OF HYDRO-ENVIRONMENT RESEARCH* 2.2. Num Pages: 29 Place: Amsterdam Publisher: Elsevier Web of Science ID: WOS:000207652500002, pp. 62–90. ISSN: 1570-6443, 1876-4444 (cit. on pp. 12–15, 80).

Okamoto, T.-A. and I. Nezu (Nov. 2009). «Turbulence structure and “Monami” phenomena in flexible vegetated open-channel flows». In: *Journal of Hydraulic Research* 47.6, pp. 798–810. ISSN: 0022-1686 (cit. on p. 13).

Pang, C.-c., D. Wu, X.-j. Lai, S.-q. Wu, and F.-f. Wang (Aug. 2014). «Turbulence structure and flow field of shallow water with a submerged *eel grass* patch». In: *Ecological Engineering* 69, pp. 201–205. ISSN: 0925-8574 (cit. on pp. 10, 23, 27, 29, 78).

Pope, S. B. (Aug. 2000). *Turbulent Flows*. en. ISBN: 9780511840531 Publisher: Cambridge University Press (cit. on pp. 28, 44, 67).

Py, C., E. de Langre, B. Moulia, and P. Hémon (June 2005). «Measurement of wind-induced motion of crop canopies from digital video images». In: *Agricultural and Forest Meteorology* 130.3, pp. 223–236. ISSN: 0168-1923 (cit. on p. 27).

Py, C., E. D. Langre, and B. Moulia (Dec. 2006). «A frequency lock-in mechanism in the interaction between wind and crop canopies». en. In: *Journal of Fluid Mechanics* 568, pp. 425–449. ISSN: 1469-7645, 0022-1120 (cit. on pp. 25, 27, 39, 82).

Rahimi, H., C. M. S. Fael, C. S. B. Taborda, S. Yuan, X. Tang, P. K. Singh, E. Fardoost, and C. A. V. Santos (Jan. 2023). «Numerical Modelling of Turbulence Kinetic Energy in Open Channel Flows with Mixed-Layer Vegetation». en. In: *Water* 15.14. Number: 14 Publisher: Multidisciplinary Digital Publishing Institute, p. 2544. ISSN: 2073-4441 (cit. on p. 28).

Raupach, M. R. (July 1981). «Conditional statistics of Reynolds stress in rough-wall and smooth-wall turbulent boundary layers». en. In: *Journal of Fluid Mechanics* 108, pp. 363–382. ISSN: 1469-7645, 0022-1120 (cit. on p. 64).

Raupach, M. R., J. J. Finnigan, and Y. Brunei (Mar. 1996). «Coherent eddies and turbulence in vegetation canopies: The mixing-layer analogy». en. In: *Boundary-Layer Meteorology* 78.3, pp. 351–382. ISSN: 1573-1472 (cit. on p. 11).

Rayleigh, L. (Nov. 1879). «On the Stability, or Instability, of certain Fluid Motions». In: *Proceedings of the London Mathematical Society* s1-11.1, pp. 57–72. ISSN: 0024-6115 (cit. on pp. 11, 16).

Rominger, J. T. and H. M. Nepf (Aug. 2011). «Flow adjustment and interior flow associated with a rectangular porous obstruction». en. In: *Journal of Fluid Mechanics* 680, pp. 636–659. ISSN: 1469-7645, 0022-1120 (cit. on pp. 15–17, 20).

Rota, G. F., A. Monti, S. Olivieri, and M. E. Rosti (June 2024). «Dynamics and fluid–structure interaction in turbulent flows within and above flexible canopies». en. In: *Journal of Fluid Mechanics* 989, A11. ISSN: 0022-1120, 1469-7645 (cit. on pp. 6, 11, 27, 32, 39, 41, 52, 61, 62, 64, 65, 75, 77, 78, 82).

Shen, S. and M. Y. Leclerc (Nov. 1997). «Modelling the turbulence structure in the canopy layer». In: *Agricultural and Forest Meteorology.* Physical and Biophysical Processes in the Vegetation Environment 87.1, pp. 3–25. ISSN: 0168-1923 (cit. on p. 61).

Shimizu, Y., T. Tsujimoto, H. Nakagawa, and T. Kitamura (Nov. 1991). «EXPERIMENTAL STUDY ON FLOW OVER RIGID VEGETATION SIMULATED BY CYLINDERS WITH EQUI-SPACING». en. In: *Doboku Gakkai Ronbunshu* 1991.438, pp. 31–40. ISSN: 0289-7806, 1882-7187 (cit. on p. 41).

Sinoquet, H., X. Le Roux, B. Adam, T. Ameglio, and F. A. Daudet (Apr. 2001). «RATP: a model for simulating the spatial distribution of radiation absorption, transpiration and photosynthesis within canopies: application to an isolated tree crown». English. In: *PLANT CELL AND ENVIRONMENT* 24.4. Num Pages: 12 Place: Oxford Publisher: Blackwell Science Ltd Web of Science ID: WOS:000167999300002, pp. 395–406. ISSN: 0140-7791 (cit. on p. 25).

Tinoco, R. O., J. E. San Juan, and J. C. Mullarney (2020). «Simplification bias: lessons from laboratory and field experiments on flow through aquatic vegetation». en. In: *Earth Surface Processes and Landforms* 45.1, pp. 121–143. ISSN: 1096-9837 (cit. on p. 10).

Tschisgale, S., B. Löhrer, R. Meller, and J. Fröhlich (June 2021). «Large eddy simulation of the fluid–structure interaction in an abstracted aquatic canopy consisting of flexible blades». en. In: *Journal of Fluid Mechanics* 916, A43. ISSN: 0022-1120, 1469-7645 (cit. on pp. 26, 27, 76).

Unigarro Villota, S., M. Ghisalberti, J. Philip, and P. Branson (2023). «Characterizing the Three-Dimensional Flow in Partially Vegetated Channels». en. In: *Water Resources Research* 59.1, e2022WR032570. ISSN: 1944-7973 (cit. on pp. 9, 10, 19, 22, 28, 50, 78).

Urban heat islands and heat mortality (2024). en (cit. on p. 3).

Vogel, S. (1994). *Life in Moving Fluids: The Physical Biology of Flow - Revised and Expanded Second Edition.* NED - New edition. Princeton University Press. ISBN: 978-0-691-03485-0 (cit. on pp. 26, 81).

Wallace, J. M. (Jan. 2016). «Quadrant Analysis in Turbulence Research: History and Evolution». en. In: *Annual Review of Fluid Mechanics* 48.Volume 48, 2016. Publisher: Annual Reviews, pp. 131–158. ISSN: 0066-4189, 1545-4479 (cit. on p. 64).

Wendt, J. F., ed. (2009). *Computational Fluid Dynamics.* en. Berlin, Heidelberg: Springer. ISBN: 978-3-540-85055-7 978-3-540-85056-4 (cit. on p. 35).

White, B. L. and H. M. Nepf (Dec. 2007). «Shear instability and coherent structures in shallow flow adjacent to a porous layer». en. In: *Journal of Fluid Mechanics* 593, pp. 1–32. ISSN: 1469-7645, 0022-1120 (cit. on pp. 16, 18).

— (2008). «A vortex-based model of velocity and shear stress in a partially vegetated shallow channel». en. In: *Water Resources Research* 44.1. ISSN: 1944-7973 (cit. on pp. 13, 16–18, 79).

Wu, W., F. D. Shields Jr., S. J. Bennett, and S. S. Y. Wang (2005). «A depth-averaged two-dimensional model for flow, sediment transport, and bed topography in curved channels with riparian vegetation». en. In: *Water Resources Research* 41.3. ISSN: 1944-7973 (cit. on p. 3).

Yan, X.-F., H.-F. Duan, W.-H. Wai, C. Li, and X.-K. Wang (Mar. 2022). «Spatial Flow Pattern, Multi-Dimensional Vortices, and Junction Momentum Exchange in a Partially Covered Submerged Canopy Flume». In: *Water Resources Research* 58 (cit. on pp. 10, 19–21, 27, 28).

Yan, X.-F., H.-F. Duan, Y.-H. Zhang, and X.-K. Wang (July 2023). «Momentum fluxes across multiple mixing interfaces subject to partially-distributed submerged canopy flows». In: *Journal of Hydrology* 622, p. 129742. ISSN: 0022-1694 (cit. on pp. 10, 22, 28).

Yan, X.-F., Y.-Y. Jia, Y. Zhang, L.-B. Fang, H.-F. Duan, and X.-K. Wang (2023). «Hydrodynamic adjustment subject to a submerged canopy partially obstructing a flume: Implications for junction flow behaviour». en. In: *Ecohydrology* 16.2, e2467. ISSN: 1936-0592 (cit. on pp. 10, 13, 16, 19–21, 28).

Yan, X.-F., W.-H. O. Wai, and C.-W. Li (Aug. 2016). «Characteristics of flow structure of free-surface flow in a partly obstructed open channel with vegetation patch». en. In: *Environmental Fluid Mechanics* 16.4, pp. 807–832. ISSN: 1573-1510 (cit. on pp. 10, 21).

Yu, Z. (2005). «A DLM/FD method for fluid/flexible-body interactions». en. In: *Journal of Computational Physics* 207.1, pp. 1–27. ISSN: 0021-9991 (cit. on pp. 39, 40).

Zeng, C. and C.-W. Li (Feb. 2014). «Measurements and modeling of open-channel flows with finite semi-rigid vegetation patches». en. In: *Environmental Fluid Mechanics* 14.1, pp. 113–134. ISSN: 1573-1510 (cit. on pp. 12, 23, 27).

Zhang, J., J. Lei, W. Huai, and H. Nepf (2020). «Turbulence and Particle Deposition Under Steady Flow Along a Submerged Seagrass Meadow». en. In: *Journal of Geophysical Research: Oceans* 125.5, e2019JC015985. ISSN: 2169-9291 (cit. on pp. 10, 22).